AN ABSTRACT OF THE DISSERTATION OF

Mark L. Porter for the degree of Doctor of Philosophy in Water Resources Engineering presented on June 13, 2008.

Title: Investigating Capillary Pressure and Interfacial Area for Multiphase Flow in Porous Media using Pore-scale Imaging and Lattice-Boltzmann Modeling

Abstract approved: _____

Dorthe Wildenschild

Recent advances in imaging technology and numerical modeling have greatly enhanced pore-scale investigations of multiphase flow and transport in porous media. It is now feasible to obtain high resolution 3-dimensional pore-scale data, and numerical methods such as the lattice-Boltzmann (LB) technique have been developed specifically for simulating such phenomena. Traditional macro-scale multiphase flow models rely heavily on empirical relationships. For example, the interaction between fluids at their interfaces is accounted for indirectly through the empirical relative permeability relationship. Nevertheless, it has recently been hypothesized that the single most important variable missing from current macro-scale models is the measure of interfacial dynamics between fluids within the pores. Furthermore, the empirical capillary pressure-saturation relationship used in macro-scale multiphase flow simulators has been shown to be a function of interfacial area per volume. This study focuses on (1) the measurement and modeling of the capillary pressure-saturation relationship; and (2) the characterization of the fluid-fluid interfacial area per volume as a function of saturation. The study synthesizes experimental results derived from pore-scale computerized micro-tomographic (CMT) images with LB simulations. An image analysis algorithm for quantifying fluid-fluid interfacial area per volume from experimental CMT and simulation images was developed and verified. The experimental results were shown to be in good agreement with values reported in the literature. Furthermore, the capillary pressure-saturation curves were used to validate a recently proposed macro-scale interfacial area model. New LB simulations of drainage and imbibition for an air-water system were developed, in which the full geometry from the experimental system was used to define the lattice. This allowed for the direct comparison of experimental and simulated phase distributions within the pores. LB simulations showed excellent agreement with experimental results, considering no optimization or calibration to the data was required. Collectively, results show that there is a complex functional relationship between capillary pressure, saturation and interfacial area that provides insights into multiphase flow and transport processes that can not be obtained from the capillary pressure-saturation relationship alone.

Investigating Capillary Pressure and Interfacial Area for Multiphase Flow in Porous Media using Pore-scale Imaging and Lattice-Boltzmann Modeling

by

Mark L. Porter

A DISSERTATION

submitted to

Oregon State University

in partial fulfillment of
the requirements for the
degree of

Doctor of Philosophy

Presented June 13, 2008
Commencement June 2009

Doctor of Philosophy thesis of Mark L. Porter presented on June 13, 2008.

APPROVED:

Major Professor, representing Water Resources Engineering

Director of the of Water Resources Graduate Program

Dean of the Graduate School

I understand that my thesis will become part of the permanent collection of Oregon State University libraries. My signature below authorizes release of my thesis to any reader upon request.

Mark L. Porter, Author

ACKNOWLEDGEMENTS

First and foremost, I would like to extend many thanks to my advisors Dorthe Wildenschild and Marcel Schaap for their support, patience, and encouragement throughout my graduate studies at OSU. Their technical and editorial advice was essential to the completion of this dissertation. I would like to thank Kendra Brown for her assistance in the laboratory. My parents, Linda and Daryl Porter, deserve special thanks and love for their unconditional support and encouragement in my decisions to pursue my ever changing interests throughout my life. Finally, I would like to extend my deepest gratitude and love to Nalisha Johnson for her daily support and encouragement these past few years.

CONTRIBUTION OF AUTHORS

Portions of the research presented in this dissertation would not have been completed without wonderful collaborations with scientists outside of Oregon State University. Marcel Schaap, from the University of Arizona, is responsible for the parallel lattice-Boltzmann code used to perform the simulations. Marcel developed and conducted the simulations using pressure boundary conditions discussed in Chapter 5. Furthermore, Marcel provided code for, and guidance in the analysis of, the 2-point correlation functions. Gavin Grant, Geosyntec Consultants, and Jason Gerhard, University of Western Ontario, provided the explicit IFA modeling results presented in Chapter 4

TABLE OF CONTENTS

Page

Page

LIST OF FIGURES

Figure Page

Figure Page

Figure Page

Figure Page

LIST OF TABLES

Table Page

Investigating Capillary Pressure and Interfacial Area for Multiphase Flow in Porous Media using Pore-scale Imaging and Lattice-Boltzmann Modeling

Chapter 1. Introduction

1.1 Multiphase Flow in Porous Media

Multiphase flow in porous media (hereafter, multiphase flow) differs from single phase flow in that there are at least two immiscible (non-mixing) fluids occupying the pore space. Some examples in which multiphase flow is of concern include: the remediation of contaminants, such as nonaqueous phase liquids (NAPLs), in the vadose zone and underlying aquifers; the infiltration and redistribution of water in the vadose zone where air and water occupy the pore space, sequestration of CO_2; and enhanced petroleum production from underground reservoirs.

In the United States, groundwater contamination became a major environmental issue in the late seventies. Many of the contaminated subsurface sites in the United States have been attributed to human activities such as waste-disposal practices, runoff from agricultural and urban watersheds, accidental spills, and leaking underground storage tanks [Charbeneau, 2000]. Contaminates associated with accidental spills and leaking underground storage tanks were often released as NAPLs. When introduced into the subsurface, NAPLs form a separate, mobile phase whose migration is controlled by gravitational, buoyant, viscous, and capillary forces [Bedient et al., 1997]. NAPLs are most commonly classified by their specific gravities; light nonaqueous phase liquids (LNAPLs) have a specific gravity less than water and dense nonaqueous phase liquids (DNAPLs) have a specific gravity greater than water. This simple classification system provides useful insights into the general migration patterns of NAPLs: LNAPLs tend to migrate to the water table where they form pools at the capillary fringe, whereas DNAPLs tend to travel deep into the saturated zone. LNAPLs found in the subsurface are typically associated with the production and distribution of petroleum products and the most common chemicals include benzene, toluene, ethyl benzene, and xylene (BTEX), naphthalene, octane and decane. DNAPLs found in the subsurface are typically associated with industrial activities such as degreasing, metal stripping, chemical manufacturing, pesticide production and creosote operations [Bedient et al., 1997]. Some common chemicals associated with DNAPLs include chlorinated aliphatic hydrocarbons (CAHs), the most prevalent being tetrachloroethylene (PCE), trichloroethylene (TCE), and trichloroethane (TCA), polyaromatic hydrocarbons (PAHs) and pentachlorobiphenyls (PCBs). Once the source of the NAPL is cut off or depleted,

continuous NAPL phase may form numerous disconnected blobs in the pores. These blobs are held in the pore space by capillary forces and act as a continual source of contamination for the passing groundwater.

The movement of water in the vadose zone is inherently a multiphase system since air and water occupy the pore space. The vadose zone generally consists of the region between the ground surface and the water table, thus the study of how water moves in this region is critical for understanding (1) the interaction between surface and groundwater, (2) the water balance for groundwater and (3) transport of contaminants from the surface to the groundwater. Additionally, soil moisture content is a controlling factor for many vadose zone processes, including infiltration, surface runoff, deep drainage, redistribution, root uptake, solute transport and groundwater recharge. The vast majority of plants depend on the water stored in the vadose zone and almost all of the available groundwater is generated by percolation through the vadose zone [Selker et al., 1999]. Furthermore, plants and crops are typically larger players in the hydrologic cycle than rivers [Smith et al., 2002]. Thus, the importance of the vadose zone should not be underestimated.

Multiphase flow processes of engineering and scientific concern are often studied on several different scales (e.g., molecular, pore- (or micro-), macro- (or Darcy), etc.) each of which is intricately related to the other scales. The two scales of interest in this research are the pore-scale and the macro-scale. Figure 1.1 illustrates a conceptual model of the relationship between the pore-scale and macro-scale, and defines some variables of interest at the pore-scale. The macro-scale differs from the pore-scale in that the property of interest is defined over a representative elementary volume (REV), which is defined as a volume that is much smaller than the entire flow domain, but is large enough to permit a meaningful statistical average (i.e., no large fluctuations in the average value) [Bear, 1988]. For example, porosity is defined as the ratio of the void space to total volume, and the REV condition is satisfied when the addition or subtraction of a few pores does not cause large differences in that ratio. If the size of the total volume under consideration is successively decreased, at some point the volume will be small enough to fit entirely into the pore space or solid phase, thus at the pore-scale the concept of porosity loses its meaning. At the pore-scale a porous medium is composed of a solid phase and a connected pore space (or void space) in which the fluids may flow and interact [Gray et al., 2002]. Each phase is separated by a thin transition layer, the interface, that can be quantified by interfacial area. The phases are bounded by the interfaces, each of which is a moving boundary. Thus, at the pore-scale the volume is occupied by evolving geometries of various phases and interfaces (Figure 1.1) [Gray et al., 2002].

Mathematical equations that describe processes, such as fluid flow and solute transport, within a porous medium differ between the macro-scale and the pore-scale. Robust models for macro-scale flow and transport are typically derived from pore-scale models, via an averaging

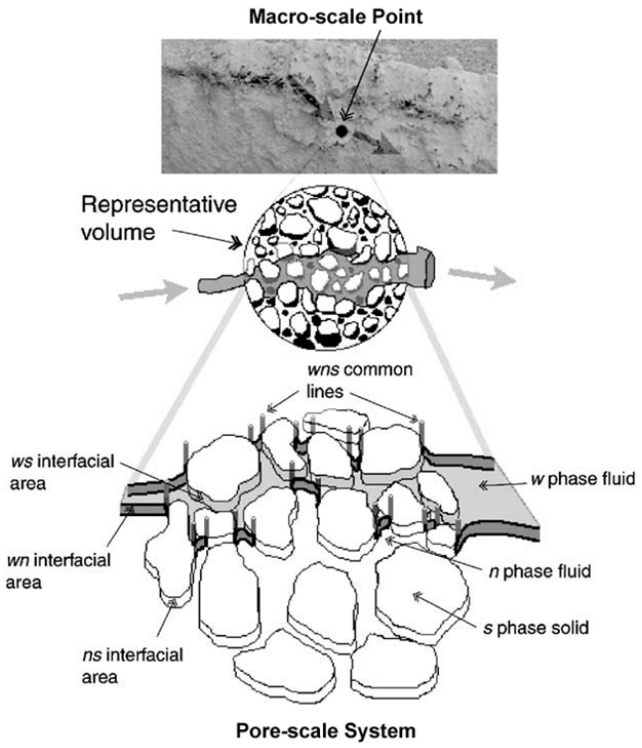

Figure 1.1: Illustration of the relationship between the macro-scale and the pore-scale. At the pore-scale individual components are defined, whereas at the macro-scale the components only occupy a fraction of the volume and the system is described by average values defined over a REV. Adapted from Gray et al. [2002].

scheme, which accounts for the physics encountered at the pore-scale. However, traditional macro-scale multiphase flow models rely heavily on extensions of Darcy's Law and empirical relationships that do not fully capture all of the important physical phenomena [Muccino et al., 1998]. As a result, the governing flow equations are obtained by enhancing a simple coefficient with complex functional dependencies rather than by constructing a general set of conservation equations that account for the physics of the problem at hand [Muccino et al., 1998]. For example, the common approach used to model two-phase flow for a NAPL-water system in subsurface environments is to use Darcy's law for each phase and account for the interaction of the fluids by (1) introducing relative permeability and (2) assuming the pressure gradients between the two phases are related by capillary pressure [Dullien, 1992]. This results in the empirical capillary pressure - saturation - permeability ($P_c - S - k_r$) relationship, of which

various forms exist. Only recently have macro-scale multiphase flow models based on pore-scale considerations been presented in the literature [Hassanizadeh and Gray, 1990; Gray, 1999; Gray et al., 2002; Muraleetharan and Wei, 1999; Wei and Muraleetharan, 2002; Murdoch and Hassanizadeh, 2002]

Advances in pore-scale experimental and numerical methods have helped identify weaknesses and inconsistencies with traditional macro-scale multiphase flow models and guided the development of improved theoretical models [Miller et al., 1998]. One such pore-scale experimental technique is high resolution imaging, which allows for direct observation of the pore space geometry and fluid configurations within the pores. Computerized microtomography (CMT) coupled with synchrotron X-ray sources has become an effective method for imaging multiphase flow experiments at resolutions ranging from 5-20 μm [e.g., Coles et al., 1998; Wildenschild et al., 2002, 2005; Culligan et al., 2004, 2006; Brusseau et al., 2007; Schnaar and Brusseau, 2006; Prodonavić et al., 2007].

Conventional methods for simulating pore-scale multiphase flow include numerical integration of the Navier-Stokes equations [Williams, 1969; Quartapelle, 1993] and molecular (i.e., particle tracking) dynamics simulations [Ma et al., 1992]. However, these models are extremely computationally intensive, and implementation difficulties arise when applied to random geometries [Swift et al., 1995]. Other methods, such as pore network, smooth particle hydrodynamics (SPH), and lattice-Boltzmann (LB), have proven successful for multiphase flow in complex pore geometries. Pore network models typically require the least computational resources, however, they use a statistical representation of the pore space and require simplifying assumptions about the interface geometry. SPH is a meshfree particle method making it attractive for simulating moving interfaces, however, SPH is computational intensive and implementation of prescribed boundary conditions is difficult [Tartakovsky et al., 2007]. The LB method is appealing in this research since the geometry of the pores obtained from CMT images may be used to define the lattice, which allows for detailed comparisons of phase distributions between experiments and simulations. Additionally, parallel implementation of the LB model is relatively straightforward, which is essential since the LB method is computationally intensive.

1.2 Research Objectives

The goal of this research is to develop a better understanding of multiphase flow at the macro-scale by synthesizing pore-scale multiphase experimental results, derived from high resolution 3D CMT image data, with multiphase LB simulations. The overall focus is on the role of capillary pressure and interfacial area per volume in multiphase flow with an emphasis on the dependence of capillary pressure on saturation and interfacial area.

The specific objectives for this research are listed below.

1. Develop and validate an image analysis technique that may be used to estimate properties such as phase distributions (i.e., porosity and saturation) and interfacial area from CMT image data.

2. Collect 3D CMT image data for NAPL-water-glass bead drainage and imbibition experiments.

3. Investigate the relationship between capillary pressure, saturation and interfacial area per volume by comparing experimental results with empirical relationships reported in the literature.

4. Conduct new LB drainage and imbibition simulations of air-water experiments and compare results directly to the experimental system with an emphasis on the relationship between capillary pressure, saturation and interfacial area.

1.3 Organization

Chapter 2 provides a review of the literature and theoretical background relevant to this research. Chapter 2 is divided into five sections, the first of which provides a discussion of the fundamental principles of multiphase flow. The second section in Chapter 2 describes a classical approach for modeling multiphase flow at the macro-scale, including a discussion of the dependence of these models on empirical relationships. An alternative approach for modeling multiphase flow at the macro-scale is discussed in the third section. The fourth section focuses on experimental methods for obtaining empirical relationships for the capillary pressure-saturation-interfacial area relationship. The final section of chapter 2 provides a discussion of pore-scale modeling, with an emphasis on LB modeling including a discussion of the LB model used in this research. Chapter 3, 4 and 5 specifically address the objectives listed in Section 1.2 and each chapter corresponds to manuscripts that will be submitted for publication. Chapter 3 describes and validates, by comparisons with other methods reported in the literature, the image analysis techniques used to obtain estimates of porosity, saturation and interfacial area from CMT image data. Chapter 4 presents capillary pressure, saturation and interfacial area estimates obtained from NAPL-water drainage and imbibition experiments, and investigates the relationship between these variables by means of comparison with interfacial area estimates predicted by a theoretical model based on the empirical capillary pressure - saturation relationship. New LB simulations of air-water drainage and imbibition experiments are presented in Chapter 5, with an emphasis on the comparison of phase distributions within the pores, capillary pressure - saturation curves and interfacial area - saturation curves between the two systems. The summary and conclusions from this research are presented in Chapter 6.

Chapter 2. Multiphase Flow and Transport

This chapter provides a summary of the scientific literature relevant to the physical processes that govern the flow of immiscible fluids in porous media. This review is intended to provide an overview of the fundamental concepts from which the theory of multiphase flow was constructed, as well as provide an overview of some of the current theories, experimental techniques, and numerical methods that are shaping the field. This survey is not meant to be exhaustive, and in fact, only provides a detailed review of topics relevant to this research.

2.1 Basics of Multiphase Flow

The flow of two or more immiscible (non-mixing) fluids is characterized by the existence of a fluid-fluid interface separating the fluids, and nonzero interfacial tension [Bear, 1988]. At the pore-scale, the porous medium consists of the solid phase and the pore space, in which the fluids reside and interact. At the macro-scale, saturation quantifies the existence of multiple fluids within the pore space. Saturation is defined as the fraction of the pore space occupied by any given fluid. Thus, a saturation value exists for each fluid in the system and the sum of all saturation values is equal to one.

Multiphase flow can be divided into two categories, namely steady state and unsteady state. Steady state flow refers to situations in which all macroscopic properties of the system are constant in time at all points in the system, thus no displacement of one fluid by another is occurring in the system [Dullien, 1992]. Unsteady state flow refers to the situation in which macroscopic properties change with time, thus if there is a change in saturation over time the flow phenomenon is considered unsteady [Dullien, 1992]. Therefore, drainage and imbibition, defined below, are unsteady flow events since the saturation changes as one fluid displaces another fluid.

2.1.1 Wettability

Capillary forces arise in multiphase porous systems due to interfaces that exist between the immiscible fluids and the fluids and the solid phase. The work required to maintain the separation between the fluids and solids is known as the interfacial tension, σ, and has units of force per length. If two immiscible fluids are placed in contact with a flat solid surface, one of the fluids will often form a drop as depicted in Figure 2.1. The contact angle, θ denotes the angle

between the fluid-fluid interface and the solid. At equilibrium, the magnitude of the contact angle is defined by the Young-Laplace equation:

$$\cos\theta = \frac{\sigma_{ns} - \sigma_{ws}}{\sigma_{nw}} \tag{2.1}$$

where σ_{ns} is the interfacial tension between the phases denoted by the subscripts. The contact angle can range from $0° < \theta < 180°$ and the magnitude of θ determines the wettability of the fluid. If $\theta < 90°$, the fluid through which the contact angle was measured is considered the wetting fluid (or phase), whereas if $\theta > 90°$, the fluid through which the contact angle is measured is considered the nonwetting fluid (or phase). Thus, a porous system with two immiscible fluids is generally composed of a solid, wetting and nonwetting phase. If $\theta = 90°$, then both fluids equally wet the solid, and if $\theta = 0°$, then one fluid perfectly wets the solid.

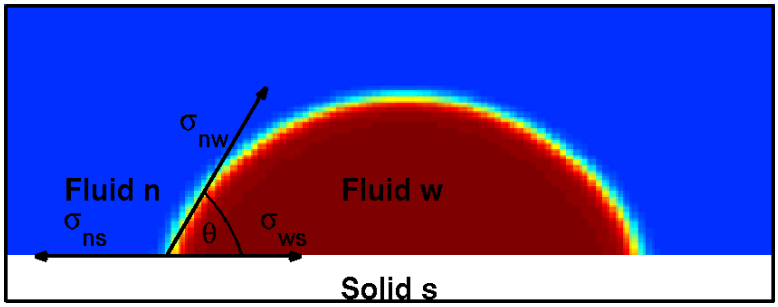

Figure 2.1: Illustration of a cross section of a liquid drop on a flat solid surface in equilibrium.

In most situations in which water enters geologic material, the contact angle is assumed to be 0° [Selker et al., 1999]. However, studies have shown that some geologic materials exhibit neutral wettability or are oil-wet [Anderson, 1987] and NAPL mixtures containing surface-active ingredients can change the porous medium from a water wet system to a NAPL wet system [Demond et al., 1994; Powers et al., 1996]. Thus, the role of wettability for multiphase flow through porous media is an active area of research [e.g., Bradford and Leij, 1996; Blunt, 2001; O'Carroll et al., 2005].

A complicating factor in the study of wettability, especially regarding the movement of fluids in porous media, is the fact that the advancing contact angle is found to be significantly larger than the receding contact angle, which is known as contact angle hysteresis [Dullien, 1992]. Additionally, the contact angle is known to be greatly affected by contamination in either the fluid or on the solid, as well as surface roughness. Thus, in a porous system in which one fluid is displacing another, the contact angle is potentially dynamic in nature [Martic et al., 2003].

2.1.2 Capillary Pressure

Capillary pressure is a fundamental variable in the study of multiphase flow in porous media. It is a measure of the tendency of a porous medium to pull in the wetting phase and repel the nonwetting phase, and it relates the discontinuity in the pressures that exists across the interface separating the fluids [Bear, 1988]. Thus, in porous media this variable is clearly defined at the pore-scale since the fluids are in contact within the pores. Formally, capillary pressure, P_c, is defined as the difference in pressures across the curved interface (in equilibrium) that separates two fluids and is given by Laplace's equation:

$$P_c = P_n - P_w = \sigma \left(\frac{1}{r_1} + \frac{1}{r_2} \right) \tag{2.2}$$

where P_n and P_w are nonwetting and wetting phase pressures, respectively, σ is interfacial tension between the two fluids and r_1 and r_2 are the principal radii of curvature of the interface. The sum of the inverse principal radii is called the mean curvature, κ. If one considers the hydraulic radius of the pore, r, Laplace's Law can be written as:

$$P_c = P_n - P_w = \frac{\sigma \cos \theta}{r} \tag{2.3}$$

Within a pore P_c is defined locally by the surface tension, contact angle and mean pore radius, however in a real porous medium all terms in Eq. 2.2 and 2.3 have the meaning of a statistical average taken over the pore space in the vicinity of a point in the porous medium, and due to the irregular, complex nature of the pore space geometry, the geometrical shape of the interface can not be defined analytically through the values of r_1 and r_2 [Bear, 1988]. For this reason idealized models (i.e., bundle of capillary tubes) were adopted in an attempt to formulate a macroscopic $P_c = f(S)$ relationship for an actual porous medium, yet these attempts to some degree have failed and the only way to derive this relationship for any given porous medium is by laboratory measurements [Bear, 1988]. The use of pore-scale numerical models have recently proven effective at predicting $P_c = f(S)$, which will be discussed in further detail in Section 2.5.

An illustration of the macro-scale capillary pressure - saturation relationship ($P_c - S$) is provided in Figure 2.2. The most noticeable feature about the curves shown in Figure 2.2 is that the $P_c - S$ relationship is hysteretic, that is, for any given saturation value, P_c will be greater for drainage than for imbibition. Hysteresis in the $P_c - S$ relationship has been attributed to the irregularity of the pore space geometry, contact angle hysteresis, Haines Jumps, the existence of trapped nonwetting phase, and changes in the solid phase configuration (i.e., swelling/shrinking of a clay soil) [Hillel, 1998]. More recently, Hassanizadeh and Gray [1990, 1993] argued that

hysteresis is a result of assuming the very complex P_c function depends upon saturation alone. They went on to argue that the most important missing variable is the fluid-fluid specific interfacial area, a_{nw}, and by expanding the functional relationship to include a_{nw}, that is $P_c = f(S, a_{nw})$, may result in a unique surface. Whether a unique surface is obtained for $P_c = f(S, a_{nw})$ is an open question and currently there are many research efforts, including this one, working to answer this question. Further details pertaining to the $P_c - S - a_{nw}$ relationship will be discussed in Sections 2.2-2.5.

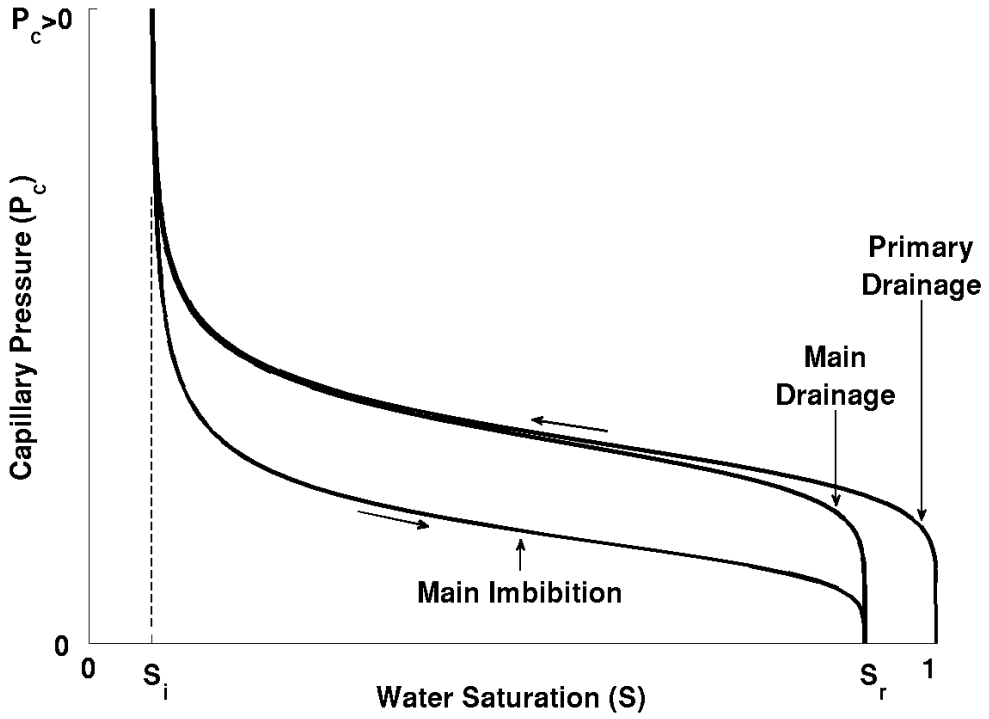

Figure 2.2: Illustration of typical macroscopic $P_c - S$ curves.

Typically, the macro-scale $P_c - S$ curves start with a completely saturated porous medium. Primary drainage is initiated by injecting the nonwetting phase very slowly, which increases the capillary pressure in the system. The nonwetting phase does not start to displace the wetting phase until the local capillary pressure has exceeded the capillary pressure associated with the largest pore in contact with the bulk nonwetting phase. Further increases in P_c result in displacement of the wetting phase until the primary drainage curve asymptotically approaches

the irreducible wetting phase saturation, S_i. The irreducible saturation refers to the trapped wetting phase, in the form of pendular rings and wetting phase bridges, that can not be displaced by further increases in the externally controlled P_c since they are not hydraulically connected to the bulk wetting phase. Dullien [1992], however states that the concept of irreducible saturation only has limited validity since many natural porous systems have wetting phase films that form continuous wetting phase pathways that allow for further reduction of saturation at higher P_c when sufficient time is allowed for displacement. Additionally, Hassanizadeh and Gray [1993] and Corey [1986] question the validity of S_i since it is often dependent on how S_i is measured, and the pressure difference between the two phases measured outside the porous medium do not necessarily represent the capillary pressure within the porous medium for the disconnected wetting phase. Corey [1986] goes on to state that due to the uncertainty in S_i, it should be interpreted as a parameter useful for curve-fitting purposes.

Main imbibition occurs, as depicted in Figure 2.2, when the capillary pressure is reduced upon the completion of primary drainage. The wetting phase displaces the nonwetting phase and there is a gradual increase in saturation at high P_c since the wetting phase enters the smallest pores first. As P_c decreases, larger and larger pores become available for the wetting phase to invade. This continues until residual nonwetting phase saturation is obtained, which is always less than 100 % saturation. Residual nonwetting phase saturation, S_r, represents the amount of entrapped nonwetting phase that remains in the porous medium when the externally measured P_c is decreased from a high value to zero [Morrow, 1970]. According to Miller et al. [1998] most of the values obtained from imbibition experiments represent the maximum possible residual nonwetting phase saturation. The formation of S_r is a function of the geometry of the pore space, wettability, viscosity ratio, interfacial tension, density difference and displacement rates [Miller et al., 1998]. Furthermore, values of S_r have been shown to be a function of saturation history, namely the initial saturation from which imbibition was initiated, and many numerical models include a nonlinear relationship between the initial and maximum residual saturation to predict S_r [Mualem, 1974; Parker and Lenhard, 1987; Lenhard et al., 2004].

Upon completion of main imbibition, main drainage is often measured, which is similar to primary drainage, except the initial saturation is S_r. Main imbibition and main drainage curves are generally the minimal requirements for numerical modeling. Any subsequent imbibition or drainage curves starting from S_i and S_r, respectively will follow the main imbibition and drainage curves closely. Any imbibition or drainage curves that are initiated between the values of S_i and S_r are called scanning curves and are bounded by the main imbibition and drainage curves (see [Dullien, 1992]).

2.1.3 Relative Permeability

Although this research only focuses on the role of capillary pressure and interfacial area in multiphase porous systems, the concept of relative permeability is a fundamental aspect of the theory of multiphase flow processes and is discussed here briefly. Intrinsic permeability is a property of the porous medium and measures the ability of the porous medium to conduct fluid, thus it is a continuum concept that is valid only at the REV scale. In porous systems containing two or more immiscible fluids, the available cross sectional area of the flow path for each fluid is less than the total cross sectional area of the pore space [Bear, 1988]. The reduction in the cross section directly affects the permeability of the system, thus the concepts of effective permeability and relative permeability have been adopted. Because two phases are moving in the pore space, each phase interferes with the other phase and the effective permeability can not exceed the intrinsic permeability. The effective permeability for a given phase is defined as:

$$\boldsymbol{k}_\alpha = \boldsymbol{k}_{r\alpha}\boldsymbol{k} \tag{2.4}$$

where $\boldsymbol{k}_{r\alpha}$ is the relative permeability for that phase and $\boldsymbol{k}$ is the intrinsic (or saturated) permeability. Relative permeability is an empirical function that describes the reduction of $\boldsymbol{k}$ due to the presence of the other phase. Dullien [1992] and Bear [1988] provide thorough discussions of the $\boldsymbol{k}_{r\alpha} - S$ relationship and its hysteretic nature. Thus, for a full description of multiphase flow through porous media one needs information about the $P_c - S - k_r$ relationship.

2.1.4 Interfacial Area

The main distinguishing feature between single phase and multiphase flow is the existence of the fluid-fluid interface separating the immiscible fluids. These interfaces are very thin transition zones between phases that can provide mechanisms for the storage and exchange of mass, momentum and energy [Muccino et al., 1998]. In the study of multiphase systems, fluid-fluid interfacial area per volume has typically been considered important for processes associated with transport phenomena and not so much for flow phenomena. Interfacial area per volume is typically not considered for flow phenomena since extensions of Darcy law are assumed to adequately describe the simultaneous flow of two fluids (see Section 2.2 and 2.3). However, Gray and Hassanizadeh [1998] argue that Darcy's law neglects driving forces for flow associated with adjacent interfaces and phases.

In regards to transport processes the fluid-fluid interfaces are controlling factors in evaporation, volatilization of organic chemicals, sorption and transport of organic contaminants, colloid particle and microbial pathogens, and dissolution of contaminants into passing groundwater.

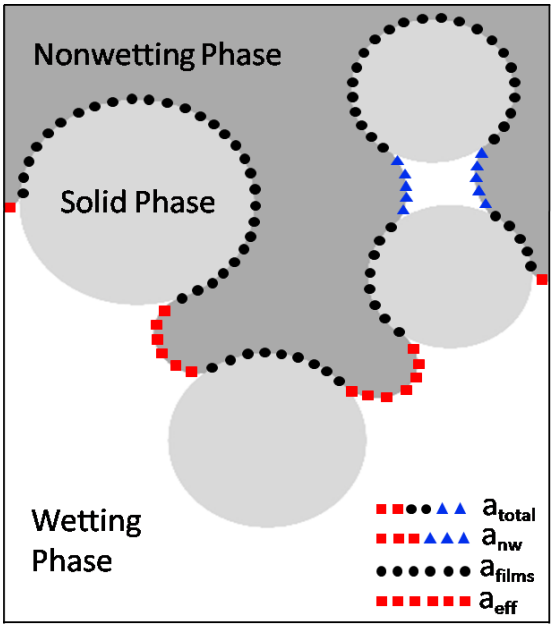

Figure 2.3: Illustration of the components of the fluid-fluid interfacial area per volume.

In studies of NAPL dissolution into groundwater the following rate-limited mass transfer model has been employed [Miller et al., 1990; Powers et al., 1992]:

$$J = k_f a_{nw} \left(C_s - C \right) \tag{2.5}$$

where J is the solute mass flux, k_f is the mass transfer coefficient, a_{nw} is the fluid-fluid interfacial are per volume, C_s is the solute concentration in thermodynamic equilibrium with the pure organic liquid and C is the solute concentration in the bulk aqueous phase. Due to the difficulty of measuring a_{nw}, a lumped mass transfer coefficient, $\kappa = k_f a_{nw}$ is often determined empirically for specific experimental geometries and flow systems [Grant and Gerhard, 2007a]. Powers et al. [1992] conducted steady-state NAPL dissolution experiments and concluded that greater understanding of factors influencing the NAPL-water interfacial area is required to adequately describe the system.

Figure 2.3 illustrates the various components of fluid-fluid interfacial area per volume that have been defined in the literature. The total fluid-fluid interfacial area per volume, a_{total}, is generally thought to be composed of wetting phase film area, a_{films}, and capillary-associated area, a_{nw}, thus $a_{total} = a_{film} + a_{nw}$. a_{film} pertains to nonwetting interfaces in contact with the wetting phase films that exist on solids of pores occupied by the nonwetting phase, whereas a_{nw}

includes all nonwetting phase in contact with the bulk mobile wetting phase and the immobile wetting phase (i.e., pendular rings and bridges) [Gladkikh and Bryant, 2003]. Additionally, a_{eff} is defined as the component of a_{nw} that is in contact with only the bulk mobile wetting phase.

2.2 Traditional Macro-scale Multiphase Flow Modeling

2.2.1 Simultaneous Flow of Two Immiscible Fluids

Macroscale models are based on the concept of a continuum, and assume that the phases are spatially continuous over an REV. The fundamental equations governing multiphase flow, assuming there is no mass transfer between phases, are given by the conservation of mass within each phase [Bear, 1988; Miller et al., 1998; Chen et al., 2006]:

$$\frac{\partial \left(\phi \rho_\alpha S_\alpha\right)}{\partial t} = -\nabla \cdot \left(\rho_\alpha \boldsymbol{q}_\alpha\right) \tag{2.6}$$

where ϕ is the porosity, ρ is the density of the fluid, S is the saturation, $\boldsymbol{q}$ is the flux and the subscript $\alpha = n, w$ denotes the nonwetting and wetting phase. In Eq. 2.6 it is often assumed that a heuristically altered form of Darcy's law applies to the simultaneous flow of two fluids in porous media and $\boldsymbol{q}_\alpha$ is defined as:

$$\boldsymbol{q}_\alpha = -\frac{1}{\mu_\alpha} \boldsymbol{k}_{r\alpha} \boldsymbol{k} \left(\nabla p_\alpha - \rho_\alpha g\right) \tag{2.7}$$

where $k_{r\alpha}$, k, p_α and μ_α is the relative permeability, intrinsic permeability, pressure and viscosity, respectively, for phase α. Substituting Eq. 2.7 into Eq. 2.6 yields:

$$\frac{\partial \left(\phi \rho_\alpha S_\alpha\right)}{\partial t} = \nabla \cdot \left(\rho_\alpha \frac{\boldsymbol{k_\alpha k}}{\mu_\alpha} \left(\nabla p_\alpha - \rho_\alpha g\right)\right) \tag{2.8}$$

which represents two equations with nine unknowns, namely ρ_n, ρ_w, S_n, S_w, p_n, p_w, $\boldsymbol{k}$, $\boldsymbol{k}_{rn}$ and $\boldsymbol{k}_{rw}$. Thus, to close the system seven additional equations are required. For ρ_n and ρ_w an equation of state (EOS) is required that defines the equilibrium relationship between density, pressure and temperature. In most environmental applications it is assumed that the system is isothermal and the fluid is incompressible, simplifying the system since the fluid density is assumed constant. The equation relating the saturations is simply $S_w + S_n = 1$, which states that the two fluids occupy the entire pore space. The two pressures p_n and p_w are related by the empirical $P_c - S$ relationship where $P_c = p_n - p_w = f(S_w)$. Additionally, $\boldsymbol{k}$, $\boldsymbol{k}_{rn}$ and $\boldsymbol{k}_{nw}$

are defined empirically, where $\boldsymbol{k}$ is typically a function of porosity, pore-size distribution and solid surface area, and $\boldsymbol{k}_{rn}$ and $\boldsymbol{k}_{rw}$ are taken as function S_w.

2.2.2 Richard's Equation for Flow in the Vadose Zone

In the vadose zone multiphase flow involves water and air and it is commonly assumed that the soil air does not hinder the movement of water. This is a reasonable assumption if the air phase is continuous and connected to the external atmosphere [Hillel, 1998]. The volumetric water content, θ_w, is commonly used to quantify the soil moisture in the vadose zone rather than saturation, and θ_w is defined as:

$$\theta_w = V_w/V_t \tag{2.9}$$

where V_w is the volume of the water contained in the pores and V_t is the total volume of the porous medium. It follows that at $S_w = 1$, $\theta_w = \phi$ where ϕ is the porosity. Volumetric water content plays a critical role in many of the processes encountered in the vadose zone, thus the unsaturated flow equations are often formulated in terms of θ_w where the hydraulic conductivity, K, is empirically defined as a function of water content. Darcy's law for unsaturated flow is written as:

$$q = K(\theta_w)\nabla H \tag{2.10}$$

where total hydraulic head, $H = p_w/\rho_w g + z$, is the sum of the pressure head and the elevation head. Combining Eq. 2.10 with the continuity equation yields Richard's Equation [e.g., Hillel, 1998; Selker et al., 1999]:

$$\frac{\partial \theta_w}{\partial t} = \nabla\cdot\left(K(\theta_w)\nabla H\right). \tag{2.11}$$

An alternate form of Richard's Equation can be obtained by substituting the suction head (the negative of the pressure head), Ψ, and the elevation head for H and taking the derivative of the elevation head:

$$\frac{\partial \theta_w}{\partial t} = -\nabla\cdot\left(K(\theta_w)\nabla\Psi\right) + \frac{\partial K(\theta_w)}{\partial z}. \tag{2.12}$$

In order to solve Eq. 2.12 a relationship is required for $K(\theta_w)$ and $\Psi(\theta_w)$, which are the same empirical relationships required by Eq. 2.8.

2.2.3 Empirical Relationships

Empirical (or constitutive) relationships serve to describe the essential features of a given system at the scale of interest while decreasing the number of variables needed to describe the system

if one started at a smaller scale [Miller et al., 1998]. In most cases, empirical relationships are required to close a system of equations that includes more unknown variables than equations. In multiphase flow through porous media the empirical $P_c - S - k_r$ relationship is of central importance as was apparent in Section 2.2.1 and 2.2.2. Since the research presented here has focused primarily on the $P_c - S$ relationship, there will be no detailed discussion pertaining to the $S - k_r$ relationship and the link between the two. Briefly, measurement of the $S - k_r$ relationship is generally cumbersome, costly and very time consuming, consequently many attempts have been made to develop indirect methods which predict the $S - k_r$ from the more easily measured $P_c - S$ curves [Vogel et al., 2001]. It is noted that the $S - k_r$ relationship is currently an active area of research with numerous open questions [e.g., Miller et al., 1998; Li et al., 2005].

Several empirical $P_c - S$ relationships are available in the literature, which attempt to relate capillary pressure to medium and fluid properties, and the wetting phase saturation, S, however, most of these models are based on idealized porous systems such as a capillary tube or bundle of capillary tubes [Bear, 1988].

Leverett [1941] proposed the J-Leverett function based on dimensional analysis; one advantage of this function is that it allows the $P_c - S$ curves to be scaled as a function of permeability, surface tension and wettability. Furthermore, this relationship allows $P_c - S$ curves measured with air and water to be scaled for use in simulations involving different fluid-fluid pairs [Lenhard and Parker, 1987; Parker and Lenhard, 1987]. This relationship has been found to be very useful for correlating P_c within a specific lithologic type [e.g., Dumore and Schols, 1974], however, the main limitation is that the J-Leverett function is incapable of accounting for individual pore structures from different samples [Dullien, 1992].

Brooks and Corey [1964] (BC model) and van Genuchten [1980] (VG model) proposed empirical relationships that have become popular for use in numerical modeling of multiphase flow processes [e.g., Simunek et al., 1999; White and Oostrom, 2000; Luckner et al., 1989; Kueper and Frind, 1991; Gerhard and Kueper, 2003]. The BC model is a power-law that leads to a well defined nonwetting phase entry pressure in the $P_c - S$ curves. The VG model is a modified version of the BC model that enables a more accurate description of the observed soil hydraulic data near saturation. These models are functions of the porous medium and fluid properties, and thus the model parameters are different for every system [Miller et al., 1998]. Additionally, these empirical models have been refined to include hysteresis [e.g., Scott et al., 1983; Lenhard and Parker, 1987; Parker and Lenhard, 1987], wettability [e.g., Bradford and Leij, 1996; O'Carroll et al., 2005] and residual nonwetting phase saturation [e.g., Lenhard and Parker, 1987; Parker and Lenhard, 1987; Luckner et al., 1989]. Thus, the fundamental empirical models are limited in their applicability and require further refinement to accurately describe the important characteristics of multiphase flow. Although, these approaches have been shown

to work for the laboratory systems in consideration, they do not address the question of whether some fundamental underlying physical process is being ignored in the empirical relationship, or the overall modeling approach.

2.3 Nontraditional Macro-scale Multiphase Flow Modeling

An alternative approach for the development of macro-scale multiphase flow models is to develop general equations based on first principles, rather than assuming Darcy's law is the fundamental expression [Muccino et al., 1998]. In this manner, the important variables affecting the simultaneous flow of two (or more) immiscible fluids through porous media may be included in the conservation of mass, momentum, and energy at the macro-scale.

It is widely recognized that the fundamental difference between single phase flow and multiphase flow is the existence of fluid-fluid interfaces. However, only a few researchers have accounted for the behavior of the interfaces explicitly in their multiphase models [e.g., Hassanizadeh and Gray, 1990, 1993; Gray, 1999; Gray et al., 2002; Murdoch and Hassanizadeh, 2002; Wei and Muraleetharan, 2002; Muraleetharan and Wei, 1999]. The inclusion of interfaces and interfacial dynamics results in additional geometric variables in the conservation equations (i.e., a_{nw}) that must be supplemented with additional evolutionary equations that describe the interaction between these variables [Gray et al., 2002]. Furthermore, Gray [1999] showed that the standard multiphase flow equations (i.e., Eq. 2.8 and 2.12) were very restrictive forms of the general equations developed from their approach.

An important theoretical result from this approach is that capillary pressure was shown to be a function of fluid-fluid interfacial area per volume, as well as saturation [Hassanizadeh and Gray, 1990, 1993; Gray, 1999]. Numerous authors have developed relationships for $P_c - S - a_{nw}$ [Leverett, 1941; Morrow, 1970; Bradford and Leij, 1997; Oostrom et al., 2001; Dobson et al., 2006; Grant and Gerhard, 2007a], however these are generally implemented as sub-models of the traditional $P_c - S$ relationship. Thus, in the literature the importance of interfacial area per volume to flow and transport processes is recognized, however it is not directly incorporated in the macroscopic equations for multiphase flow.

Hassanizadeh and Gray [1993] hypothesized that the inclusion of the fluid-fluid interfacial area per volume into the functional dependence of capillary pressure (i.e., $P_c = f(S, a_{nw})$) could eliminate hysteresis observed in the traditional $P_c - S$ relationship. This is true only if the surface for $P_c - S - a_{nw}$ is unique. Muccino et al. [1998] provided an example of how this would work for a simple capillary tube system, however they stated that further experimental and numerical studies are required to test the hypothesis.

2.4 Experimental Methods

2.4.1 Capillary Pressure-Saturation Methods

Laboratory methods for measuring the $P_c = f(S)$ relationship are typically divided into three groups:

1. static (or displacement) methods, based on the establishment of successive states of hydrostatic equilibrium,
2. steady state methods, based on the establishment of successive states of steady flow, and
3. unsteady state (transient) methods, based on the measurement of P_c and saturation during fluid displacement.

Static measurements are the most commonly reported, whereas steady state measurements are usually applied in conjunction with relative permeability measurements. Transient measurements have gained some interest since they do not take as long to measure as static curves. Furthermore, there is considerable debate regarding the use of static $P_c - S$ measurements for transient multiphase flow modeling [e.g., Muccino et al., 1998; Hassanizadeh et al., 2002], since numerous authors have shown that $P_c - S$ curves are dependent upon the dynamics of flow during and/or prior to measurement [Topp et al., 1967; Davidson et al., 1966; Smiles et al., 1971; Welge, 1948]. The term quasi-static or quasi-equilibrium is often used since static conditions are often difficult to establish with certainty, and thus are assumed somewhat arbitrarily [e.g., Hassanizadeh et al., 2002]. The term quasi-static has also been used to describe transient $P_c - S$ measurements that show no observable differences from static measurements [e.g., Wildenschild et al., 1997, 2001]. The use of the term quasi-static (or near-equilibrium) in subsequent chapters refers to conditions in which the system has been allowed to equilibrate for only a short time, thus the state of equilibrium is not certain.

When measuring $P_c - S$ curves the porous medium consist of either packed material, or undisturbed samples. Since the structure of the porous medium affects the $P_c - S$ curves, it is best to use an undisturbed sample, however, many investigations addressing fundamental multiphase flow research use repacked, unconsolidated, coarse sand material [e.g., Topp et al., 1967; Chen et al., 1999; Chen and Kibbey, 2006; Gerhard and Kueper, 2003; Lenhard and Parker, 1987; Liu et al., 1998; Wildenschild et al., 2001]. The pressure (retention) cell dimensions typically have diameters ranging from 5-8 cm and heights ranging from 1-6 cm. The porous medium is usually in hydraulic contact with the fluids through a porous plate or membrane and the pressure is measured in the fluids outside the porous medium [Dane and Topp, 2002, pg. 675]. In some experiments, tensiometers have been placed inside the porous medium or on

the sides of the columns [Topp et al., 1967; Sakai and Illangasekare, 2007; Wildenschild et al., 2001]. Traditionally, static $P_c - S$ curves are obtained by establishing a series of equilibria by controlling the pressure in the fluid phases and allowing one fluid to drain out of the system until equilibrium saturation is reached [Dane and Topp, 2002, pg. 675]. An alternative approach consists of adding or extracting a precise amount of fluid to the system, then allowing for the fluids to redistribute and the pressure head to equilibrate with time [Dane and Topp, 2002, pg. 698]. The main purpose of this approach is to reduce equilibration time required [Dane and Topp, 2002, pg. 702]. In the experiments presented in this research the fluid saturation was controlled and the pressure head was allowed to equilibrate.

2.4.2 Interfacial Area-Saturation Methods

Experimental methods for measuring the fluid-fluid interfacial areas in porous media began to appear in the late 1990's [Dane and Topp, 2002, pg. 783]. The methods developed at that time consisted of measuring the interfacial accumulation of various surface-active chemicals (i.e., surfactants) [Saripalli et al., 1997; Kim et al., 1999b,a; Brusseau et al., 1997; Schaefer et al., 2000]. The general idea is that when an aqueous solution with a known surfactant concentration is applied to a porous medium that contains a wetting and nonwetting fluid, some of the surfactant molecules adsorb onto the interface between the two fluids. If the unit area covered by each surfactant molecule at the interface is known, measuring the total mass (moles) of surfactant adsorbed at the interface permits the estimation of the fluid-fluid interfacial area per volume [Dane and Topp, 2002, p. 784].

Another approach for experimental measurement of fluid-fluid interfacial area is through the analysis of high resolution x-ray computerized microtomographic (CMT) image data. When coupled with a synchrotron source, this method is capable of producing 3D images of the internal structure of small samples with resolutions on the order of 1 μm [Flannery et al., 1989]. Details pertaining to acquisition of CMT image data are beyond the scope of this discussion, however more information can be found in Lindquist et al. [2000] and Wildenschild et al. [2002, 2005]. Briefly, in applications addressing multiphase flow in porous media, one of the fluids is typically doped with an x-ray absorbent in order to enhance the contrast between fluids. The resulting CMT gray-scale image is a 3D array of x-ray attenuation coefficients. Figure 2.4 illustrates a typical 2D vertical slice of the 3D CMT data during a drainage cycle. The saturations and interfacial areas are subsequently quantified from the gray-scale image data by means of various image analysis techniques. Although numerous authors have used CMT imaging techniques to obtain high resolution data for porous media, only a few studies have investigated the $a_{nw} - S$ relationship [e.g., Culligan et al., 2004, 2006; Brusseau et al., 2007, 2008; Costanza-Robinson et al., 2008].

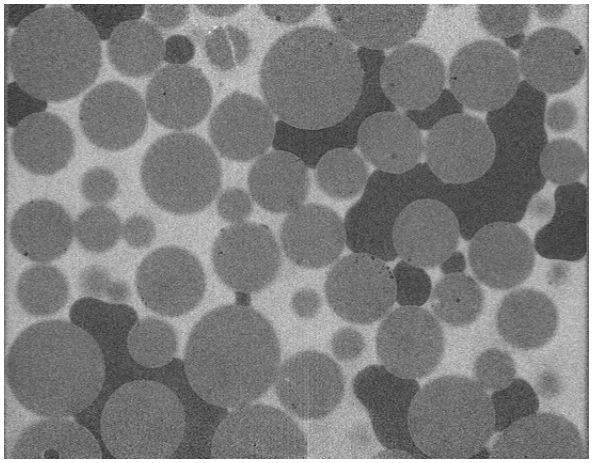

Figure 2.4: Illustration of typical vertical cross section of the gray-scale CMT data. The light gray represents the wetting phase, the gray represents the beads and the dark gray is the nonwetting phase.

It is important to note that there are significant differences in the fluid-fluid interfacial area per volume measured via tracer techniques and CMT image analysis. Tracer techniques measure a_{total} and are capable of measuring the interfacial area associated with microscale roughness [Kim et al., 1999a]. Fluid-fluid interfacial area estimates obtained via image analysis are dependent upon the resolution of the images and a_{films} are typically not resolved, thus a_{nw} is estimated. Based on certain assumptions (see Chapter 4), estimates of a_{total} and a_{eff} may be obtained from CMT image data. Additionally, CMT data allows for the investigation of the spatial statistics of the interfaces and disconnected phases, which can not be obtained with interfacial tracer techniques.

2.4.3 Capillary Pressure-Saturation-Interfacial Area Methods

There are very few experimental data sets reported in the literature pertaining to $P_c - S - a_{nw}$ and these have only appeared within the last decade. It also noted that there is lack of consensus as to which component of the fluid-fluid interfacial area the different $P_c - S - a_{nw}$ relationships correspond. Based on illustrations presented by Hassanizadeh and Gray [1993] the $P_c - S - a_{nw}$ relationship corresponds to capillary-associated, a_{nw} or a_{eff} as they are defined in Section 2.1.4. However, the earliest $P_c - S - a_{total}$ measurements to appear in the literature were obtained via interfacial tracer tests for unsaturated sands [Kim and Rao, 1997]. In these experiments the drainage $P_c - S$ curve was measured separately from the interfacial tracer measurements

and the data from the two experiments were combined to investigate $P_c - S - a_{total}$. Recently, [Chen and Kibbey, 2006] reported multiple drainage and imbibition $P_c - S - a_{total}$ curves in which a tracer test was performed while simultaneously measuring static $P_c - S$ curves.

Culligan et al. [2004, 2006] measured quasi-static drainage and imbibition $P_c - S$ curves and from 3D CMT images estimated a_{nw} for each point on the curve. Similar experiments are presented in this manuscript (see Chapter 4) and in addition to a_{nw}, a_{eff} estimates are presented. Cheng et al. [2004] and Chen et al. [2007] presented $P_c - S - a_{nw}$ obtained from static drainage and imbibition experiments performed on a 2D micromodel and a_{nw} was estimated from images obtained from digital microscopy. Their experiments included multiple scanning curves in addition to main imbibition and drainage, thus they were able to evaluate the resulting surface for $P_c - S - a_{nw}$. Cheng et al. [2004] observed similar surfaces for both imbibition and drainage and concluded that the addition of the a_{nw} into the functional relationship for $P_c - S$ eliminated hysteresis. It is noted, however, that their curves only spanned saturations of 0.6-1.0, thus their conclusion is based off on an incomplete saturation range.

2.5 Pore Scale Modeling

2.5.1 Survey of Models

In the past few decades, the number of pore-scale numerical investigations of multiphase flow processes has increased significantly. Numerical modeling approaches are appealing since experimental measurements are often extremely time consuming, expensive, and limited in the amount and types of data that can be obtained. Additionally, there has been an increase in pore-scale morphology information, which is typically obtained from high resolution image data or simulated media.

Once the pore geometry is determined numerous methods for modeling pore-scale multiphase flow and transport phenomena are available from which to choose. Conventional approaches include computational fluid dynamics (CFD) and molecular dynamics (MD). In general, CFD involves numerical solution of the Navier-Stokes equations and molecular dynamics involves simulating the interactions between many particles (i.e., fluid molecules), then averaging the resulting particle configurations to obtain the quantity of interest. The computational costs associated with the treatment of moving interfaces limits CFD methods to flows in which interfacial area is very small [Ferziger and Perić, 2002]. The finite total time-length of the trajectory and size of the simulated system are major limitations of the MD method where the simulation of a few tens or even hundreds of thousands particles is still much smaller than a macroscopic object and a span of a few tens or even hundreds of nanoseconds is still too short compared to macroscopic times [Simdyankin and Dzugutov, 2003]. Additionally, Frisch et al.

[1986] showed that the molecular, or atomistic, motion within fluids need not be so detailed as real molecular dynamics in order to produce realistic fluid mechanics.

Some methods that have recently proven successful for simulating pore-scale multiphase flow through porous media include pore network, smooth particle hydrodynamics (SPH) and lattice-Boltzmann. Pore network models represent the porous media using pore bodies and throats of simple geometric shapes (i.e., spheres, triangles, cylinders, etc.). In the past, pore network models were developed based on simplifying assumptions about the pore structure (i.e., bundle of capillary tubes, an idealized pore size distribution) and thus the resulting simulations were limited in their predictive capabilities. The first network model based on interconnected sites and bonds (pores and throats) was introduced by Fatt in 1956 [Dullien, 1992]. Since then many studies have focused on the structure of networks for multiphase flow applications. Difficulties are encountered in selecting the appropriate shapes, sizes, locations, connections and orientations of the pores and throats. Furthermore, network models require calibration of the network geometry for accurate quantitative predictions [Pan, 2004]. The calibration step consists of (1) the adjustment of network parameters to match the main branches of the $P_c - S$ curve, or (2) deriving network parameters from the topology of the porous medium, obtained from high resolution image data or simulated media [Pan, 2004]. However, once constructed, network models are capable of simulating flow phenomena by constructing rules or by solving flow equations within the simplified geometries [Blunt, 2001]. Additionally, for static or quasi-static multiphase processes, the computational requirements are negligible, compared to other pore-scale methods. Thus, numerous network models (some with hundreds to thousands of data points) have been presented in the literature that simulate the $P_c - S$ and $P_c - S - a_{nw}$ relationships [e.g., Reeves and Celia, 1996; Held and Celia, 2001; Dalla et al., 2002; Gladkikh and Bryant, 2003; Joekar-Niasar et al., 2007].

SPH methods involve the discretization of the Navier-Stokes equations spatially, leading to a set of ordinary differential equations (ODEs) with respect to time, which are solved via time integration. SPH differs from conventional CFD methods in that it is a meshfree particle method that is Lagrangian in nature, making it attractive for tracking moving interfaces or free surfaces [Liu and Liu, 2003]. The particle nature of SPH models allows fluid-fluid and fluid-solid interactions to be modeled through simple particle-particle interactions, which allows for simulations of surface tension and well defined contact angles under both static and dynamic conditions [Tartakovsky and Meakin, 2005a]. Disadvantages of SPH include "artificial" contributions to both the viscosity and surface tension, and prescribed flux and/or pressure boundary conditions for flow equations are quite difficult [Tartakovsky and Meakin, 2005b; Tartakovsky et al., 2007]. Although SPH is a promising method for simulating multiphase flow, no simulations of the $P_c - S$ relationship have been reported in the literature.

Lattice-Boltzmann (LB) methods have become very popular in the realm of multiphase flow and transport. The LB method is a discrete velocity model constructed on a discrete lattice that approximates the incompressible Navier-Stokes equations at each lattice point. The fundamental idea behind the LB method is the construction of simplified kinetic models that incorporate the essential physics of pore-scale processes such that the macro-scale averaged properties obey the desired macroscopic equations [Chen and Doolen, 1998]. The truly microscopic methods used in the past (i.e., molecular dynamics) are not capable of providing this comparison [Succi, 2001]. An advantage of the LB method is that the kinetic equations and boundary conditions are imposed locally allowing for (1) the exact representation of the pore geometry (i.e., obtained from high resolution image data), (2) the simulation of moving boundaries between phases, and (3) a fully parallel algorithm. Furthermore, numerous authors have simulated $P_c - S$ curves with favorable results [e.g., Pan et al., 2004; Vogel et al., 2005; Schaap et al., 2007; McClure et al., 2004]. McClure et al. [2004] estimated interfacial area for the resulting $P_c - S$ simulations, however no comparison with experimental data was presented.

2.5.2 Lattice-Boltzmann Modeling

The LB method evolved from an earlier method known as Lattice-Gas Cellular Automata (LGCA). A cellular automaton is a regular discrete lattice (i.e., grid) in which the sites can represent a finite number of states [Rothman and Zaleski, 1997]. In a cellular automaton the particles are represented by Boolean variables (i.e., 1 indicates that a given site is occupied, whereas 0 indicates the site is empty) and the system evolves in discrete time based on simple rules involving the nearest neighbors, and the requirement that mass and momentum be conserved [Rothman and Zaleski, 1997]. The first LGCA model for of the Navier-Stokes equations was introduced by Uriel Frisch, Brosl Hassacherler and Yves Pomeau in 1986 [Frisch et al., 1986]. Their model was constructed on a hexagonal lattice in which the particles moved at the same speed and there were only 6 velocities.

Shortly thereafter it became apparent that there were some limitations to the LGCA method when applied to hydrodynamics, which include: (1) statistical noise due to Boolean variables; (2) exponential complexity making it virtually impossible to perform 3D simulations; and (3) LGCA is restricted to low Reynolds number flows [Succi, 2001, Ch. 2]. The LB method was developed mainly in response to statistical noise exhibited by LGCA methods and soon after it was discovered that all other anomalies present in LGCA could be eradicated with by the LB method [Succi, 2001]. McNamara and Zanetti [1988] introduced the first LB method which was based on the simple idea of replacing the Boolean variables with the corresponding ensemble-averaged populations and solving the Boltzmann equation.

In the remainder of this section a brief discussion of the LB modeling technique will be presented. There are numerous articles [e.g., Chen and Doolen, 1998; Shan and Chen, 1993, 1994; Shan and Doolen, 1996; Swift et al., 1995, 1996] and texts [Rothman and Zaleski, 1997; Succi, 2001; Sukop and Thorne, 2006] that describe the LB technique in full detail, thus the discussion here will focus more on recent results from Schaap et al. [2007] and how those results pertain to this research.

The LB method solves the Boltzmann equation for an ensemble-averaged distribution of particles on a discrete, finite lattice connected by fixed paths along which the particles move. Mathematically, a lattice is defined as a collection of nodes in 1-, 2- or 3D space, on which an ensemble-averaged distribution of particles, $f_i(\boldsymbol{x}, t)$, is streamed to the neighboring nodes by way of a set of fixed velocity vectors $\boldsymbol{e}_i$ where the subscript $i = 0, 1, ..., b$ represents each velocity. The set of $\boldsymbol{e}_i$ are determined by the lattice dimensions and the lattice neighbors included in the formulation. For example, Figure 2.5 shows a 2D lattice with nine velocity vectors. The notation D2Q9 is standard in the LB literature and refers to a 2D lattice with 9 velocity vectors, as depicted in Figure 2.5. In the D2Q9 model there are only three speeds at which the particles travel and these are determined by the distance $f_i(\boldsymbol{x}, t)$ must travel to the neighboring node. It follows that in the D2Q9 model depicted in Figure 2.5, the magnitude of $\boldsymbol{e}_0$ is 0 lattice units per time step (or $lu\ ts^{-1}$), the magnitude of $\boldsymbol{e}_0$ - $\boldsymbol{e}_4$ is 1 $lu\ ts^{-1}$ and the magnitude of $\boldsymbol{e}_5$ - $\boldsymbol{e}_8$ is $\sqrt{2}\ lu\ ts^{-1}$. These velocities are extremely convenient since the x- and y-components of $\boldsymbol{e}_i$ are 0, 1 or -1.

The macroscopic density and momentum are defined as moments of the microscopic particle distributions:

$$n(\boldsymbol{x}, t) = \sum_{i=0}^{b} f_i(\boldsymbol{x}, t), \tag{2.13}$$

$$\boldsymbol{u}(\boldsymbol{x}, t) = \frac{1}{n(\boldsymbol{x}, t)} \sum_{i=0}^{b} f_i(\boldsymbol{x}, t)\, \boldsymbol{e}_i(\boldsymbol{x}, t). \tag{2.14}$$

The evolution of the particle distributions in time and space is modeled via stream and collide steps. The first operation in each time step is the streaming operation, in which each particle distribution is advanced to the next lattice site according to its velocity. This can be thought of as simply moving each f_i to its appropriate new location and leaving everything else unchanged. The second operation is to simulate the particle interactions at the new location via the discrete Boltzmann equation. In addition, the collision operator was greatly simplified by using a single relaxation time, and the discrete Boltzmann equation is written as [Chen and Doolen, 1998]:

$$f_i(\boldsymbol{x} + \boldsymbol{e}_i, t+1) = f_i(\boldsymbol{x}, t) - \frac{1}{\tau}\left[f_i(\boldsymbol{x}, t) - f_i^{eq}(\boldsymbol{x}, t)\right] \tag{2.15}$$

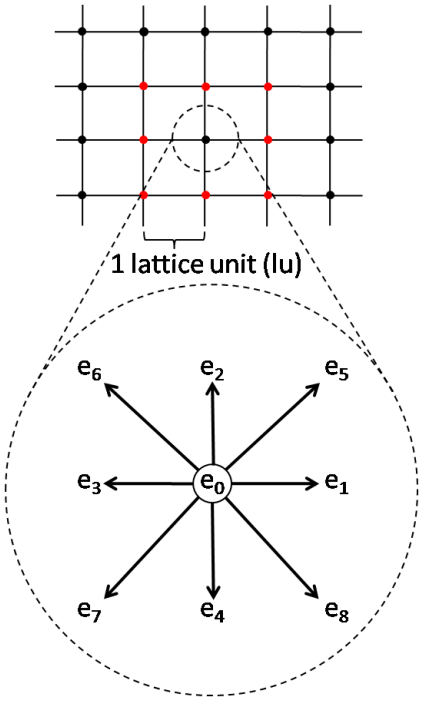

Figure 2.5: Illustration of a D2Q9 lattice. The vectors $\boldsymbol{e}_i$ represent the nine velocities in this model.

where τ is the relaxation time that determines the fluid viscosity and f_i^{eq} is the equilibrium distribution function. The appropriate form of f_i^{eq} is determined by the lattice geometry, the velocity vectors and the conservation of mass and momentum. It is quite extraordinary that the Navier-Stokes equations are recovered at the macro-scale via stream and collide rules that simply conserve mass and momentum on a lattice with sufficient symmetry.

Furthermore, the stream and collide algorithm allows a simple bounce-back rule to be used at all solid phase boundaries. The bounce-back rule states a particle distribution that should advance to a solid site during any given streaming operation is simply assigned to the opposite particle distribution (i.e., in Figure 2.5, if f_1 were to advance into a solid, then $f_3 = f_1$). Improved schemes have been presented in the literature [e.g., Pan et al., 2004], however the accuracy of the standard bounce-back algorithm is sufficient for most applications.

Different methods have been proposed to extend the LB framework to multiphase flow. The interaction between the fluids via interfacial tension is the key to simulating multiphase flow. Furthermore, in porous media applications, the interaction between the fluids and the solids (i.e., the contact angle) must be incorporated. Gunstensen et al. [1991] introduced the first

LB model for immiscible fluids incorporating the interaction between fluids and solids based on color gradients. A slightly improved method was presented by Shan and Chen [1993], in which the interaction between fluids and solids was incorporated through interaction potentials. In these two methods the interaction between the fluids and solids was incorporated phenomenologically through the macroscopic velocity. These methods are appealing since they are relatively straightforward extensions of the single phase LB model and easy to implement. Swift et al. [1995, 1996] and Orlandini et al. [1995] proposed a method that included the free-energy functional in the derivation, thus surface tension is modeled based on thermodynamic considerations rather than phenomenologically.

A Shan and Chen (SC) type model as described by Shan and Chen [1993, 1994] and Martys and Chen [1996] was used for the simulations in this research. Details specific to this work have been published in Schaap et al. [2007] and the following discussion will highlight some of the most important aspects of the publication. The general focus of the study by Schaap et al. [2007] was to determine appropriate LB parameters, obtain appropriate physical representation for the LB parameters and simulate $P_c - S$ curves. The SC type model is a multi-component model, meaning that there are two particle distributions at each lattice site. The effective fluid density, ρ, at a given lattice site is simply the sum of the two component densities at that site (i.e., $\rho = n_1 + n_2$). Interaction between the two fluids and the fluids and the solid phase are modeled through the fluid-fluid interaction potential, G_c, and the fluid-solid interaction potential, G_{a1} and G_{a2}, which are incorporated into the macroscopic velocities for each fluid component via adhesive and cohesive forces (see Chapter 5 and [Schaap et al., 2007]). It is noted that $G_{a1} = -G_{a2}$ where the positive and negative values imply nonwetting and wetting phase, respectively, thus in the remainder of this section G_a will be used for brevity.

One disadvantage to the LB method is that numerous simulations are required to obtain appropriate model parameters, namely ρ_i, σ_L, G_c and G_a where ρ_i is the initial density and σ_L is the lattice surface tension. In order to determine ρ_i, σ_L and G_c a series of 2D bubble simulations were conducted. The results of the simulations are presented in Figure 2.6, which indicates that at a $G_c\rho_i < 0.028$ no separation between the fluids is observed. Larger values of $G_c\rho_i$ increase the contrast between components and reduce the diffusion of one fluid into the other. The surface tension between each fluid was calculated using Laplace's law by first calculating the pressure inside and outside the bubble to obtain P_c and then measuring the radius, R, of each bubble. Figure 2.6 indicates a range of possible choices for ρ_i, G_c and σ_L. In practice, we found that a value of $G_c\rho_i$ greater than 0.06 led to numerical instabilities and somewhat arbitrarily we chose $G_c\rho_i = 0.0522$, resulting in $\rho_i = 2.087$ and $\sigma_L\rho_i = 0.085$.

In order to determine G_a, a series of 3D square duct simulations were conducted. In these simulations G_a was varied from 0 to 0.02 and the resulting contact angles are presented in Figure 2.7. It was assumed that the contact angle in the experimental systems, especially the

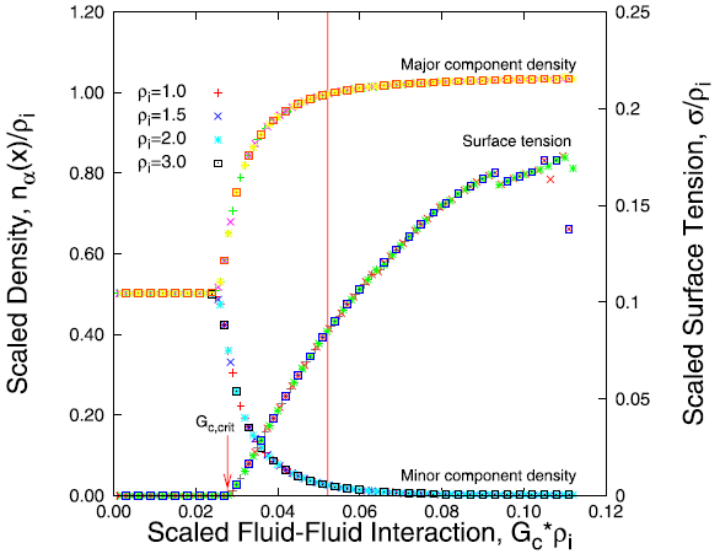

Figure 2.6: Scaled major and minor component densities in the bubble (left y-axis) and scaled lattice surface tension (right y-axis) as a function of the scaled cohesion parameter, $G_c\rho_i$. The vertical line depicts the $G_c\rho_i$ value used in the rest of the study. $G_{c,crit}$ depicts the critical $G_c\rho_i$ value above which stable fluid separation is possible

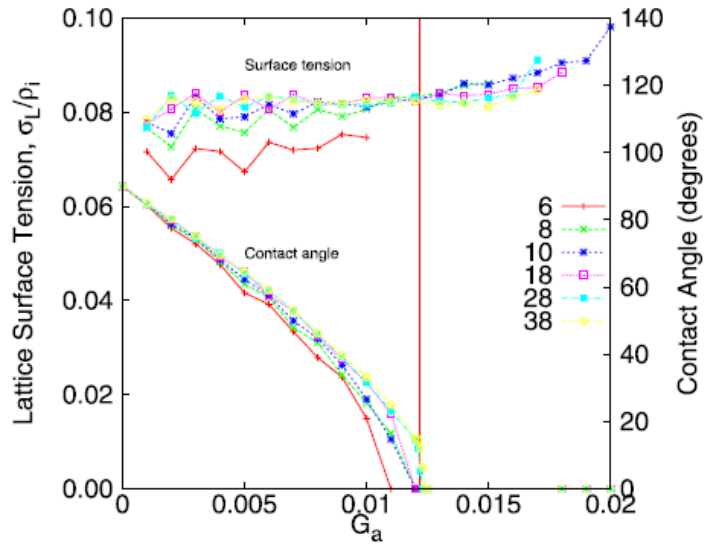

Figure 2.7: Surface tension and contact angle as a function of the value of the adhesion parameter, G_a, for several duct sizes.

air-water system, was zero, thus a G_a value corresponding to a zero contact angle was chosen for the simulations, which was 0.012. Since this publication it has been shown that G_a could be determined analytically and there is a discussion pertaining to this in Chapter 5. Figure 2.7 also shows surface tension as a function G_a indicating that the surface tension was slightly different in the duct simulations (0.083) than in the bubble simulations (0.085), most likely due to the presence of the solid phase.

Simulations of drainage and imbibition were conducted using the LB parameters determined above. The porous medium for the simulations consisted of segmented CMT images from the experimental system described in [Culligan et al., 2006]. A subset of 100 slices of the experimental data was used in order to decrease the computational demands. Dimensional analysis indicated that capillary forces dominated the system, while gravity, buoyancy and viscous forces were negligible. Based on this information the initial density, ρ_i, for each fluid was equal when $P_c = 0$ and the relaxation parameter, τ, that determines the viscosity was set to 1 for each fluid component. Furthermore, dimensional analysis results suggested that both the air-water and oil-water systems presented in Culligan et al. [2004, 2006] could be simulated with one set of simulations.

A comparison of the air-water and oil-water $P_c - S$ curves from Culligan et al. [2004, 2006] and LB $P_c - S$ curves are presented in Figure 2.8. In the top graph the LB simulations are compared to the air-water $P_c - S$ curves [Culligan et al., 2004], whereas in the bottom graph the LB simulations are compared to the oil-water $P_c - S$ curves [Culligan et al., 2006]. The simulated results in both graphs are identical simulations. The only difference between them is that they are scaled to physical units according to Laplace's law using the appropriate physical surface tension:

$$P_{c,p} = \frac{\sigma_p P_{c,L}}{h_p \sigma_L} \tag{2.16}$$

where h_p is the lattice resolution (17 μm) and the subscripts p and L represent physical and LB variables, respectively. Thus, in regards to the air-water $P_c - S$ curves the LB simulations are scaled to physical units by the surface tension between air and water ($\sigma_p = 0.0727\ N/m$) and for the oil-water $P_c - S$ curves the LB simulations are scaled to physical units by the interfacial tension between oil and water ($\sigma_p = 0.0378\ N/m$).

The air-water comparison shows excellent agreement between the observations and simulations. The simulated primary drainage curve is lower than the primary drainage curve from the experiments, however there is good agreement with subsequent drainage curves. Additionally, the simulated secondary drainage curve has a slightly lower nonwetting phase entry pressure than in the experiments. The simulated imbibition curve matches the observed imbibition curves and the simulations resulted in similar residual nonwetting phase saturation. These

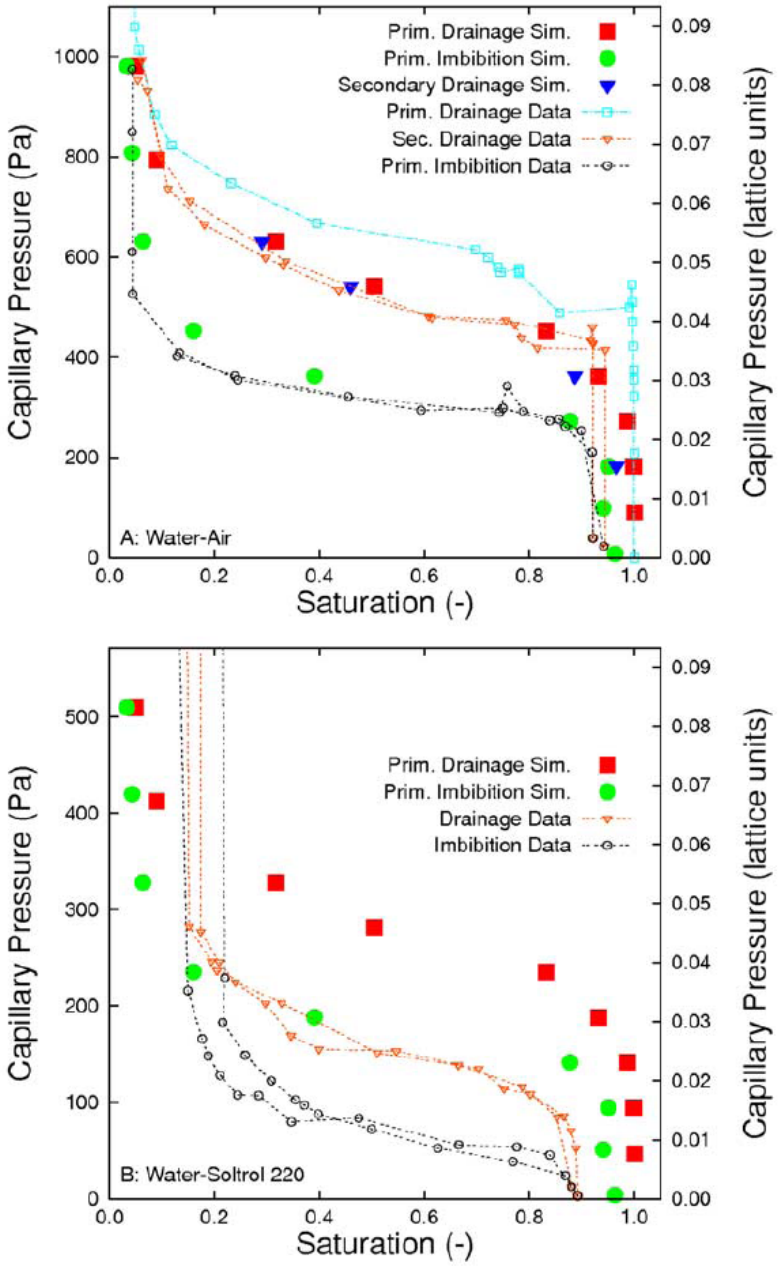

Figure 2.8: Simulated (large symbols) and measured (small symbols connected with lines) pressure saturation characteristics for the (A) water-air and (B) water-Soltrol systems. Data points for secondary drainage simulations were deleted from (B) for clarity.

results are especially encouraging since there was no optimization of parameters or calibration to the experimental data.

The comparison between the oil-water $P_c - S$ curves and the LB simulations show significant discrepancies. Culligan et al. [2006] reported issues with these measurements in that there was some space between the sintered glass beads and the column wall. This led to wall flow and likely caused a low entry pressure since the largest pore at the column wall was larger than the pores within the porous medium. Furthermore, that apparatus used in the oil-water experiments was a mixed wet system. Culligan et al. [2006] used glass beads as the porous medium and an acrylic column. The oil was found to preferentially wet the acrylic column, whereas water preferentially wet the glass beads, thus the mixed wet system. Since the oil preferentially wet the column this likely increased the wall flow observed in the experiments. Schaap et al. [2007] also pointed out that the discrepancies could be due to a nonzero contact angle for the oil-water-glass bead system. Again, the mixed wet system would affect the contact angle as well. Thus, it is possible that the oil-water system could be modeled by incorporating the correct contact angle into the simulations.

Schaap et al. [2007] showed that it was possible to choose appropriate LB parameters to simulate the air-water experimental results presented by Culligan et al. [2004, 2006]. Successful modeling of the air-water experimental system was somewhat unexpected since it has been reported that the SC type LB model used was not capable of simulating large density differences encountered in air-water systems [see Inamuro et al., 2004]. It is noted that large density differences were not explicitly simulated in Schaap et al. [2007], however since the experimental system was dominated by capillary forces there was agreement between the simulations and the air-water $P_c - S$ curves. Because it was thought that simulating the air-water experiments [Culligan et al., 2004] was out of reach, a decision was made early in this study to use the pore geometry of the oil-water experiments [Culligan et al., 2006]. The air-water results from Schaap et al. [2007] motivated the simulations presented in Chapter 5, in which the geometry of the air-water experiments [Culligan et al., 2004] was used to construct the lattice. Furthermore, the simulations presented in Chapter 5 included the entire imaged section rather than a subset (100 slices). The larger domain and the same pore geometry allowed for the comparison of $a_{nw} - S$ curves, as well as the $P_c - S$ curves.

Chapter 3. Validation of Image Analysis Methods for Computed Microtomography data of Multiphase Flow in Porous Systems

Mark L. Porter[1] and Dorthe Wildenschild[1]

1. Department of Chemical, Biological and Environmental Engineering, Oregon State University, 102 Gleeson Hall, Corvallis, OR 97331, USA

Computational Geosciences
233 Spring Street, New York, NY 10013
To be submitted

3.1 Abstract

This study focuses on the validation of an image processing technique that has been used to identify phases and estimate interfacial area between phases in gray-scale x-ray tomographic images. The original gray-scale images were smoothed with an anisotropic diffusion filter followed by a k-means cluster analysis to obtain segmented data from which porosity and saturation were estimated. Isosurfaces were constructed from the segmented data using a generalized marching cubes algorithm, and interfacial area was estimated from the resulting isosurfaces. The results for a 2-phase, high precision bead pack show that there was essentially no difference between porosity estimates and only minor differences between interfacial area estimates obtained from the segmentation method presented here and an indicator kriging segmentation method. Furthermore, porosity and interfacial area estimates obtained from both segmentation routines were in close agreement with values estimated from laboratory measurements. Interfacial area estimates for 3-phase capillary tube data using the method presented here was compared with other methods found in the literature including voxel counting, 2-point correlation functions, and the porous media marching cubes (PMMC) algorithm. All of these estimates were compared with an analytical estimate based on the assumption that the air-water interface in the capillary tube could be approximated by a spherical cap. The estimates obtained by various marching cubes methods tended to be similar and equally acceptable with errors ranging from approximately 1-20 %, whereas voxel counting and 2-point correlation functions overestimated the analytical interfacial area by 20-40 %. In addition, porosity and interfacial area estimates were obtained for CMT data with resolutions increased by factors of two and four, and the results showed little or no improvement in the comparison with laboratory estimates.

3.2 Introduction

In recent years, significant strides have been made in non-destructive imaging of materials and processes related to the Earth's subsurface. The advances in experimental techniques have made it possible to characterize and distinguish microscale characteristics such as pore geometry, pore network connectivity, fluid phase distributions in porous media, interfacial properties and solute transport. Computed microtomographic (CMT) imaging studies have been presented in: (1) petroleum engineering, focusing on the extraction of pore morphology and network information, and relative permeability estimates for use in pore network simulators [e.g., Coles et al., 1998; Lindquist and Venkatarangan, 1999; Patzek, 2000; Arns et al., 2003; Øren and Bakke, 2003; Turner et al., 2004; Prodonavić et al., 2006, 2007; Silin and Patzek, 2006]; (2) environmental engineering where the focus has been on describing non-aqueous phase liquid (NAPL) characteristics such as blob morphology [e.g., Al-Raoush and Wilson, 2005a,b; Schnaar

and Brusseau, 2005, 2006; Wildenschild et al., 2005] and fluid-fluid specific interfacial area [e.g., Culligan et al., 2004, 2006; Brusseau et al., 2006, 2007]; (3) geology and geochemistry [e.g., Song et al., 2001; Altman et al., 2005; Betson et al., 2005; Carlson, 2006; Fredrich et al., 2006; Ketcham and Iturrino, 2005]; (4) vadose zone and root zone processes [e.g., Hopmans et al., 1992; Clausnitzer and Hopmans, 1999, 2000; Wildenschild et al., 2005, 2002; Scheckel et al., 2007]; (5) and microbiology [e.g., Thieme et al., 2003].

Images obtained with CMT are gray-scale, and therefore need further processing before properties of interest can be quantified. The gray-scale voxels reflect the large spectrum of x-ray attenuation values of the scanned materials. Generally, segmentation (or classification) of gray-scale images results in a data set in which each separate entity, hereafter phase, in the image is represented by a single integer value. For example, in a porous material the solids and the void space may be represented by zeros and ones, respectively. Numerous segmentation routines have been presented in the literature [e.g., Pappas, 1992; Pal, 1996; Oh and Lindquist, 1999; Petitot, 2003; Sheppard et al., 2004] and Sezgin and Sankur [2004] provide a comprehensive survey of 40 segmentation methods. The segmented data is typically used to quantify properties such as phase distributions (i.e., porosity and saturation). However, the resulting estimates are known to vary significantly depending upon the original image quality and the segmentation method employed [Sezgin and Sankur, 2001]. Furthermore, CMT images of porous materials often contain features at or below the image resolution which blur the edges at phase boundaries, which can result in the loss of significant features and errors in the resulting macroscopic estimates [Sheppard et al., 2004].

Interfacial area estimates are typically obtained from the segmented data with some additional processing. The simplest estimate consists of counting the faces of voxels that exist between two phases, however, this approach results in interfacial area estimates with significant pixelation effects generally leading to an overestimation for the smooth fluid-fluid interfaces of interest. More advanced approaches include marching cubes methods [Dalla et al., 2002; McClure et al., 2007], 2-point correlation functions [Lindquist et al., 1996; Montemagno and Ma, 1999] and adaptive distance gradient filtering [Flin et al., 2005]. McClure et al. [2007] recently developed a porous media marching cubes (PMMC) algorithm, which extracts interfacial area estimates directly from gray-scale data, bypassing the need for a segmentation routine.

The primary objective of this study is (1) to present a detailed description of the image analysis methods employed in previous and current investigations (see [Wildenschild et al., 2005; Culligan et al., 2004, 2006; Porter et al., 2008a,b]), including recent improvements that affect the resulting estimates and (2) to validate these methods by comparing phase distribution and interfacial area estimates for a high precision glass bead pack and fluid configurations within capillary tubes with estimates obtained from some of the more commonly used image processing methods and software packages specifically designed for applications to porous media.

3.3 Image Analysis

3.3.1 Image Filtering

Image analysis begins with the reconstructed gray-scale images. Typically, the gray-scale images contain a certain level of noise that can greatly affect the quality of the subsequent segmentation. With this in mind, edge preserving noise reduction filters are commonly used and recommended as a first step in image analysis [Sheppard et al., 2004; Kaestner et al., 2008].

Culligan et al. [2004, 2006] employed a median filter to remove noise from the original gray-scale images. The median filter is a commonly used low-pass, edge preserving nonlinear digital filter that uses the median value of a specified convolution kernel to smooth the data [Gallagher and Wise, 1981] and performs well with outliers (i.e., random noise) [Kaestner et al., 2008]. Thus, it considers a neighborhood surrounding the voxel in consideration, and replaces that voxel with the median value of the neighborhood. A drawback to the median filter, and other filters based on convolution kernels, is that they blur sharp edged features present in the original image [Kaestner et al., 2008]. Thus, our improved image analysis algorithm uses an anisotropic diffusion filter to remove noise from the original gray-scale images[1]. The anisotropic diffusion filter is a mathematically formulated diffusion process that promotes intra-region smoothing over edge smoothing [Perona and Malik, 1990; Gerig et al., 1992]. The equation takes the following form [Gerig et al., 1992]:

$$\frac{\partial u(\boldsymbol{x},t)}{\partial t} = \nabla\cdot\left(c(\boldsymbol{x},t)\,\nabla u(\boldsymbol{x},t)\right) \tag{3.1}$$

where the vector $\boldsymbol{x}$ represents the spatial coordinates within the image, t represents the number of times (iterations) the filter is applied to the image, $u(\boldsymbol{x},t)$ is the voxel intensity and $c(\boldsymbol{x},t)$ is a diffusion function that controls the strength of diffusion based on intensity gradients. Perona and Malik [1990] and Gerig et al. [1992] proposed the following functions for $c(\boldsymbol{x},t)$:

$$c(\boldsymbol{x},t) = \exp\left(-\left(\frac{|\nabla u(\boldsymbol{x},t)|}{\kappa}\right)^2\right) \tag{3.2}$$

$$c(\boldsymbol{x},t) = \frac{1}{1+\left(\frac{|\nabla u(\boldsymbol{x},t)|}{\kappa}\right)^2} \tag{3.3}$$

where κ is a parameter chosen according to the level of noise and strength of edges contained in the image. In the discrete case, the anisotropic diffusion filter estimates local gradients as

[1] Daniel Simoes Lopes, http://www.civil.ist.utl.pt/~danlopes

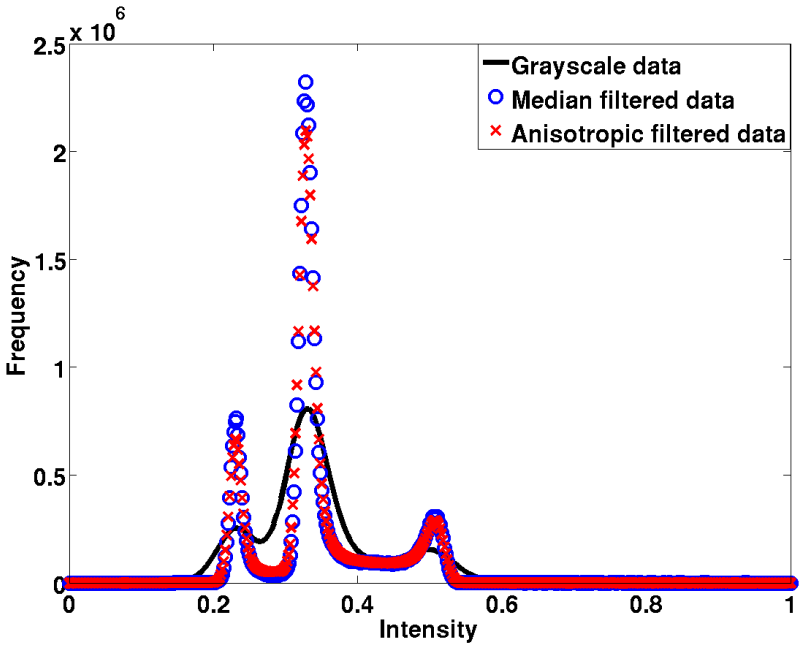

Figure 3.1: Comparison of the intensity histograms of the two filters to the original gray-scale data shows that the majority of the smoothing occurs in regions of similar intensities (i.e., there was a reduction of the variance of each peak). The left middle and right peaks represents the nonwetting, solid and wetting phases, respectively.

differences between neighboring voxels. If the gradient is large, a discontinuity is assumed and the diffusion process is stopped.

Figure 3.1 compares the histograms for each filter and an original gray-scale image. It is apparent that both filters reduce the variance in the intensity peaks, thus indicating that the majority of the filtering occurs within regions containing similar intensity values. Additionally, a comparison between the original gray-scale, median filtered and anisotropic diffusion filtered image is provided in Figure 3.2. This figure illustrates, qualitatively, that both filters remove a significant amount of noise and preserve edges relatively well. Furthermore, it appears that the anisotropic diffusion filter preserved small features better than the median filter. The graph of the intensity values for a cross section of the gray-scale median filtered and anisotropic filtered images appears in Figure 3.2. The intensity values for the gray-scale image show that the edges between the different phases were originally smooth, thus very little edge enhancement was achieved using the anisotropic diffusion filter. Multiple κ values were tested using Eq. 3.2 and 3.3 without achieving significant edge enhancement. Kaestner et al. [2008] proposed

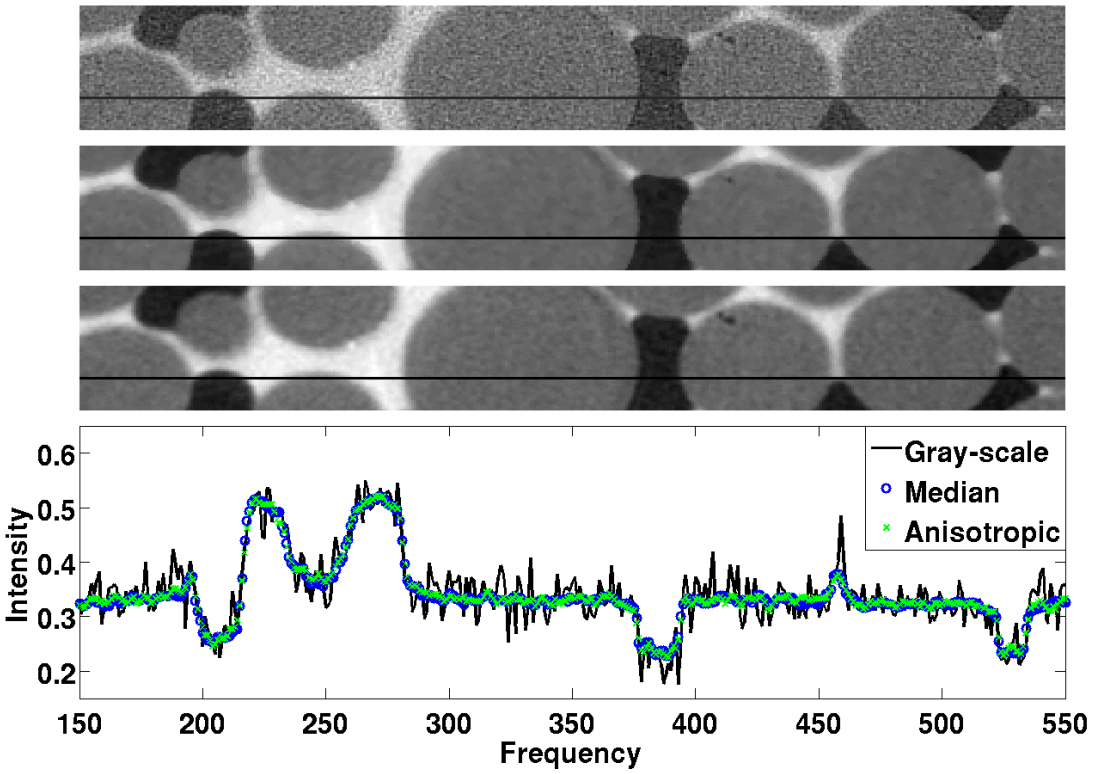

Figure 3.2: A comparison between the original gray-scale (top), median filtered (middle) and anisotropic diffusion filtered (bottom) images. The graph shows a cross section of the intensity values for each image (the horizontal line) indicating that there was very little difference between the median and anisotropic diffusion filter.

using a gradient image smoothed by a Gaussian filter for $c(\boldsymbol{x}, t)$ in Eq. 3.1, however this was not tested in this study. Applications of the anisotropic diffusion filter using equations 3.2 and 3.3 to CMT data collected at higher resolution at the Advanced Light Source (ALS) at Lawrence Berkeley National Laboratory (LBNL), showed that phase edges were preserved and enhanced with appropriate choices of κ. Thus, the quality of the original gray-scale image had a significant effect on enhancement of the phase boundaries, which again strongly influenced the outcome of the k-means cluster analysis, as will be discussed in the following section.

3.3.2 Segmentation

The choice of a segmentation algorithm depends on a number of factors and a variety of algorithms have been presented in the literature. Sezgin and Sankur [2004] and Kaestner et al. [2008] provide thorough discussions pertaining to a number of the segmentation algorithms available. In this study, and related works [Wildenschild et al., 2005; Culligan et al., 2004, 2006; Porter et al., 2008a,b], a k-means cluster analysis (included in the CCHIPS software package[2]) has been used to segment both two and three phase data. The k-means cluster analysis is an unsupervised learning algorithm that maximizes the difference between voxels in different clusters (between-group variation) and minimizes the differences between voxels within the same cluster (within-group variation). The algorithm requires an initial guess for the cluster centers, then iteratively updates the centers until an objective function, namely the squared error function, is optimized. K-means is appealing since it is relatively simple to implement, it converges quickly and it is capable of segmenting multiple phases. However, k-means also has some drawbacks: (1) there are no spatial constraints, (2) each cluster is characterized by a constant intensity and (3) obtaining the global optimum is not guaranteed [Pappas, 1992].

In practice, the CCHIPS k-means cluster analysis works well with 2-phase data, but does not properly segment 3-phase porous media data sets that do not contain sufficiently steep intensity gradients between the nonwetting and wetting interfaces obtained from GSECARS. In the 3-phase case, the CCHIPS routine produces segmented data with a thin film of solid phase assigned to all nonwetting-wetting interfaces indicating that a thin region of intermediate intensity voxels exist between the wetting (high intensity) and nonwetting (low intensity) phases. This likely occurs because the phase boundaries in the original gray-scale images from GSECARS were relatively smooth. To overcome this problem, Wildenschild et al. [2005] and Culligan et al. [2004, 2006] worked the k-means cluster analysis into a larger segmentation algorithm. The algorithm combined histogram specification, dilation and erosion operations, an edge detection routine (the Canny operator) and a medial axis routine along with the k-means cluster analysis, and most importantly, knowledge of the solid phase locations obtained from a 2-phase dry image. Although this algorithm worked well for the data presented in Wildenschild et al. [2005] and Culligan et al. [2004, 2006], applications to recent GSECARS CMT data resulted in the faulty creation of wetting phase regions around some of the solids, features that were not present in the gray-scale image. Additionally, this algorithm was rather complex and computationally intensive, taking approximately 3-4 hours for a typical data set (650x650x515 voxels) on a 1.8 GHz personal computer. Hereafter, this segmentation routine will be referred to as Autoseg.

[2]Copyright 2001, The Imaging Research Center, Children's Hospital Medical Center, Cincinnati, OH, http://www.irc.cchmc.org/cchips.php

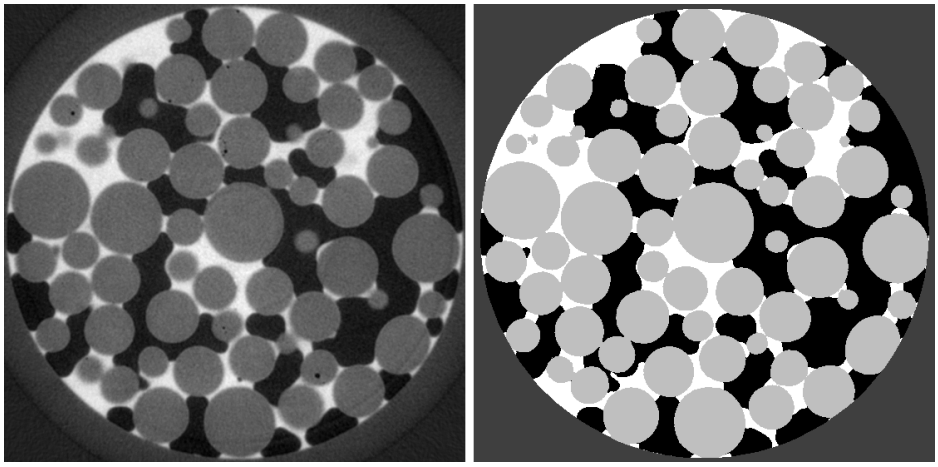

Figure 3.3: A comparison of filtered (anisotropic diffusion) gray-scale image (left) with k-means segmented image (right). The white, black and light gray regions are water, NAPL and solids, respectively.

The segmentation algorithm used in this study was much simpler, involving only a k-means cluster analysis and knowledge of the solid phase locations from a dry image. The first step in the algorithm consisted of segmenting both wet and dry data sets into binary images using the k-means cluster analysis. For the case of the wet data, the segmentation step created a binary image in which the nonwetting phase was separated from both the wetting and solid phases. The solid and wetting phase was subsequently separated by overlaying the solid phase, obtained from the segmented dry data, onto the segmented (binary) wet data. A post processing step was implemented to remove blobs under a certain size. This was especially useful for removing small artifacts within the beads and small unphysical fluid blobs that were created due to inaccuracies in the segmentation routine and slight movement of the solid phase during the experiments. Figure 3.3 shows an example of the resulting segmented data from this routine. Qualitatively, it appears that the segmented data represents the original data well. Additionally, this algorithm segments a typical data set in approximately 10 minutes.

In recent applications of the k-means cluster analysis to 3-phase data collected at the ALS, the algorithm properly segmented the data without the need of overlaying the solid data onto the wet data. This is the simplest and most accurate segmentation routine, of the three discussed here, since it reduces any error associated with movement of the solid phase. The success of the algorithm when applied to the ALS data set is most likely due to the fact that the phase edges in the original gray-scale images were sharper than those obtained from GSECARS mainly because of a better signal-to-noise ratio during data collection. This led to edge enhancement

during the filtering step (see Section 3.3.1) and, thus the k-means algorithm easily identified the nonwetting-wetting phase interface.

Porosity and saturation values were estimated from the segmented data via voxel counting. This is the simplest and most widely used method for these types of estimates. Two-point correlation functions may also be used for these estimates, however, Lindquist et al. [1996] showed that there was little difference in the estimates obtained with either method.

3.3.3 Interfacial Area

Compared to the number of segmentation methods, relatively few algorithms have been presented in the literature for estimating interfacial area from CMT image data. Some of these include voxel counting, marching cubes (MC), 2-point correlation functions and adaptive distance gradient filtering (ADGF). Counting voxel faces common to the two phases of interest is by far the simplest method, however, in cases pertaining to fluid-fluid interfaces in porous media where the surfaces are smooth, the estimates are high. Lindquist et al. [1996] states that voxel counting estimates should be considered as upper bounds for interfacial area.

MC algorithms have recently been employed in a number of porous media studies [Montemagno and Ma, 1999; Dalla et al., 2002; Culligan et al., 2004, 2006; McClure et al., 2007] and one advantage of this method is that it can be applied directly to the gray-scale data [McClure et al., 2007]. The MC algorithm produces an isosurface constructed from a triangular-mesh based on information from the surrounding voxels, thus reducing pixelation effects. Dalla et al. [2002] used synthetic binary data to investigate the accuracy of the marching cubes algorithm for wetting phase bridges encountered in porous media, and showed that the estimated area was generally smaller than the analytical estimate.

Other methods for estimating interfacial area from CMT image data include 2-point correlation functions and ADGF. Lindquist et al. [1996] and Song et al. [2001] compared interfacial area estimates obtained from 2-point correlation functions and voxel counting. Their results showed that voxel counting resulted in estimates that were 1.5-2.9 times higher than estimates obtained from 2-point correlation functions. Montemagno and Ma [1999] compared 2-point correlation functions and marching cubes interfacial area estimates for binary data of synthetic sphere packings and single spheres, and showed that the 2-point correlation functions obtained smaller relative errors than MC and that MC is sensitive to pixelation effects. Flin et al. [2005] compared their ADGF algorithm to the MC applied to binary and smoothed binary data, and for surface area estimates of three snow samples, they observed relatively similar results from all methods, except for MC applied to Gaussian smoothed binary data, which they claim was a result of the large kernel (11x11x11) used in the Gaussian filter.

Interfacial area estimates presented here, and in related works [see Culligan et al., 2004, 2006; Porter et al., 2008a,b], were obtained using the commercially available image analysis software, Amira^{TM}, which uses a generalized marching cubes algorithm to generate an isosurface between phases. The isosurfaces are generated by choosing a single isovalue that effectively separates one phase from all other phases in the image. Isosurfaces are generated for the total interfacial area for the solid phase, a_s, wetting phase, a_w, and nonwetting phase a_n. In a 3-phase system the total interfacial area for each phase is defined as follows:

$$\begin{aligned} a_s &= a_{ws} + a_{ns} \\ a_w &= a_{nw} + a_{ws} \\ a_n &= a_{nw} + a_{ns} \end{aligned} \tag{3.4}$$

where a_{nw} is the interfacial area of the nonwetting-wetting interface, a_{ns} is the interfacial area of the nonwetting-solid interface, and a_{ws} is the interfacial area of the wetting-solid interface. From Eq. 3.4 it can be shown that the interfacial area between two phases is defined as follows:

$$\begin{aligned} a_{nw} &= \frac{1}{2}\left(a_w + a_n - a_s\right) \\ a_{ns} &= \frac{1}{2}\left(a_n + a_s - a_w\right) \\ a_{ws} &= \frac{1}{2}\left(a_w + a_s - a_n\right). \end{aligned} \tag{3.5}$$

In many studies pertaining to interfacial area in porous media, a_{nw} is of interest [Cheng et al., 2004; Culligan et al., 2004, 2006; Chen et al., 2007; Brusseau et al., 2006] and the use of equation 3.5 is common. It should be noted that Eq. 3.5 will propagate any error associated with the estimates of a_w, a_n and a_s when these are the measured values. This is especially important when using the marching cubes algorithm to estimate a_w, a_n and a_s, since it is often difficult to obtain perfect contact between the three isosurfaces. For example, consider a trinary data set in which the nonwetting, solid and wetting phases are assigned the values 0, 1 and 2, respectively; one would need multiple isovalues and a second binary data set for one of the phases to construct satisfactory isosurfaces of a_w, a_n and a_s. Culligan et al. [2004, 2006] used a method that involved a trinary data set for estimating a_n and a_w and a separate binary data set for a_s. In their case the trinary values were 3, 5 and 10 for the nonwetting, solid and wetting phases, respectively. The isovalues selected were 4 and 7.5 for a_n and a_w, respectively. For the binary data set, the values for the nonwetting phase and solid phase were 3 and 5, respectively, and an isovalue of 4 was selected. Additionally, the data was resampled in Amira^{TM} prior to applying MC. The resampling step smoothed the data and coarsened the grid using a triangle

window. The grid coarsening was necessary at the time because of computational memory constraints (2 GB). Although, it was determined that this method resulted in good surface area estimates for a binary sphere [Culligan et al., 2006], a number of issues arise with this method when applied to 3-phase porous media data. The first issue involves the use of a single isovalue in a trinary data set to estimate a_w or a_n. Using an isovalue of 4 for a_n resulted in an isosurface that was biased toward the nonwetting phase at all nonwetting-wetting interfaces. In a similar fashion the use of an isovalue equal to 7.5 for a_w resulted in an isosurface biased toward the wetting phase at all nonwetting-wetting interfaces. This ultimately resulted in isosurfaces that had little or no contact at all nonwetting-wetting interfaces, thus introducing some error in approximations based on Eq. 3.5.

In our improved interfacial area estimate method the segmented trinary data was converted to three (one for each phase) different binary data sets in which each phase was separated from the other two phase. For example, in the nonwetting data set the nonwetting phase was set equal to zero and both the wetting and solid phases were set equal to one. This allowed for the use of a single isovalue, set equal to 0.5, for the construction of all isosurfaces, which ensures maximal contact. This is similar to the approach Dalla et al. [2002] applied to synthetic binary data. Additionally, we smooth the binary data with a Gaussian filter (3x3x3 kernel) to reduce pixelation effects in the resulting isosurfaces.

McClure et al. [2007] recently proposed a mathematically rigorous porous media marching cubes (PMMC) algorithm that addresses many of the issues that arise when applying the marching cubes algorithm to segmented data. Additionally, this algorithm estimates other properties including interfacial curvature and 3-phase contact lines, however, only a few key aspects pertaining to interfacial area estimates are discussed here, for further details see [McClure et al., 2007]. PMMC uses the standard generalized marching cubes algorithm for the fluid and solid phases except when a nonwetting-wetting-solid contact line is encountered. It is precisely in these locations that Dalla et al. [2002] observed that the standard marching cubes algorithm did not faithfully represent the wetting phase surface. In these cases, PMMC employs a combination of the marching cubes, interpolation and extrapolation to accurately construct the isosurface. Furthermore, PMMC estimates the interface of interest (i.e., a_{nw}, a_{ws}, a_n, etc...) directly, bypassing the need for Eq. 3.5. Since PMMC can directly estimate the interface of interest it is possible to use the original gray-scale data, thus avoiding the segmentation step. It is noted that the interfacial area estimates are affected by the original noise in the data and McClure et al. [2007] recommends the use of a smoothing filter.

3.4 Validation Data

3.4.1 Experimental Data Sets

The experimental data presented here was collected at the GeoSoilEnviro Consortium for Advanced Radiation Sources (GSECARS) beam-line at the Advanced Photon source (APS), Argonne National Laboratory. Only the most necessary details pertaining to the GSECARS beam-line specifications will be presented here, further details can be found in Wildenschild et al. [2002, 2005]. The experiments were conducted at an energy level just above the K-shell photoelectric absorption edge of iodine (33.2 keV). An 11% (by weight) iodine-spiked water solution was used as the wetting phase in these experiments to facilitate absorption in the wetting phase, resulting in an intensity distribution from which the nonwetting and wetting phases could be distinguished. A tunable monochromator isolates a single energy, 33.27 keV, from the white synchrotron light and the x-rays are subsequently converted to visible light by a scintillator and captured on a high speed CCD camera. The raw data is processed with a series of algorithms developed in IDL^{TM} (Research Systems Inc.) that sharpen edges, remove ring artifacts, center the data and then reconstruct the gray-scale images via a filtered back-projection algorithm [Rivers, 2001].

The experimental data consisted of CMT images of (1) a high precision bead pack and (2) cylindrical capillary tubes of three different radii, each containing an air-water interface. The high precision beads ($d = 0.8\,mm \pm 0.01\,mm$, $\rho = 2.5\,g \cdot cm^{-3}$) were packed into an acrylic column ($i.d. = 6.54\,mm$). The mass of the beads packed in the column was $233.0\,mg \pm 0.5\,mg$. Based on this information the number of beads in the column and the surface area for the entire bead pack was estimated to be 348 ± 8 beads and $700\,mm^2 \pm 20\,mm^2$, respectively. The bead pack was imaged at two different resolutions, namely $11.8\,\mu m$ and $5.9\,\mu m$. The two different resolutions were obtained by adjusting the region of interest (ROI) using a binning procedure. The higher resolution (5.9 μm) data was imaged with a Micromax CCD camera equipped with a Nikon macro lens and a 10 mm spacer, and the full camera chip (1300x1050 voxels) was used. The lower resolution (11.8 μm) data was obtained by binning the voxels 2 by 2 such that a ROI 650x515 voxels was produced.

Cylindrical capillary tubes with three different radii were used to image the air-water meniscus near equilibrium conditions. The capillary tube dimensions and CMT image resolutions are listed in Table 3.1. The tubes were secured in a vertical position and the lower end was submerged in a water reservoir while imaging. Cylindrical capillary tubes were chosen so that interfacial area estimates could be compared with interfacial area calculations based on the

Table 3.1: List of capillary tube inside diameters and the associated CMT image resolutions.

Inside Diameter (μm)	CMT Image Resolution (μm)
800 ± 8	13, 6.5
1350 ± 25.4	13
1500 ± 15	13, 6.5, 3.3, 1.6

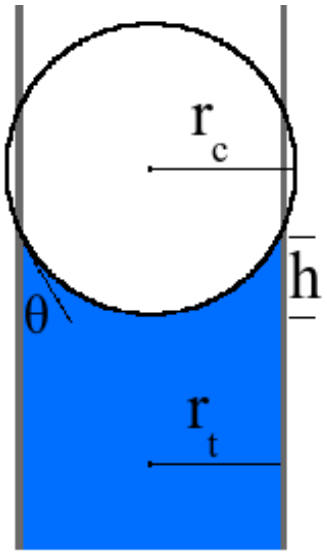

Figure 3.4: Illustration of the air-water meniscus in a capillary tube where r is the radius of the sphere, θ is the contact angle and h is the height of the spherical cap used to calculate an analytical interfacial area of the meniscus.

radius of curvature from Laplace's Law:

$$P_c = P_n - P_w = \frac{2\sigma \cos\theta}{r_t} \tag{3.6}$$

where σ is the surface tension between air and water, θ is the contact angle and r_t is the radius of the capillary tube. We assumed that the shape of the meniscus could be approximated by a spherical cap, thus $a_{nw} = 2\pi r_c h$, where r_c is the radius of curvature and h is the height of the cap, see Figure 3.4. The radius for the tube and the radius of curvature of the meniscus are related by $r_t = r_c \cos\theta$.

3.4.2 Methods

The majority of CMT data reported in the literature is subjected to image analysis techniques similar to those discussed in Section 3.3 prior to the estimation of porosity, saturation and interfacial area, thus it is important to note that the potential for error is relatively high. However, there is no straightforward way to assess the error associated with the estimates since they are affected by (1) the noise in the original image, (2) smoothing of edges when filtering the noise, (3) improper segmentation of some voxels near phase boundaries, (4) the sensitivity of MC to pixelation effects and (5) the possibility of poor contact between isosurfaces.

In order to assess the reliability and validate the image analysis method presented here and used in recent investigations [Porter et al., 2008a,b] we have calculated porosity and interfacial area estimates for the experimental systems described in Section 3.4.1. First we estimated the porosity of the 2-phase high precision beads using our k-means segmentation routine and indicator kriging, and compared the results with estimates based on laboratory measurements. Indicator kriging was conducted using 3DMA[3] and is described in full detail by Oh and Lindquist [1999]. Briefly, indicator kriging is a local thresholding method that incorporates spatial information through the spatial 2-point covariance of the image [Oh and Lindquist, 1999]. The method requires a population assignment step, which segments a fraction of the image based on two threshold values T_0 and T_1. Care must be taken in the choice of T_0 and T_1 since misclassification can occur. Oh and Lindquist [1999] developed automated methods for selecting T_0 and T_1, however, based on their experience they recommend user selection [Lindquist, 1999]. Indicator kriging was chosen to compare with k-means cluster analysis because it accounts for spatial correlations within the image, whereas k-means does not. Furthermore, 3DMA is a software package specifically designed for applications in porous media, and therefore allows for comparison of our approach to another commonly used algorithm.

Numerous interfacial area estimates for the high precision glass beads and menisci in the capillary tubes were calculated using various combinations of the image analysis techniques discussed in Section 3.3 and are described in detail here. Table 3.2 lists the various interfacial area methods and the image analysis techniques used to obtain each estimate. The first column lists the names we have used to identify the different interfacial area estimates. The 2-Point Correlation estimates were obtained using the method described by Torquato [2002, pg. 290] and the algorithm was implemented as described in [Schaap and Lebron, 2001]. The method entitled Gauss MC is the method we have used in recent studies [see Porter and Wildenschild, 2008; Porter et al., 2008a] and is a replacement for the Culligan Method, which was used in [Culligan et al., 2004, 2006]. Blob3D[4] refers to estimates obtained using the freely available

[3] http://www.ams.sunysb.edu/~lindquis/3dma/3dma_rock/3dma_rock.html
[4] http://www.ctlab.geo.utexas.edu/software/index.php

Table 3.2: List of the different interfacial area estimates presented in this study and the corresponding image analysis steps.

Method	Filter	Segmentation	Data Type
Voxel Counting	Aniso. Diff. (x1)	k-means & Ind. Krig.	binary
2-Point Corr.	Aniso. Diff. (x1)	k-means & Ind. Krig.	binary
Binary MC	Aniso. Diff. (x1)	k-means & Ind. Krig.	binary
Median MC	Aniso. Diff. (x1)	k-means & Ind. Krig.	Median filtered binary
Gauss MC	Aniso. Diff. (x1)	k-means & Ind. Krig.	Gauss filtered binary
Resample MC	Aniso. Diff. (x1)	k-means & Ind. Krig.	Resampled trinary
Blob3D	Aniso. Diff. (x1)	k-means & Ind. Krig.	binary
PMMC	Median (x2)	–	gray-scale
Culligan Method	Median (x1)	Autoseg	Resampled trinary

image analysis software package. Blob3D uses a MC algorithm to construct isosurfaces from which interfacial area estimates are obtained. In practice we found that Blob3D creates surfaces on the flat edges of the capillary tube data, thus we were not able to obtain reliable interfacial area estimates from Blob3D for the capillary tube data. This artifact was not an issue with the high precision beads since the beads were not in contact with the edges of the volume. The "Filter" column lists the filter used to remove noise from the original gray-scale data and, in parentheses, indicates the number of times (or iterations) the filter was applied to the data. The "Segmentation" column indicates which segmentation method was used to classify the phases. For the high precision glass beads both k-means and indicator kriging segmentation routines were used in order to investigate the sensitivity of the resulting interfacial area estimate on the segmentation routine. In the case of PMMC no segmentation routine was required. The last column, entitled "Data Type," indicates the type of data from which the estimate was obtained. In most cases binary data from the indicated segmentation routine was used to obtain interfacial area estimates. In the Median MC and Gauss MC, the respective filter kernels were 3x3x3 so that the edges of each phase were the only areas affected by the filter. The median filter was chosen since (in a binary image) it does not smooth the data, it only rearranges the binary values near edges based on the surrounding neighbors. This effectively tests the sensitivity of interfacial area estimates to the segmentation routine. The Gaussian filter, on the other hand, smoothed the binary data. A smoothing filter was chosen since it has been shown that the marching cubes algorithm is sensitive to pixelation effects [Montemagno and Ma, 1999; Dalla et al., 2002; McClure et al., 2007], although to a lesser extent than voxel counting. In both the Median and Gauss MC an isovalue of 0.5 was selected and good contact between each isosurface

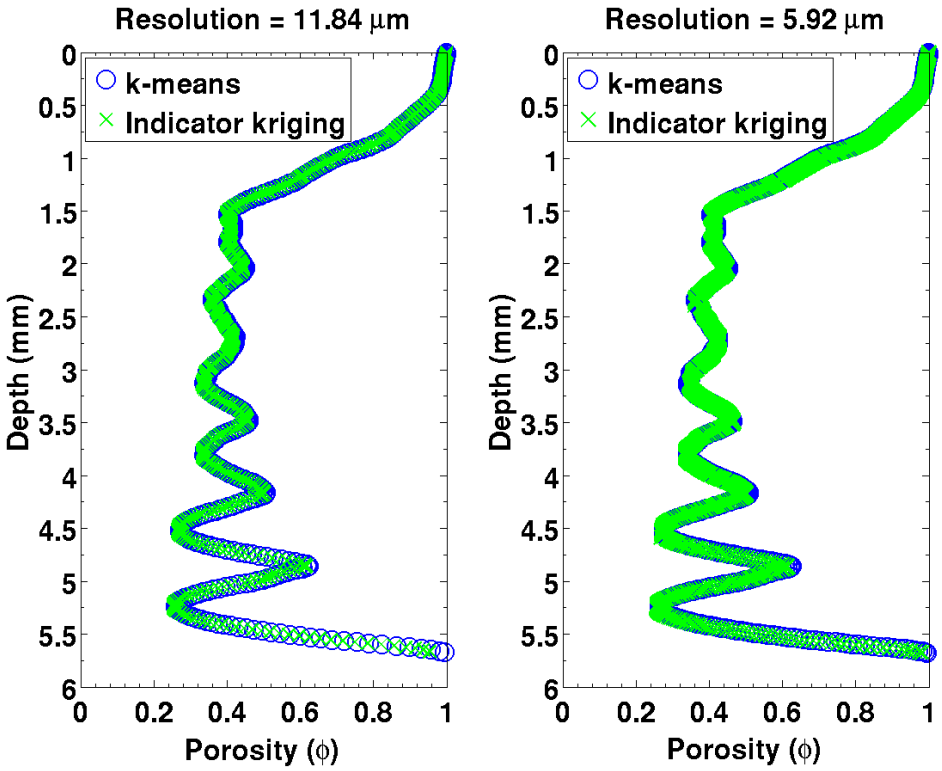

Figure 3.5: A comparison of porosity estimates as a function depth for k-means and indicator kriging for the low (left) and high (right) resolution beads. The comparison indicates that there are no significant differences in average porosity (per slice) between the two methods. In addition, the resolution does not have a significant effect on the estimated porosities.

was maintained. In the case of Gauss MC the smoothing caused some deterioration of contact near the three phase contact line.

3.5 Results

3.5.1 High Precision Beads (2-Phase Analysis)

Figure 3.5 compares the porosity profiles obtained from the k-means and indicator kriging segmentation methods for the two resolutions. These results indicate that the two segmentation methods produce virtually the same porosity estimates and that doubling the resolution had little effect on the estimates. Table 3.3 compares the volume averaged porosity estimates

Table 3.3: Comparison of volume averaged porosity estimates obtained from measurements and segmentation data.

Resolution (μm)	Measured	K-means	Indicator kriging
11.84	0.509	0.515 (1.2 % error)	0.510 (0.3 % error)
5.92	0.509	0.517 (1.5 % error)	0.515 (1.1 % error)

obtained from laboratory measurements with estimates obtained from the segmented data. These values are reported to three significant figures for comparison purposes only. These results show that all of the estimates were essentially the same with a maximum of 1.5 % error, and that the estimates were not notably sensitive to either of the segmentation routines nor the different resolutions.

The surface area of the 2-phase bead pack was estimated using voxel counting, 2-point correlation functions, Binary MC, Median MC, Gauss MC, Resample MC and Blob3D (see Table 3.2) at the 11.8 and 5.9 $\mu m/voxel$ resolutions. The relative errors (with respect to the laboratory measurement) for all estimates are presented in Figures 3.6 and 3.7. The two horizontal lines represent the error associated with the laboratory measurement. Voxel counting and 2-point correlation functions overestimated the interfacial area by 25 % or more. All other estimates were within 15 % and 10 % of the laboratory measurement for the 11.8 and 5.9 $\mu m/voxel$ resolutions, respectively. It is interesting to note that for both resolutions, the errors for voxel counting approach 40 %, which is expected when assuming the pixelation effects lead to an overestimation corresponding to the $\sqrt{2}$. The Blob3D interfacial area estimates are based on isosurfaces, thus it is not surprising that they are similar to the other MC methods. The error associated with the 2-point correlation functions contradicts the results reported by Montemagno and Ma [1999], however they calculated a_s using the angular average, which appears to be a more accurate method than the one we used here [see Torquato, 2002, pg. 290]. Figures 3.6 and 3.7 also show that the estimates were not significantly affected by the segmentation routine; at both resolutions estimates for the indicator kriging data were slightly lower than the estimates obtained by k-means cluster analysis. In all cases, the interfacial area estimates increased slightly, between a factor of 1.04-1.09, as a result of doubling the resolution. Most of the MC methods underestimated the laboratory measurement at 11.8 $\mu m/voxel$, whereas at 5.9 $\mu m/voxel$ the interfacial area estimates increased slightly and therefore match the measurements more closely.

Doubling the resolution was a relatively easy process at GSECARS, however the decision to do so should not be made lightly since the size of the data increased by a factor of 8. This is especially important if multiple data sets are collected throughout an experiment. The number

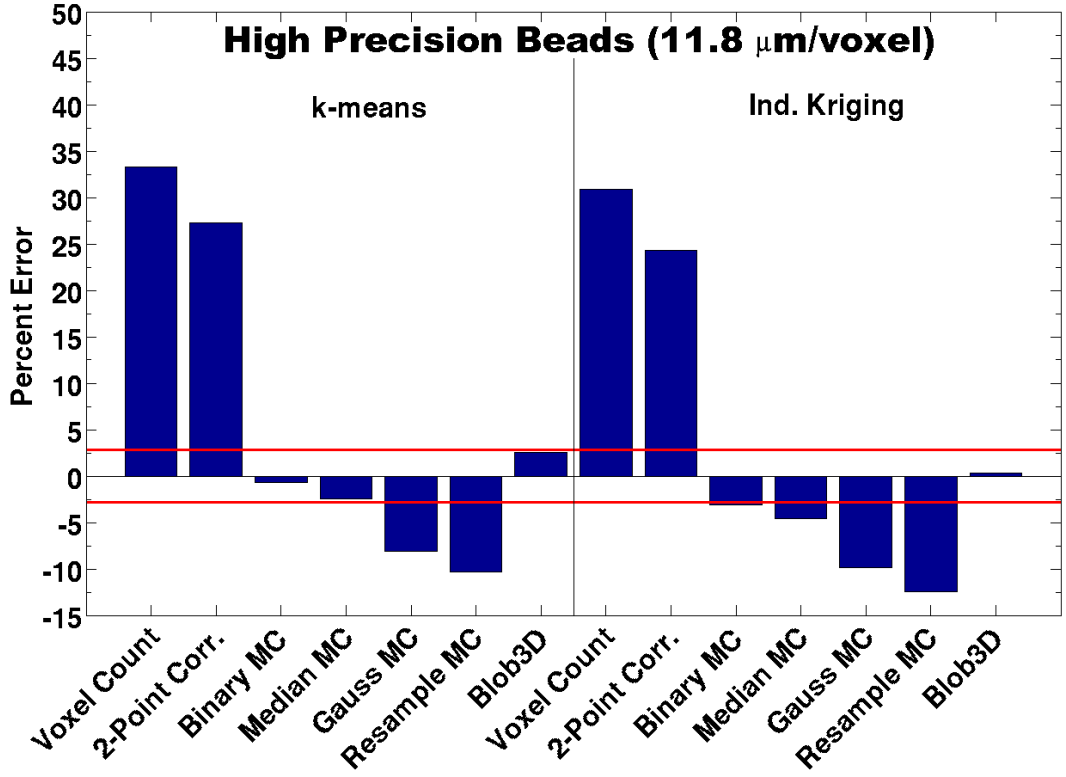

Figure 3.6: The relative error obtained from various interfacial area estimation methods for the 2-phase, high precision glass beads at a resolution of 11.8 $\mu m/voxel$. The figure shows result for k-means and indicator kriging on the left and right, respectively, of the vertical line. The horizontal red lines represents the error associated with the laboratory measurement, which is the basis for the relative error.

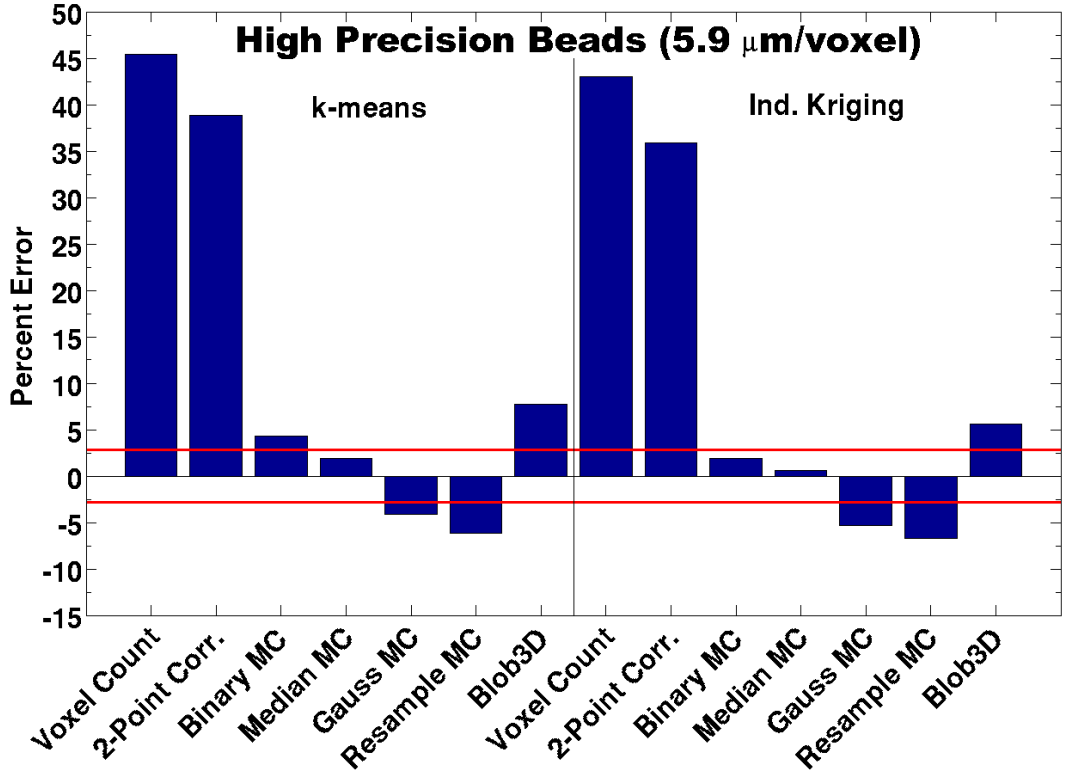

Figure 3.7: The relative error obtained from various interfacial area estimation methods for the 2-phase, high precision glass beads at a resolution of 5.9 $\mu m/voxel$. The figure shows result for k-means and indicator kriging on the left and right, respectively, of the vertical line. The horizontal red lines represents the error associated with the laboratory measurement, which is the basis for the relative error.

of voxels in the 11.8 and 5.9 $\mu m/voxel$ resolution data sets were 650x650x515 (415 MB) and 1300x1300x1030 (3.3 GB), respectively. Thus, the computational demands to store and process the higher resolution data increased significantly. The performance of all software used in this study greatly decreased when working with the high resolution data. Considering the differences in the estimates presented here, the increased costs exceed the improvements gained.

Although the porosity and interfacial area estimates presented in this study were not highly sensitive to the segmentation routines used, it is possible that other properties of the porous media (i.e., pore connectivity, permeability, etc...) could be affected by the choice of the segmentation routine and the resolution of the data. This particularly needs to be considered when the regions near bead-to-bead contacts are of importance. Both segmentation routines produced binary data in which many of the beads touched (See Figure 3.3), however no tests were conducted to investigate how this affects other properties or processes within the porous medium.

3.5.2 Capillary Tubes (3-Phase Analysis)

Capillary tube CMT data was collected to test the image analysis methods on a simple 3-phase system. The 13 μm resolution data was used to compare a_{nw} estimates obtained by voxel counting, 2-point correlation functions, Resample MC, Binary MC, Median MC, Gauss MC, PMMC and the Culligan Method (see Table 3.2). The values reported for PMMC were provided by the author of [McClure et al., 2007]. Voxel counting a_{nw} estimates did not require the use of Eq. 3.5 since the voxel faces between the phases of interest were counted. 2-point correlation estimates of a_n, a_s and a_w were obtained as described by Torquato [2002, pg. 290] and a_{nw} values were calculated using Eq. 3.5. All other estimates were obtained from Amira^{TM}and Eq. 3.5 as described in Section 3.3.3. Estimates from Blob3D were not included here since estimates for a_s, a_n and a_w obtained with this program included regions associated with the edges of the volume. This was not an issue with the 2-phase bead data since none of the solid phase touched the edges. The extra area associated with the edges of the volume could be subtracted out since those areas are flat surfaces, however, since Blob3D uses isosurfaces to estimate interfacial area, it is expected that the results would be similar to those obtained from Amira^{TM}.

The resulting isosurfaces for a_n and a_w produced using Amira^{TM}are provided in Figure 3.8. As expected, Binary and Median MC show significant pixelation effects (stair-step appearance). and Binary MC was more representative of the wetting phase at the three phase contact line than the Median MC. Gauss MC shows slight signs of pixelation effects, yet was relatively smooth at the three phase contact line. Resample MC resulted in the smoothest isosurfaces, however, there was no contact at the nonwetting-wetting interface.

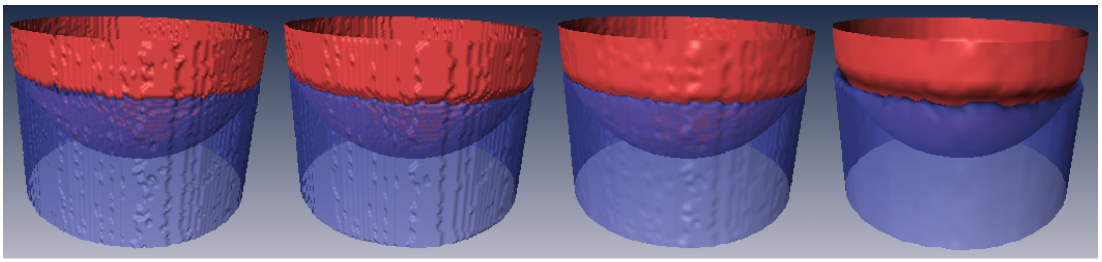

Figure 3.8: Comparison of (a) Binary MC, (b) Median MC, (c) Gauss MC and (d) Resample MC nonwetting (red) and wetting (blue) phase isosurfaces.

Table 3.4: Comparison of a_{nw} estimates for the $13\mu m$ resolution capillary tubes. All estimates area in units of mm^2.

	Tube $I.D.$ (μm)		
	800	1350	1500
Analytical Estimate	0.91	2.08	3.36
Voxel Counting	1.23	2.90	4.37
2-Point Corr.	–	2.57	4.18
Binary MC	0.85	1.99	3.33
Median MC	0.80	1.94	3.15
Gauss MC	0.76	1.84	2.98
Resample	0.76	1.82	2.71
PMMC	0.78	1.93	2.95
Culligan Method	0.96	2.30	2.77

Table 3.5: Measured and calculated values for predicting the interfacial area of the meniscus in the capillary tubes assuming the meniscus was the shape of a spherical cap (i.e., $a_{nw} = 2\pi r_c h$)

Tube *I.D.* (μm)	**Measured** r_c (mm)	**Measured** h (mm)	**Measured** θ ($^\circ$)	**Calculated** r_c (mm)	**Calculated** h (mm)
800	0.40	0.36	6	0.40	0.36
1350	0.73	0.44	22	0.73	0.46
1500	0.76	0.66	3	0.75	0.71

In order to compare a_{nw} estimates presented in Table 3.4 with a_{nw} estimates based on an analytical model, it was assumed that the shape of the meniscus was a spherical cap, as illustrated in Figure 3.4, and the interfacial area is given by $2\pi r_c h$. Values for r_c and h were obtained independently by two different methods to ensure the resulting estimates were reliable. In the first method, r_c and h were measured directly from cross sections (on the principle x- and y-axes) of the gray-scale images. In the second, method the contact angle between the meniscus and the capillary tube was estimated along the principle x- and y-axes of gray-scale images, and values for r_c and h were then calculated based on θ and the radius of the tubes, r_t, using $r_t = r_c \cos\theta$ and $r_c = (h^2 + r_t^2)/2h$. The values obtained from the measurements and calculations appear in Table 3.5, which shows that there was little difference between the measured and calculated values for r_c. However, there were noticeable differences between the measured and calculated h values. Based on these observations, the calculated values of r_c and h (columns 5 and 6, respectively) in Table 3.5 were used to calculate analytical estimates of a_{nw} for the nonwetting-wetting phase meniscus.

The percent errors associated with the analytical a_{nw} estimate and the image analysis estimates for the three capillary tubes at a voxel resolution of 13 μm are shown in Figure 3.9. The horizontal lines represent the error associated with the analytical estimates. All MC methods underestimated the analytical estimate by 1-20 % error, whereas voxel counting and 2-point correlation functions overestimated the analytical value by 20-40 %. Of all MC methods, Resample MC method consistently resulted in the greatest percent error, whereas the Binary MC method consistently resulted in the least percent error. This suggests that in the binary MC method, pixelation effects make up for areas in which the MC method does not accurately capture the geometry of the phase boundary. Estimates obtained from the Culligan Method were the only estimates that were not consistent for all three capillary tubes. Although all estimates from the Culligan method were within 20 % error, this method slightly overestimated the analytical estimate for the 800 and 1350 μm tubes, but underestimated it for the 1500 μm tube. Since the only difference between Resample MC and the Culligan Method was the

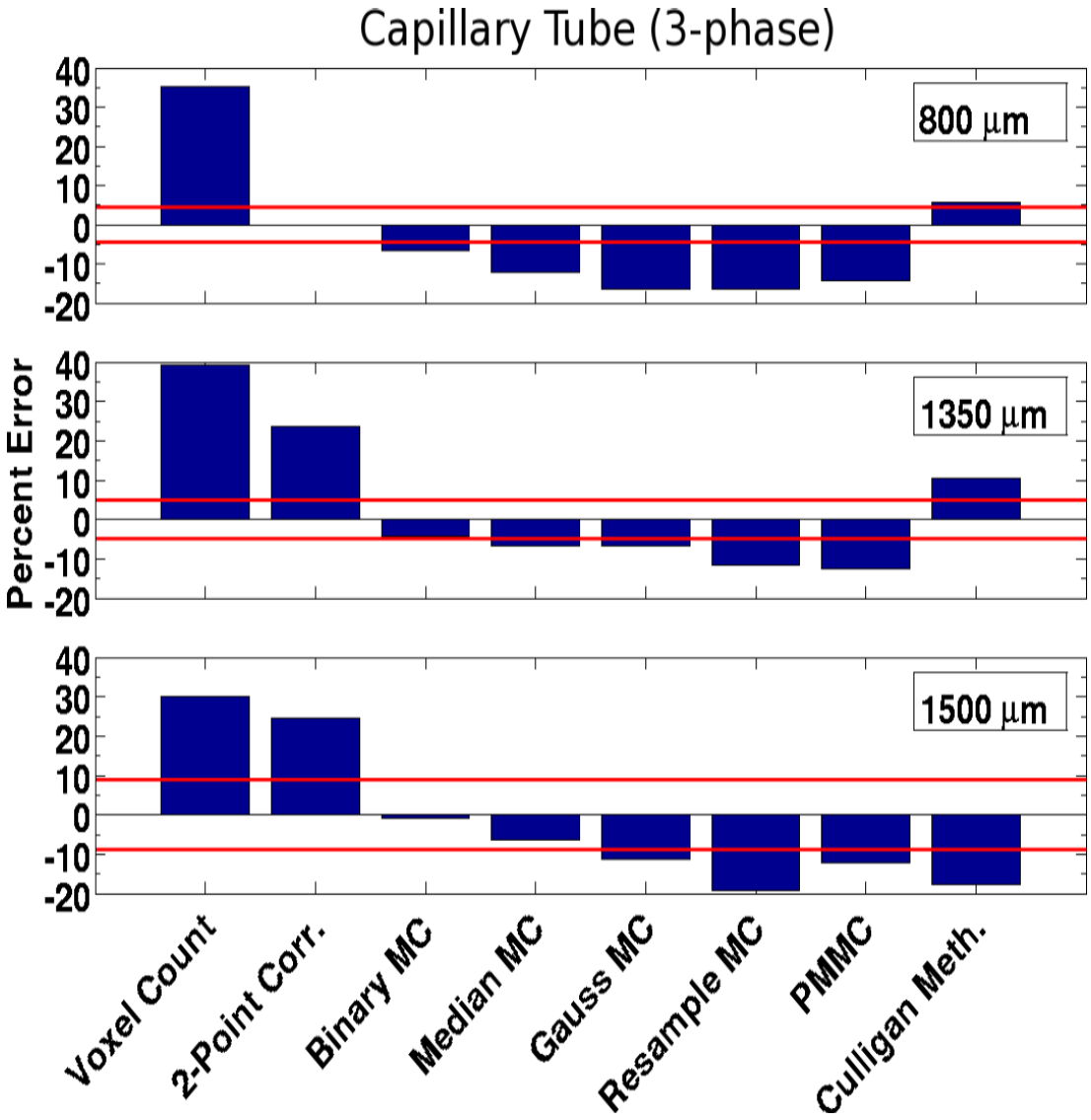

Figure 3.9: Relative errors for the a_{nw} estimates obtained from different image analysis techniques for the 13 $\mu m/voxel$ resolution capillary tube data. The horizontal red lines represent the error associated with the analytical estimate.

segmentation routine, the results suggest that the segmentation routine used in Culligan et al. [2004, 2006] was not as consistent as the segmentation routine presented here. In general, all estimates obtained from the MC methods, including the Culligan Method, are excellent considering the error associated with the analytical estimate.

The effect of voxel resolution on the resulting a_{nw} estimates was also investigated using the 800 and 1500 μm capillary tubes. The analysis of the high resolution CMT data was exactly the same as the analysis of the 13 μm data. The a_{nw} estimates obtained from the high resolution CMT image data area shown in Table 3.6 along with the 13 μm data. The results show that in both the 800 and 1500 μm tubes, doubling the resolution caused a decrease in the interfacial area estimates and therefore a decrease in the accuracy of the estimate. This is contrary to what would be expected since there are more voxels available for the construction of the isosurface in 6.5 μm data than in 13 μm data. Additionally, at higher resolutions it is expected that features such as the nonwetting-wetting-solid contact line would be better resolved, leading to more representative isosurfaces and a more accurate interfacial area estimate. Even at a resolution of 3.3 μm (approximately 4 times greater than 13 μm) no significant change in a_{nw} was observed. This shows that in this capillary tube system an increase in resolution did not result in an increase in accuracy for the interfacial area estimates. Only at a resolution of 1.6 μm was there considerable increases in the a_{nw} estimates and the interfacial area was greatly overestimated. The high values in the 1.6 μm data were caused by increased signal-to-noise ratio encountered in the original gray-scale data for this high of a resolution. It is possible that minor changes in the image analysis routine (i.e., more iterations of the anisotropic diffusion filter) could have eliminated some of this noise, however this was not attempted since the goal of this study was to test the image analysis method presented here and used in Porter et al. [2008a,b].

3.6 Summary and Conclusions

In this study, the techniques used in [Porter et al., 2008a,b; Culligan et al., 2004, 2006] for analyzing CMT image data to obtain phase distribution and interfacial area estimates was described and tested in detail. The technique involved three steps: (1) filtering of the original gray-scale image data with a median or anisotropic diffusion filter, (2) segmentation of the data into binary (or trinary) data sets using a k-means cluster analysis, and (3) construction of isosurfaces from the segmented data in the commercially available software package Amira^{TM}, which uses a generalized marching cubes algorithm. Phase distribution estimates such as porosity and saturation were obtained from the segmented data by counting voxels. Interfacial area estimates were obtained from the isosurfaces.

To test the reliability of the of the image processing method presented here, two experimental data sets were analyzed and compared to results obtained by other methods presented in the

Table 3.6: a_{nw} estimates for a series of voxel resolutions. Units are in mm^2.

Voxel Resolution	Method	800 μm	1500 μm
	Analytical Estimate	0.91	3.36
13 μm	**Binary MC**	0.85	3.32
	Median MC	0.8	3.15
	Gauss MC	0.76	2.97
6.5 μm	**Binary MC**	0.83	3.21
	Median MC	0.76	3.10
	Gauss MC	0.75	2.92
3.3 μm	**Binary MC**	–	3.34
	Median MC	–	3.14
	Gauss MC	–	2.96
1.6 μm	**Binary MC**	–	5.92
	Median MC	–	5.22
	Gauss MC	–	3.73

literature. The two data sets consisted of (1) a high precision bead pack and (2) air-water interfaces contained within three capillary tubes of different radii. The 2-phase high precision bead data was used to compare how the resulting estimates from k-means cluster analysis compared to results obtained from indicator kriging, which is freely available through 3DMA. Interfacial area estimates were computed by voxel counting, 2-point correlation functions, marching cubes and Blob3D. Four different marching cubes (Binary MC, Median MC, Gauss MC and Resample MC) estimates were computed for comparison purposes, all of which, except Binary MC, consisted of filtering the segmented data prior to constructing the isosurfaces in Amira^{TM}. The method presented here was also compared to Blob3D since it is a commonly used image processing software package. The capillary tube data served as a simple 3-phase system for testing the reliability of the interfacial area estimates. Voxel counting, 2-point correlation functions and four different marching cubes estimates were compared using the three capillary tube data sets, all of which were segmented by k-means cluster analysis. PMMC [McClure et al., 2007] estimates were also included in the comparison as well as estimates obtained with the method used by Culligan et al. [2004, 2006]. The effects of resolution on the resulting estimates were also investigated for both the high precision glass beads and the capillary tube data.

Porosity profiles (as a function of depth) for the high precision beads showed that there was no observable difference between the estimates obtained from the two different segmentation routines and two different resolutions. Additionally, the volume averaged porosity estimates obtained from either segmentation routines was within 1.5 % difference of the laboratory porosity

estimates. Interfacial area estimates showed that voxel counting and 2-point correlation functions significantly overestimated (25-45 %) the laboratory estimates, whereas all MC-based estimates, and Blob3D, were within 15 %. The interfacial area estimates obtained from the higher resolution data exceeded the lower resolution estimates by a factor of 1.04-1.09 in all cases. Furthermore, all interfacial area estimates obtained from data segmented by indicator kriging were slightly lower than the corresponding estimates obtained from data segmented by k-means, however the differences were minimal. Thus, it was shown that for the 2-phase, high precision beads the resulting estimates were not sensitive to the segmentation routine.

Capillary tube data showed that voxel counting and 2-point correlation functions resulted in interfacial area estimates that were significantly higher than the analytical estimate, whereas the MC-based estimates, including PMMC and the Culligan Method, were in good agreement with the analytical estimate. It was also shown that the MC methods generally underestimated the analytical estimate. The MC estimates with pixelation effects were closer to the analytical estimate than those that had been smoothed prior to constructing the isosurfaces, which suggests that smooth isosurfaces are not necessarily the best estimate when applying MC to CMT data. The interfacial area estimates obtained from Amira^{TM} were also in agreement with those obtained from PMMC. This was somewhat surprising since the PMMC algorithm bypasses the segmentation step and provides a better representation of the fluid surfaces at the three phase contact line. An increase in the resolution by a factor of 2 or 4 did not result in significant improvements in the interfacial area estimates, however an increase by a factor of 8 led to significant overestimation mainly due to noise produced at this resolution. Further filtering of the gray-scale data could perhaps eliminate some of this noise, as could changes in the experimental procedure, for instance by using longer exposure times during tomographic data collection.

Overall, we have shown that the method presented here and used in [Porter et al., 2008a,b] to obtain phase distributions and interfacial area estimates were in excellent agreement with measured values, as well as with other methods that are commonly used in the literature (i.e., indicator kriging via 3DMA, Blob3D and PMMC). In addition, the improvements to the segmentation routine presented here were found to result in more consistent interfacial area estimates than the routine previously used by our group [Culligan et al., 2004, 2006].

3.7 Acknowledgments

Porter and Wildenschild were supported by NSF-EAR-06101108 and NSF-EAR-0337711. The authors would like to thank Marcel Schaap for his assistance with the 2-point correlation function data analysis. Additionally, we would like to thank James McClure for the interfacial area estimates obtained from the porous media marching cubes (PMMC) algorithm. A por-

tion of this work was conducted at GeoSoilEnviroCARS (Sector 13), Advanced Photon Source (APS), Argonne National Laboratory. GeoSoilEnviroCARS is supported by the National Science Foundation - Earth Sciences (EAR-0622171) and Department of Energy - Geosciences (DE-FG02-94ER14466). Use of the Advanced Photon Source was supported by the U. S. Department of Energy, Office of Science, Office of Basic Energy Sciences, under Contract No. DE-AC02-06CH11357. We thank all of the staff for research support.

Chapter 4. Investigating Nonwetting-Wetting Phase Specific Interfacial Area in an NAPL-Water-Glass Bead System Using Computed Microtomography Data

Mark L. Porter[1], Dorthe Wildenschild[1], G. P. Grant[2] and J. I. Gerhard[3]

1. Department of Chemical, Biological and Environmental Engineering, Oregon State University, 102 Gleeson Hall, Corvallis, OR 97331, USA

2. Geosyntec Consultants, Guelph, Ontario, Canada

3. Dept. of Civil and Environmental Engineering, The University of Western Ontario, London, Ontario, Canada

Water Resources Research
2000 Florida Avenue N.W., Washington, DC 20009-1277 USA
To be submitted

4.1 Abstract

Computed microtomographic image data was collected and analyzed to estimate fluid-fluid interfacial area for drainage and imbibition in a NAPL-water-glass bead porous system. We present fluid-fluid interfacial area estimates associated with capillarity and wetting phase films, which comprise the total fluid-fluid interfacial area. The capillary associated fluid-fluid interfacial area was further divided into interfacial area associated with the bulk (mobile) wetting phase and the disconnected (immobile) wetting phase. The fluid-fluid interfacial area estimates were found to be in agreement with estimates presented in the literature. The total fluid-fluid interfacial area was shown to increase linearly as saturation tended toward zero, whereas the capillary associated interfacial area increased from zero at saturation of one to a peak value at approximately 0.20 percent saturation and then decreased as the saturation continued toward zero. The distinction between bulk wetting phase and disconnected wetting phase interfacial area showed that in this system the wetting phase was relatively well connected, even at irreducible saturation. In addition, the capillary pressure-saturation curves and porosity were used as input for the explicit interfacial area submodel proposed by Grant and Gerhard [2007a] and the resulting predicted interfacial area values were in excellent agreement with the observed data.

4.2 Introduction

Knowledge of the interfacial area between phases within porous media is important for quantifying flow and transport phenomena. Subsurface processes such as the dissolution of nonaqueous phase liquids (NAPLs) into groundwater, adsorption of contaminants onto solids, and volatilization of contaminants in the vadose zone are directly affected by the solid-fluid and fluid-fluid interfacial areas. In regards to NAPL dissolution, most models avoid the difficult, often impractical, task of estimating interfacial area by using an effective mass transfer coefficient, which is a combination of the interfacial area per volume and the intrinsic rate of the mass transfer process [Bryant and Johnson, 2002]. This approach provides an estimate for the mass transfer rate, however the coefficient is empirical, and thus, only applies to the conditions (i.e., pore geometry, flow rate, etc...) of the system from which it was obtained [Bryant and Johnson, 2002; Grant and Gerhard, 2007a]. Powers et al. [1992] conducted dissolution experiments and concluded that greater understanding of factors influencing NAPL-water interfacial areas is required to adequately describe the complexities of NAPL-water mass transfer in a variety of media.

In addition, a number of theories based on thermodynamic considerations have been developed that suggest there is a functional macroscopic relationship between capillary pressure

(P_c), wetting phase saturation (S) and the nonwetting-wetting phase interfacial area per volume [Leverett, 1941; Morrow, 1970; Hassanizadeh and Gray, 1993; Bradford and Leij, 1997; Oostrom et al., 2001; Dobson et al., 2006; Grant and Gerhard, 2007a,b]. Hassanizadeh and Gray [1993] hypothesized that the additional dependence of P_c on a_{nw} could provide a quantitative description of hysteresis typically observed in the empirical $P_c - S$ relationship.

Pore scale experimental and numerical investigations involving the quantification of fluid-fluid interfacial area per volume (IFA) in porous media have increased significantly in the past decade. Two experimental methods for estimating fluid-fluid interfacial area per volume have been presented in the literature, namely interfacial tracers [e.g., Kim and Rao, 1997; Kim et al., 1999b,a; Saripalli et al., 1997; Annable et al., 1998; Anwar et al., 2000; Schaefer et al., 2000; Costanza-Robinson and Brusseau, 2002; Chen and Kibbey, 2006] and high resolution imaging [e.g., Wildenschild et al., 2002; Culligan et al., 2004, 2006; Schnaar and Brusseau, 2005, 2006; Brusseau et al., 2007; Costanza-Robinson et al., 2008]. Similarly, pore-scale modeling techniques, such as pore network, pore morphology and lattice-Boltzmann, have also been used to estimate IFA [e.g., Reeves and Celia, 1996; Held and Celia, 2001; Bryant and Johnson, 2002, 2004; Dalla et al., 2002; Joekar-Niasar et al., 2007; Porter et al., 2008a]. Results from these, and similar studies, indicate that (1) the magnitudes of IFA reported vary considerably, and (2) there is disagreement between experimental measurements and pore-scale numerical predictions regarding the relationship between capillary-associated IFA and saturation. Recently, Grant and Gerhard [2007a] developed a model (Explicit IFA) that predicts the effective IFA using knowledge of only the $P_c - S$ curves and porosity. They compared their predicted interfacial area values to those reported by Culligan et al. [2004, 2006], which showed similar trends between predicted and observed IFA values with the predicted values for main drainage higher than the observed values by a maximum factor of 1.8 at the $a_{nw} - S$ peak.

There are typically two distinct contributions to the total fluid-fluid IFA (a_{total}) reported in the literature, namely capillary-associated IFA, a_{nw}, and film IFA, a_{film}, thus $a_{total} = a_{nw} + a_{film}$. Figure 4.1 illustrates the fluid-fluid interfacial areas distinguished in the two fluid-porous system in this investigation. Capillary-associated IFA includes all nonwetting interfaces in contact with the bulk, mobile wetting phase and disconnected wetting phase pendular rings [Gladkikh and Bryant, 2003], whereas film IFA pertains to the nonwetting phase in contact with the wetting phase films that exist on solids of pores occupied by the nonwetting phase [Gladkikh and Bryant, 2003]. In this study, the effective IFA, a_{eff} is also measured, which is defined as the IFA associated with the bulk wetting phase and the nonwetting phase, thus a_{eff} is the portion of the a_{nw} that is not associated with disconnected wetting phase, see Figure 4.1.

In general, tracer techniques measure the total fluid-fluid IFA and high resolution imaging techniques provide a direct measure of the capillary-associated IFA (since wetting phase films are not typically resolved). However, based on the assumption that the porous medium

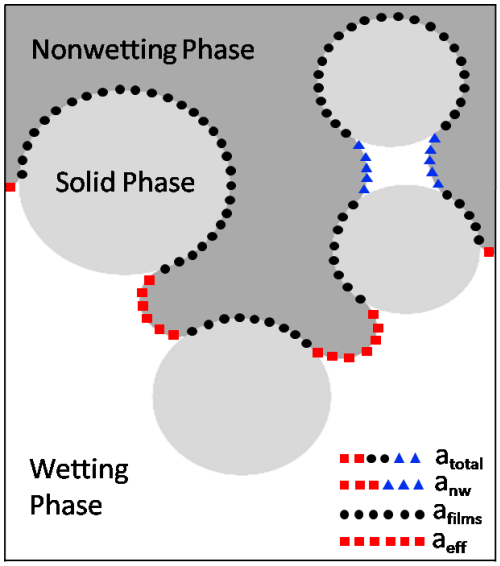

Figure 4.1: Illustration of the various fluid-fluid interfacial areas that may be distinguished in a two fluid-porous system.

is strongly water wet, and therefore, wetting phase films exist on all solid surfaces, the nonwetting phase IFA, a_n, can be used to infer the total fluid-fluid IFA (i.e., $a_n = a_{total}$). In a similar fashion, it can be assumed that IFA associated with the nonwetting-solid interface, a_{ns}, represents a_{film}. Additionally, IFA associated with the wetting-solid interface, a_{ws}, can be estimated from the high resolution image data. If wetting phase films exist on all solids in the porous medium, $a_{ws} = a_s$ for all saturation values, however, since wetting phase films were not directly observed in the data, changes in a_{ws}, as a function of saturation, were considered along with the other IFA estimates.

In this study synchrotron X-ray computed microtomographic (CMT) imaging techniques were used to obtain high resolution ($13\,\mu m/voxel$) 3D images for drainage and imbibition experiments in a NAPL-water-glass bead system. One of the primary motivations for this work was to investigate the relationship between $P_c - S - a_{nw}$ using experimental CMT data. To the best of our knowledge, the only 3D experimental measurements of $P_c - S - a_{nw}$ using CMT imaging techniques are those reported by Culligan et al. [2004, 2006]. Thus, there is a need for additional experimental data to further our understanding of multiphase systems and to validate analytical theories and numerical models. Furthermore, the experimental methods and image analysis routines used by Culligan et al. [2006] have been improved, which will be discussed in Section 4.3.2 and 4.3.3. The $P_c - S$ curves and porosity were input into the explicit

IFA submodel recently developed by Grant and Gerhard [2007a], which is discussed in Section 4.3.4, and comparisons between measured and predicted a_{eff} values are presented in this study.

4.3 Methods

4.3.1 Synchrotron X-ray Computed Microtomography

The experiments presented here were carried out at the GeoSoilEnviro Consortium for Advanced Radiation Sources (GSECARS) bending magnetic beamline, Sector 13, Advanced Photon Source (APS), Argonne National Laboratory. A short description of the synchrotron setup follows. For a detailed account of tomography and the synchrotron setup during these and similar experiments see Wildenschild et al. [2002, 2005]; Culligan et al. [2006], and references therein.

The synchrotron source produces polychromatic (white) radiation that is converted to a monochromatic (single energy) wavelength using a monochromator (channel-cut Si(111)) in the range of $8 - 45\,keV$. In these experiments, the water was doped with KI at a 1:6 mass ratio of KI:H_2O and the energy level for scanning was set to approximately $33.3\,keV$, which is slightly higher than the peak photoelectric adsorption energy for iodide. The use of the KI dopant increases the contrast between the water and NAPL phases. The monochromatic x-ray beam passes through the sample at a width of $50\,mm$ and a height of $5\,mm$, which is then converted to visible light using a YAG scintillator. The light is reflected to a CCD camera (MicroMAX $5\,MHz$) with a Nikon macro lens where the data is collected. The sample is mounted on a computer-automated stage for precise rotation and translation within the beam and was rotated twice from 0° to 180° in 0.5° steps to obtain 360 12-bit images. The raw data was processed in IDL^{TM} (Research Systems Inc.) to sharpen the edges, center the data around the rotation axis, and remove ring artifacts, after which gray-scale images were reconstructed via a back-projection algorithm [Rivers, 2001]. The gray-scale CMT image data consists of the x-ray attenuation coefficients and the resulting voxel size for this data set was $13\,\mu m/voxel$. A horizontal cross-section appears in the left image of Figure 4.2.

4.3.2 NAPL-Water Experiments

The experimental procedures for this study are similar to those used in Culligan et al. [2006], however improvements have been made to the experimental system. The major difference in these experiments is that the beads were loose packed in a glass column, whereas Culligan et al. [2006] used sintered glass beads packed in an acrylic column. The sintered glass beads resulted in significant void space between the porous medium and the column wall and it

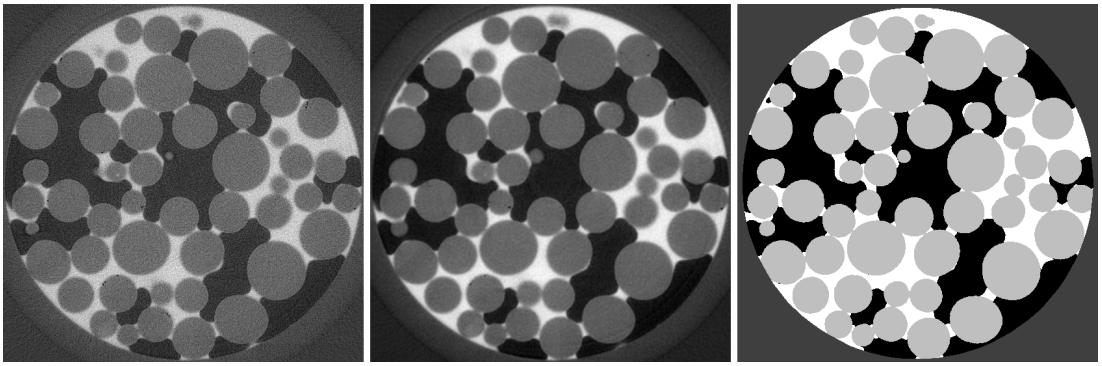

Figure 4.2: Comparison of gray-scale image (left), filtered gray-scale image using an anisotropic diffusion filter (middle) and the segmented image (right). The white, black and light gray regions are water, NAPL and solids, respectively.

was later determined in laboratory experiments (performed by this author), that the NAPL-water-glass bead-acrylic column system was a mixed-wet system; the oil preferentially wet the acrylic column whereas the water preferentially wet the glass beads. The combination of void space near the column wall and the mixed wettability resulted in a low nonwetting phase entry pressure and significant wall flow. The loose bead packing used in the experiments presented in this study allowed for the beads to settle next to the column wall reducing the void space along the walls; and the glass column eliminated the mixed wettability in the system. All other components of the experimental apparatus were similar to those used by Culligan et al. [2006]. Furthermore, improvements in detection and reconstruction procedures at GSECARS led to higher quality data; and the image analysis, segmentation and interfacial area algorithms were also modified to arrive at an overall improved data set. Details pertaining to the data analysis modifications can be found in Porter and Wildenschild [2008].

The glass column had an inside diameter of $7.0\,mm$ and was $25.0\,mm$ in length. The column was packed with loose soda lime glass beads ($\rho = 2.5\,g/cm^3$) with diameters ranging from $0.6 - 1.4\,mm$ and an average bead size of $0.85\,mm$. The porosity of the sample was $36\,\%$. A semi-permeable, hydrophilic membrane was placed at the bottom of the column to prevent NAPL from entering the water line. The water line was connected to a syringe pump (Gilson 402, Gilson Inc.), which precisely controlled the amount of water pumped into and out of the porous medium. A small rubber stopper containing a NAPL outlet tube connected to a reservoir was placed inside the column in contact with the top of the porous medium. The NAPL used in this study was Soltrol 220 (Chevron Philips, $\rho = 0.79\,g/cm^3$) dyed red with Oil Red O (Sigma Aldrich). The pressure of each phase was measured in the fluid lines above and

below the porous medium throughout the entire experiment. The experiments were conducted at a flow rate of 0.6 ml/hr. A quasi-static point on the $P_c - S$ curve was obtained by pumping a precise amount of water into (imbibition) or out of (drainage) the column, shutting the pump off and then waiting for the system to equilibrate. It was assumed that the system was at near-equilibrium conditions after 15 minutes. At that time a $5\,mm$ section in the middle of the column was scanned to collect the CMT image data. In this manner a primary drainage and two imbibition and drainage $P_c - S$ curves were measured and imaged.

4.3.3 Image Analysis

The gray-scale CMT images required further image analysis to accurately quantify the phase distributions and IFA. Phase distributions (i.e., solid, wetting and nonwetting phase volume fractions) were quantified via a segmentation routine and IFA was quantified using the commercially available image analysis software AMIRA^{TM}. Segmentation was performed first to create a trinary data set from which porosity and saturation values were estimated. IFA was subsequently estimated using the trinary data such that the IFA values for each phase corresponded to the volume fraction estimates obtained via segmentation. Only the most necessary details pertaining to the image analysis procedure are provided below, a full description can be found in Porter and Wildenschild [2008].

The first step in the image analysis was to filter the data to remove random noise in the original gray-scale data (see Figure 4.2). An anisotropic diffusion filter was used, which is a mathematically formulated diffusion process that promotes intra-region smoothing over edge smoothing [Perona and Malik, 1990; Gerig et al., 1992]. A comparison between the original gray-scale data and the filtered data is provided in Figure 4.2. Qualitatively, it appears that the filter successfully removed the noise from the original data while adequately preserving edges within the image. However, the edges in the original image were relatively smooth to begin with, thus the edge enhancement obtained using the anisotropic diffusion filter was minimal (see [Porter and Wildenschild, 2008]).

After processing the data with the anisotropic diffusion filter, a k-means cluster analysis (CCHIPS[1]) was performed. The k-means cluster analysis transformed the gray-scale data into a data set containing k values (or clusters). K-means is an unsupervised learning algorithm that maximizes the difference between pixels in different clusters and minimizes the differences between pixels within the same cluster [MacQueen, 1967]. Initially, the algorithm randomly chooses cluster centers and iteratively updates the centers until they are optimized (i.e., the center for each cluster does not change) [MacQueen, 1967]. Ideally, the gray-scale data would

[1]Copyright 2001, The Imaging Research Center, Children's Hospital Medical Center, Cincinnati, OH, http://www.irc.cchmc.org/cchips.php

be transformed into a data set containing three clusters, one for each phase. However, for three clusters the code produced a thin film of solid phase at all nonwetting-wetting interfaces. This most likely occurred because the range of the solid phase intensity values was between the nonwetting and wetting phase intensity values, and the nonwetting-wetting phase boundaries were relatively smooth in the original gray-scale images. To overcome this difficulty, the k-means cluster analysis was only used to obtain a binary image where the wetting phase was separated from the nonwetting and solid phases. The nonwetting and solid phases were subsequently separated by using information about the solid phase locations obtained from the binary dry data set, resulting in a trinary data set.

Further complications were encountered since the data changed throughout a drainage (or imbibition) event. At high saturation values there were three distinct peaks (wetting, nonwetting and solid) in the intensity histograms, whereas at low saturation values the wetting phase peak was virtually nonexistent, see Figure 4.3. This change in intensity values had implications when using the k-means cluster analysis since the center associated with the wetting phase cluster shifted as the saturation changed. Because there was always a definite solid phase peak in the data, the center associated with the nonwetting and solid phase was consistent throughout all data sets, despite the change in the nonwetting phase. The changes in the wetting phase center caused the solid phase to be clustered with the wetting phase at low saturation and not with the nonwetting phase, thus causing errors in the volumetric fraction and IFA estimates at low saturations.

In order to minimize the variability of the wetting phase center, the fully saturated data set was concatenated with every other data set prior to applying the k-means cluster analysis. This effectively created a distinct wetting phase peak in the histogram of the data being processed; resulting in a consistent wetting phase center and a consistent wetting phase cluster classification throughout all data sets. The results from the segmentation algorithm are illustrated in Figure 4.2. Porosity and saturation values were quantified by counting the pixels of each phase. The average porosity was 0.36 and the porosity profile is presented in Figure 4.4, which reveals significant variability throughout the imaged section of the porous medium.

The total interfacial area for the solid, a_s, wetting, a_w, and nonwetting, a_n phases was approximated via a generalized marching cubes algorithm in Amira^{TM}, which generates isosurfaces between phases, based on a single isovalue that represents the value separating one phase from the other phases. In this analysis the trinary data was transformed into three binary images, one for each phase, and then smoothed with a Gaussian filter (3x3x3 kernel) prior to constructing the isosurfaces. The isovalue for each isosurface was set to 0.5, which is half of the maximum and minimum values in the data. The interfacial areas, a_{nw}, a_{ws} and a_{ns} were subsequently estimated from the following equations:

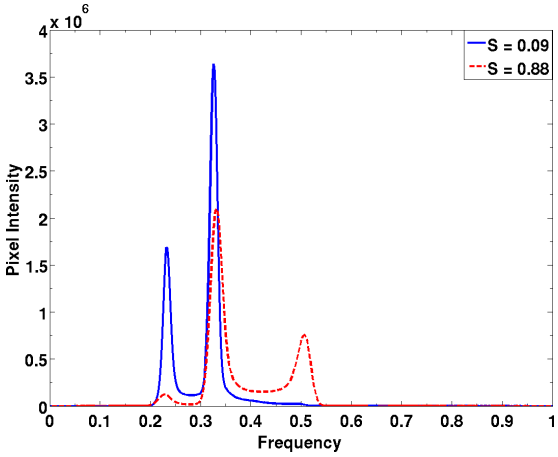

Figure 4.3: The left peak represents the bulk of the nonwetting phase, the middle peak represents the bulk of the solid phase and the right peak represents the bulk of the wetting phase. At high saturation there is a definite wetting phase peak, whereas at low saturation the wetting phase peak is virtually undetectable.

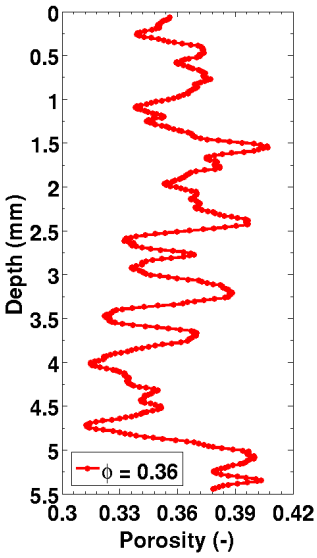

Figure 4.4: Porosity as a function of depth estimated form the CMT image data.

$$a_{nw} = \frac{1}{2}\left(a_w + a_n - a_s\right)$$
$$a_{ws} = \frac{1}{2}\left(a_w + a_s - a_n\right)$$
$$a_{ns} = \frac{1}{2}\left(a_s + a_n - a_w\right). \tag{4.1}$$

It is noted that Eq. 4.1 assumes perfect contact between all isosurfaces obtained from the marching cubes algorithm, which has been shown to be difficult to obtain, especially near the contact line between the three phases [Dalla et al., 2002; McClure et al., 2007]. The use of a single isovalue for all three data sets resulted in good contact between all phases. The validation and reliability of the interfacial area estimates obtained from this approach was discussed in detail in Porter and Wildenschild [2008].

4.3.4 Explicit IFA Submodel

Recently, Grant and Gerhard [2007a] presented the explicit IFA submodel which is a modification of the thermodynamic model of the two-fluid capillary - saturation relationship presented by Leverett [1941] and Morrow [1970], and later extended to three fluid systems by Bradford and Leij [1997]. Only the most necessary information pertaining to the Explicit IFA Submodel are presented here, for a full description see Grant and Gerhard [2007a]. Briefly, the thermodynamic approach assumes that interfacial area is proportional to the work applied to the system, the magnitude of which is the area under the capillary pressure - saturation curves [Grant and Gerhard, 2007a]. Thus, with the explicit IFA submodel, interfacial area may be predicted from knowledge of the capillary pressure - saturation curves, which is already required by multiphase flow models. The explicit IFA model incorporates five modifications to the basic thermodynamic model, which include (1) constitutive relationships for heterogeneous media, (2) continuity of saturation history, (3) the conversion from total to effective interfacial area per volume, (4) accounting for energy losses, and (5) accounting for NAPL dissolution. Modifications (2)-(4) allow for the comparison between the measured and predicted a_{eff} values in this study. The predicted a_{eff} values were obtained by numerically integrating the Brooks and Corey constitutive relationship.

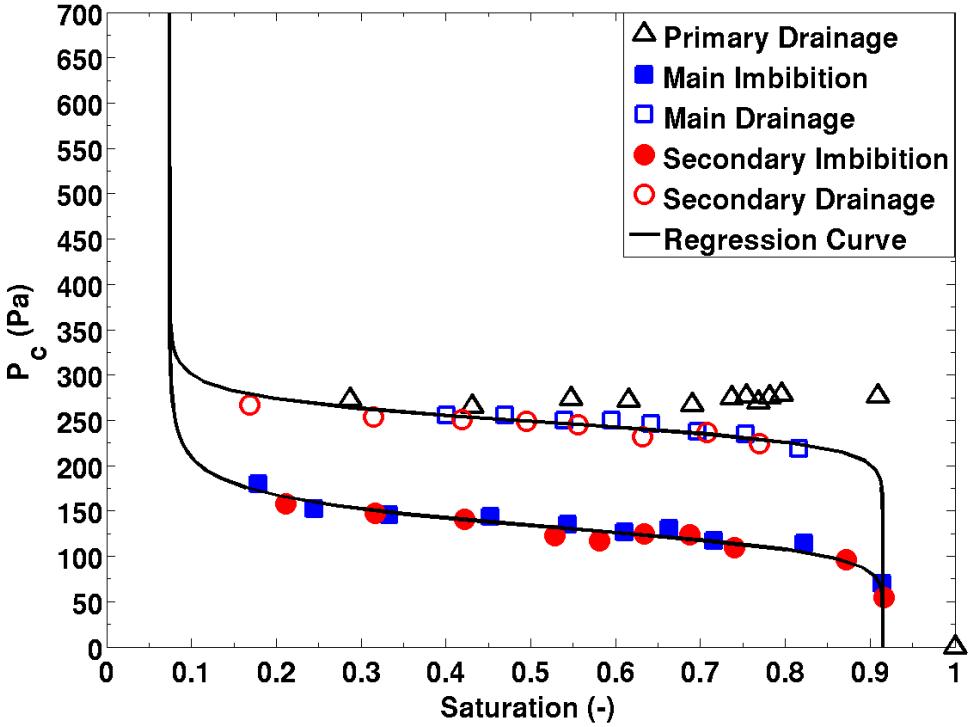

Figure 4.5: Hysteretic $P_c - S$ curves for the oil-water-glass bead system. Drainage and imbibition are represented by the open and closed symbols, respectively. The solid line represents the van Genuchten regression line. The irreducible saturation was 0.07 ($P_c = 1923\,Pa$), however the point is not shown here since it is represented by the regression line.

4.4 Results and Discussion

4.4.1 Capillary Pressure - Saturation Curves

The drainage and imbibition $P_c - S$ curves appear in Figure 4.5. These saturation values represent saturations for the entire column measured with the syringe pump during the experiments. The NAPL entry pressure occurs at approximately $220\,Pa$ and the flatness of the curve is characteristic of a medium to coarse grained sand with a relatively uniform pore size distribution. Liu et al. [1998] also observed relatively flat drainage curves for Soltrol and water in Columbia and Lincoln sands, as did Oostrom and Lenhard [1998] and Oostrom et al. [2003] for sandy porous media.

The reliability of the $P_c - S$ curves presented in Figure 4.5 was investigated by comparing them with two simple scaling relationships. The first consisted of scaling the air-water $P_c - S$ curves reported in Culligan et al. [2004] by the ratio (β_{ow}) of the air-water (σ_{aw}) and oil-water (σ_{ow}) interfacial tensions as proposed by Lenhard and Parker [1987]. The scaled air-water curves (not shown here) were in excellent agreement at high saturations for drainage and then diverged at low saturations due to the slope in the air-water curves and differences in the residual wetting phase saturation. The air entry pressure for the air-water $P_c - S$ curves in Culligan et al. [2004] was approximately $430\,Pa$, resulting in a scaled entry pressure of $224\,Pa$, which is essentially the same as the measured NAPL entry pressure ($220\,Pa$). The NAPL-water imbibition curves, on the other hand, showed little agreement and were consistently lower than the scaled air-water imbibition curves by a factor of 0.83.

The second scaling relationship used for comparison involved the ratio of the inflection point associated with the residual nonwetting phase on the imbibition curve (also know as the terminal pressure (P_T), see [Gerhard and Kueper, 2003]) and the nonwetting phase entry pressure for drainage (P_E). Gerhard and Kueper [2003] compiled an extensive list of the ratio of P_T/P_E for multiple fluid pairs and porous media, and the ratio ranged from 0.44 to 0.71. Additionally, Kool and Parker [1987] proposed a similar scaling relationship based on the ratio of the van Genuchten [1980] parameters α^i and α^d, where the superscripts i and d represent imbibition and drainage, respectively. Since α^d is inversely related to P_E [van Genuchten, 1980], this scaling relationship is essentially the inverse of P_T/P_E, and findings by Kool and Parker [1987] show that α^i/α^d ranges from $1.82 - 2.78$ for repacked porous media and multiple fluid pairs. The van Genuchten regression curves for drainage and imbibition are presented in Figure 4.5, and the ratio of $\alpha^i/\alpha^d = 1.89$ or $P_T/P_E = 0.53$, which is in the range of the values reported by Kool and Parker [1987] and Gerhard and Kueper [2003] for similar systems.

4.4.2 Saturation Profiles

Saturation profiles are presented here to aid in the interpretation of the $P_c - S$ curves presented in Figure 4.5 and the $a_{nw} - S$ relationship presented in Section 4.4.3 and correspond to measurements on a cube centered within the imaged section of the column. The volume of the cube was $\approx 128\,mm^3$ (375x375x415 voxels) and using 2-point correlation functions [Berryman, 1985; Schaap and Lebron, 2001], it was determined that this volume comprises an REV. Additionally, similar studies have shown that volumes of this size and smaller are indeed REVs [Culligan et al., 2004, 2006; Brusseau et al., 2007]. The cube was analyzed, rather than the entire imaged section, since the cube is more representative of a real porous medium; it is possible the column walls have some effect on the flow within the system and therefore would effect saturation and interfacial area estimates. Average saturation values were calculated for the entire imaged

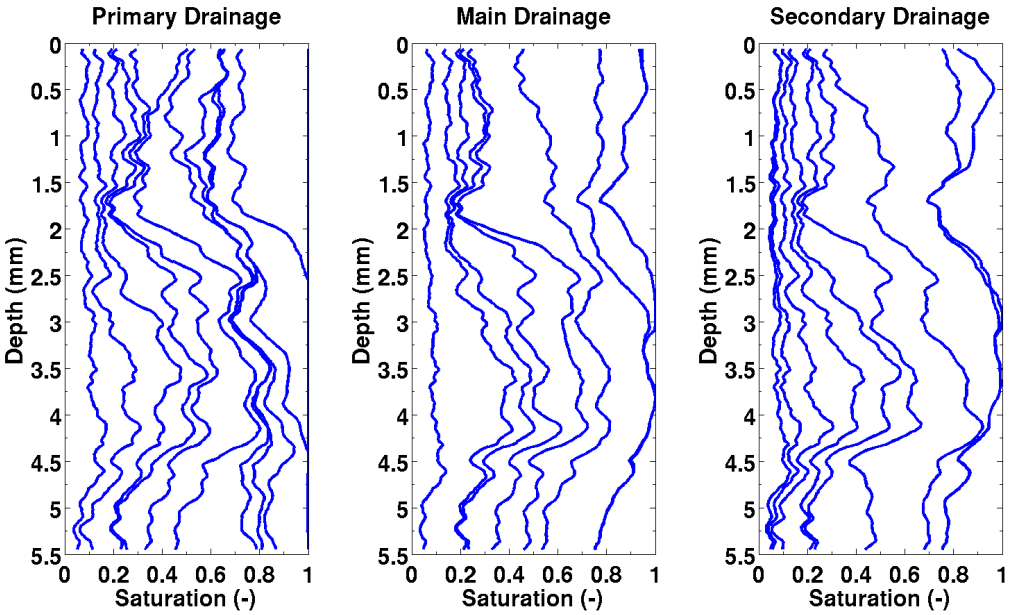

Figure 4.6: Saturation as a function of depth for all drainage points.

section to compare with the cube estimates, providing a measure of the amount of wall flow in the system. The difference between saturations in the cube and imaged section of the column was less than 2 % for all measurements, indicating that wall effects were minimal.

Figures 4.6 and 4.7 show the saturation profiles for all static drainage and imbibition points, respectively. It is evident from the saturation profiles that there were two relatively large saturation gradients at depths of approximately 2 mm and 4.25 mm in all drainage and imbibition cycles. The figures are strikingly similar to the air-water saturation profiles presented by Culligan et al. [2006], despite the difference in fluids and pore geometry. Figure 4.6 reveals that above 2 mm, drainage was relatively uniform for all $P_c - S$ points in all cycles suggesting there was a connected network of relatively large pores at those depths. However, from approximately 2-4 mm drainage was significantly restricted until higher pressures were attained. The porosity profile (see Figure 4.4) shows multiple regions in which the porosity decreased significantly over a short distance at depths from 2-4 mm. The drainage behavior observed here is consistent with a pore geometry containing only a few large connected pores (the remaining comprised of smaller connected pores), since the nonwetting fluid only enters large pores at low pressures. Below a depth of 4 mm drainage was not significantly restricted for low pressures, suggesting there was a network of large connected pores at those depths as well.

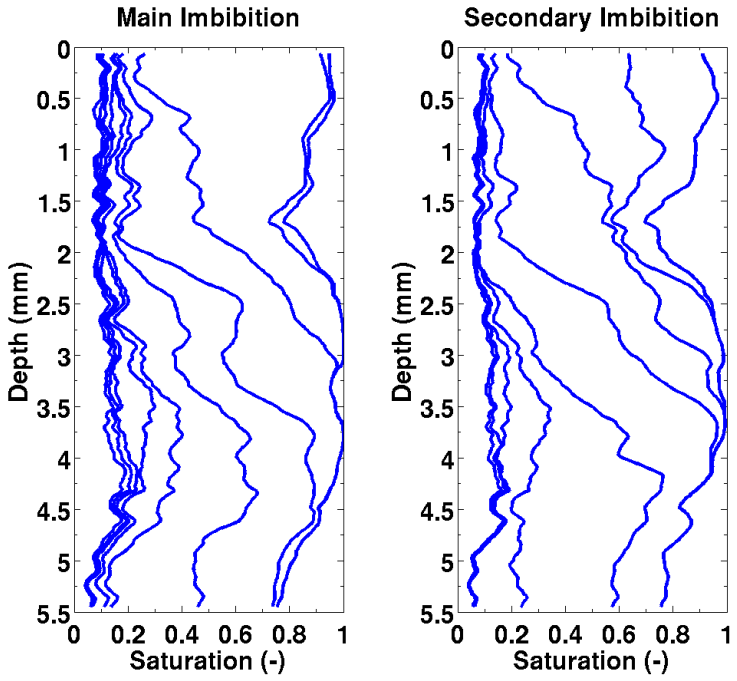

Figure 4.7: Saturation as a function of depth for all imbibition points.

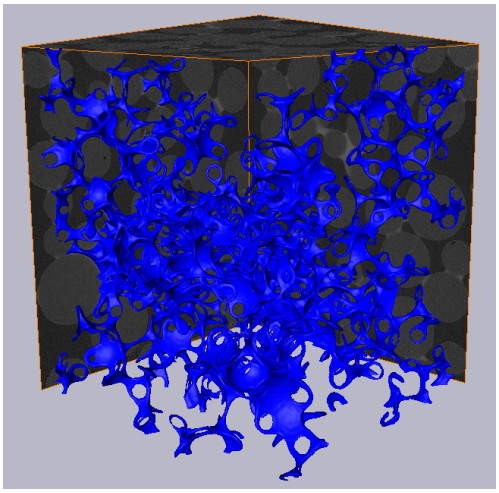

Figure 4.8: Illustration of a wetting phase path connected from the top to the bottom at an average wetting phase saturation of 0.08 during main drainage. Water enters and exists the volume primarily through the bottom face.

The saturation profiles observed during imbibition (see Figure 4.7) reveal that the flow in the system was primarily plug flow. At high pressures, the small increase in saturation occurred relatively uniformly throughout the column, indicating that the connected water paths were primarily swelling rather than invading pores. A single connected water phase path (from top to bottom) was identified (see Figure 4.8) at an average saturation of 0.08 during main drainage. It was visually confirmed that connected paths led to the observed increase in saturation at shallow depths for high P_c values. Significant changes in saturation did not occur above a depth of 2 mm until the bulk of the water was capable of invading larger pores (i.e., the P_c was sufficiently low).

4.4.3 Interfacial Area Estimates

A few select examples of nonwetting and wetting phase isosurfaces used to estimate IFA values appear in Figure 4.9. The isosurfaces were taken from primary drainage, main drainage and secondary imbibition. The wetting phase isosurface for primary drainage shows the existence of numerous pendular rings and wetting phase bridges at a saturation of 0.09. The portion of the wetting phase isosurface associated with disconnected pendular rings is identified in the third column of Figure 4.9, indicating that at low saturations the wetting phase was relatively well connected in funicular patterns.

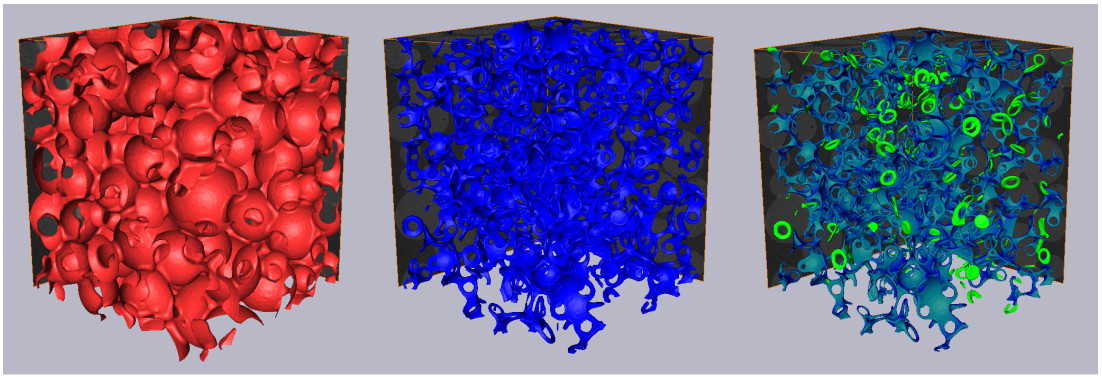

Primary Drainage (S = 0.09)

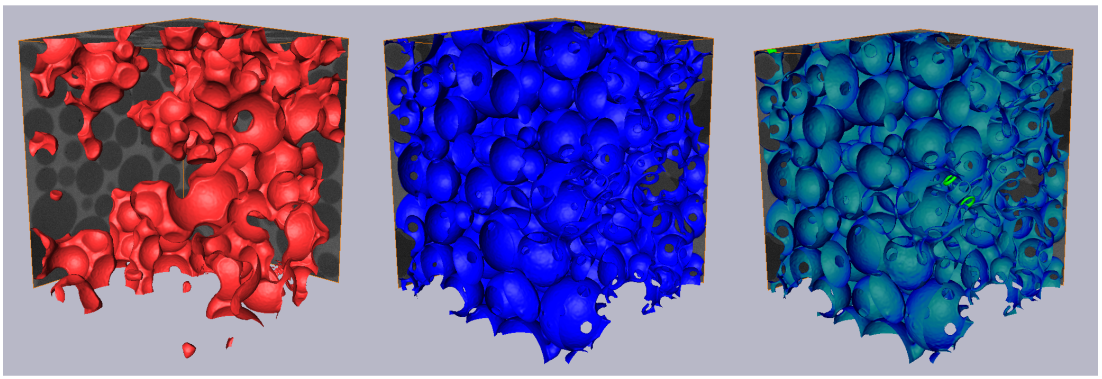

Main Drainage (S = 0.22)

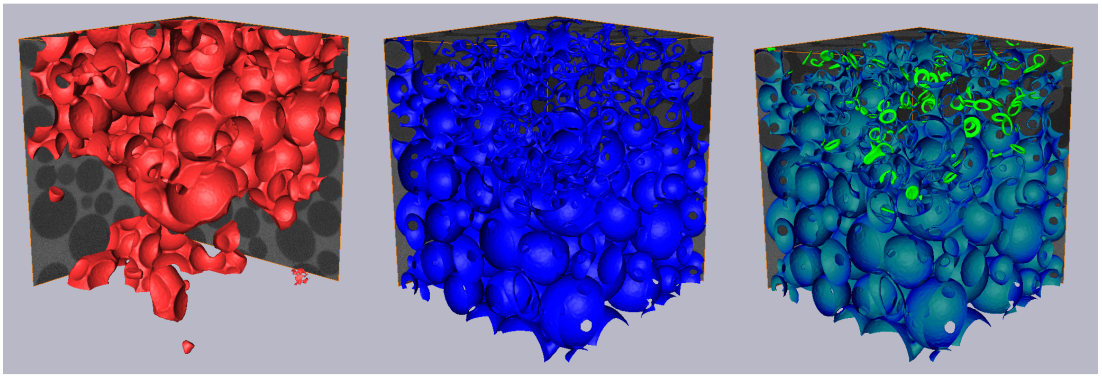

Secondary Imbibition (S = 0.53)

Figure 4.9: Examples of the nonwetting, a_n, wetting, a_w and the bulk wetting and disconnected wetting phase isosurfaces used to calculate a_{nw} and a_{eff}. The left, center, and right columns are the nonwetting phase (red), the wetting phase (blue), and the bulk (blue-green) and disconnected (green) wetting phases, respectively.

For main drainage, the nonwetting phase predominantly invaded the right side of the cube, suggesting that the pores were larger on this side. Additionally, a nonwetting phase finger has entered the cube from the bottom, suggesting that the nonwetting phase bypassed the constricting region and found a path into the pores from below. A relatively sharp wetting front is observed in the secondary imbibition isosurfaces, suggesting there was not a large network of connected, intermediate sized pores in the cube in which water could rise significantly.

IFA estimates for a_{nw}, a_s, a_{tot}, a_{film} and a_{ws} (as defined in Section 4.2) are shown in Figure 4.10. In all cases, the solid lines indicate drainage, whereas the dashed lines indicate imbibition. The overall behavior of these quantities as a function of saturation are in good agreement with those found in the literature [e.g., Bryant and Johnson, 2002; Gladkikh and Bryant, 2003; Bryant and Johnson, 2004; Cheng et al., 2004; Culligan et al., 2004, 2006; Brusseau et al., 2007; Costanza-Robinson et al., 2008]. It is clear that $a_s = 3.8\,mm^{-1}$ was the upper bound for all IFA estimates in this system. Estimates of a_s are of importance at low saturations (high capillary pressure) when water retention is controlled more by adsorption and less by the pore geometry [Hillel, 1998]. Additionally, a_s is a parameter in empirical equations such as the Kozeny-Carman relationship for estimating permeability.

As expected, the assumption that wetting phase films exist in the system, results in a_{total} estimates that approach a_s as saturation approaches zero. However, the best fit regression line ($a_{total} = -3.4S + 3.4$, $r^2 = 0.99$), suggests that a_{total} is approaching a value of 3.4 mm^{-1}, which is slightly lower than $a_s = 3.8\,mm^{-1}$. Additionally, a_{total} values appear to be curving up toward a_s at low saturations. This behavior was not observed in CMT measurements presented by Brusseau et al. [2007] or Costanza-Robinson et al. [2008], however in those studies there were a limited number of data points, especially at low saturations. In support of our findings, interfacial tracer [Anwar et al., 2000; Chen and Kibbey, 2006; Costanza-Robinson and Brusseau, 2002] and numerical modeling [Dalla et al., 2002; Gladkikh and Bryant, 2003; Bryant and Johnson, 2004] results show that a_{total} may indeed curve upwards at low saturations.

Figure 4.10 illustrates that a_{total} is primarily composed of a_{film}, whereas a_{nw} contributes only a small fraction to a_{total}, especially at low saturations. This is expected since in water-wet systems (i.e., those in which films exist) it is assumed that the films spread over all solids in the porous medium, whereas the nonwetting-wetting interfaces only occur as menisci associated with the bulk wetting phase, pendular rings and wetting phase bridges. The observed differences in a_{nw} and a_{total} illustrate that it is potentially important to understand which of the IFA components contribute to the flow or transport process of interest.

An important feature regarding the a_{total} estimates reported here, and in other CMT studies [Culligan et al., 2004, 2006; Brusseau et al., 2007; Costanza-Robinson et al., 2008], is that they are considerably lower than those obtained from interfacial tracer experiments [Kim et al., 1999b; Anwar et al., 2000; Costanza-Robinson and Brusseau, 2002; Brusseau et al., 2007].

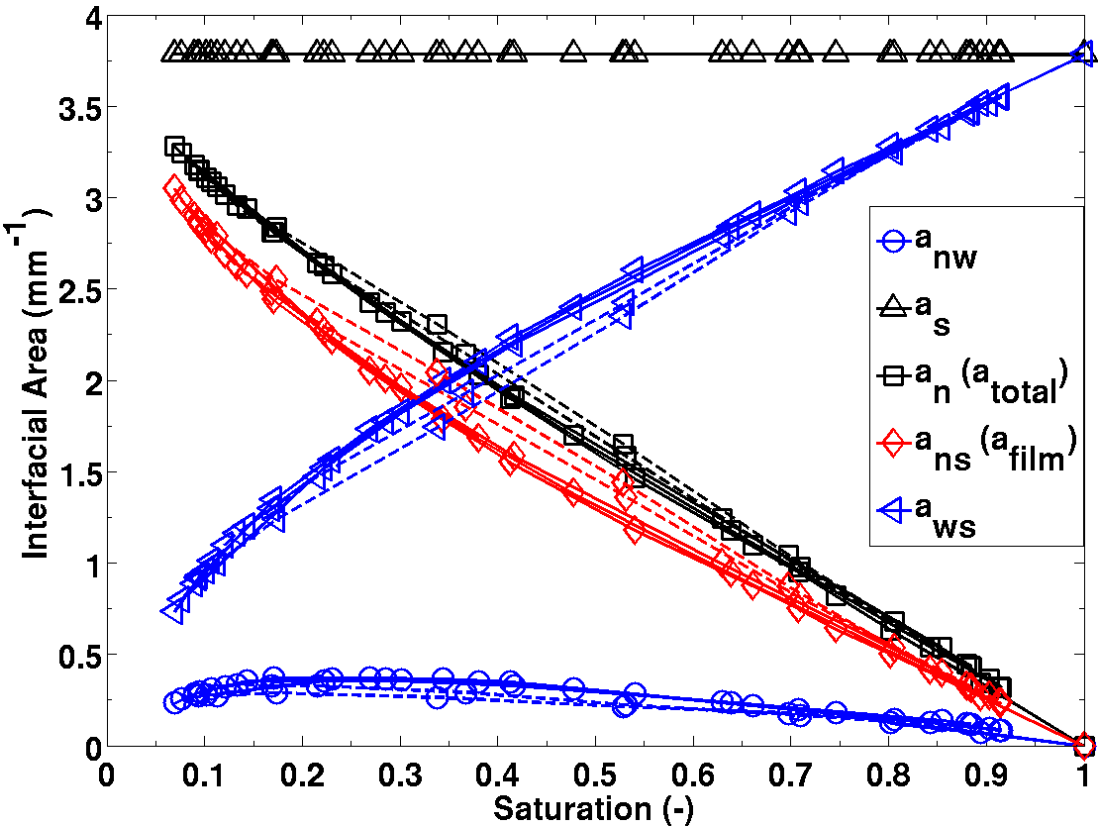

Figure 4.10: IFA estimates as a function of saturation obtained from CMT image data. This graph illustrate the various components of IFA that can be estimated from CMT data. The solid lines indicate drainage, whereas the dashed lines are imbibition.

This is most likely due to the fact that interfacial tracer methods are capable of measuring IFA associated with microscopic surface roughness, whereas CMT image data has a limited resolution (i.e., 13 μm in this study), at which microscopic features are not resolved. Kim et al. [1999a] presented scanning electron microscopy (SEM) images of glass beads that were coated with patchy and irregularly sized particles, contained indentations, and had smaller beads attached to them, which demonstrated that microscopic heterogeneities could have a significant influence on interfacial tracer IFA measurements. Thus, when considering processes controlled by IFA, it is important to consider the relative contribution of the different components of IFA.

Figure 4.10 also demonstrates that it is possible to investigate the complex relationship between the volume fraction of each phase and a_{nw}, a_{ns} and a_{ws}. These variables represent six of the seven primary geometric variables that enter the macroscopic conservation equations in the multiphase flow model proposed by Gray et al. [2002]. The only primary geometric variable that was not presented (or measured) is the common contact line between the three phases. Figure 4.10 clearly illustrates the differences in behavior during imbibition and drainage, which provides insights into the role of hysteresis in the system, which can assist researchers in the development of physically correct models for multiphase flow.

A primary interest in this study was the role of a_{nw} in the NAPL-water-glass bead system, thus Figure 4.11 shows a_{nw} as a function of saturation. Imbibition and drainage are clearly labeled to stress the locations relative to one another. All of the curves peak at saturations between 0.2 and 0.35, which is consistent with trends observed in CMT experiments by Culligan et al. [2004, 2006]. The magnitude of the curves also match well with the magnitudes reported by Culligan et al. [2004, 2006]. Brusseau et al. [2007] shows a_{nw} values that peak at saturations from 0.5 - 0.6. Modeling [Reeves and Celia, 1996; McClure et al., 2004; Joekar-Niasar et al., 2007; Porter et al., 2008a] and theoretical [Dalla et al., 2002; Bryant and Johnson, 2002, 2004; Grant and Gerhard, 2007a] predictions report curves that peak at saturations between 0.2 and 0.4. However, other numerical studies have shown the peak to occur at higher saturations for imbibition, drainage and scanning curves that follow primary drainage [Held and Celia, 2001; McClure et al., 2004; Joekar-Niasar et al., 2007]. Thus, it appears there is no consistent trend for the peak locations and differences in experimental results are most likely due to differences in the porous media.

The most noticeable difference between the behavior for experimental and pore-scale numerical a_{nw} estimates as a function of saturation, is that the curves presented here, and consistently in other CMT experimental studies [Culligan et al., 2004, 2006] Brusseau et al. [2007], show drainage a_{nw} estimates that are higher than imbibition estimates, whereas pore-scale numerical modeling results consistently predict imbibition a_{nw} values that are higher than drainage values [Held and Celia, 2001; McClure et al., 2004; Joekar-Niasar et al., 2007; Porter et al., 2008a]. Culligan et al. [2004, 2006] argued that a_{nw} values should be higher in drainage than in

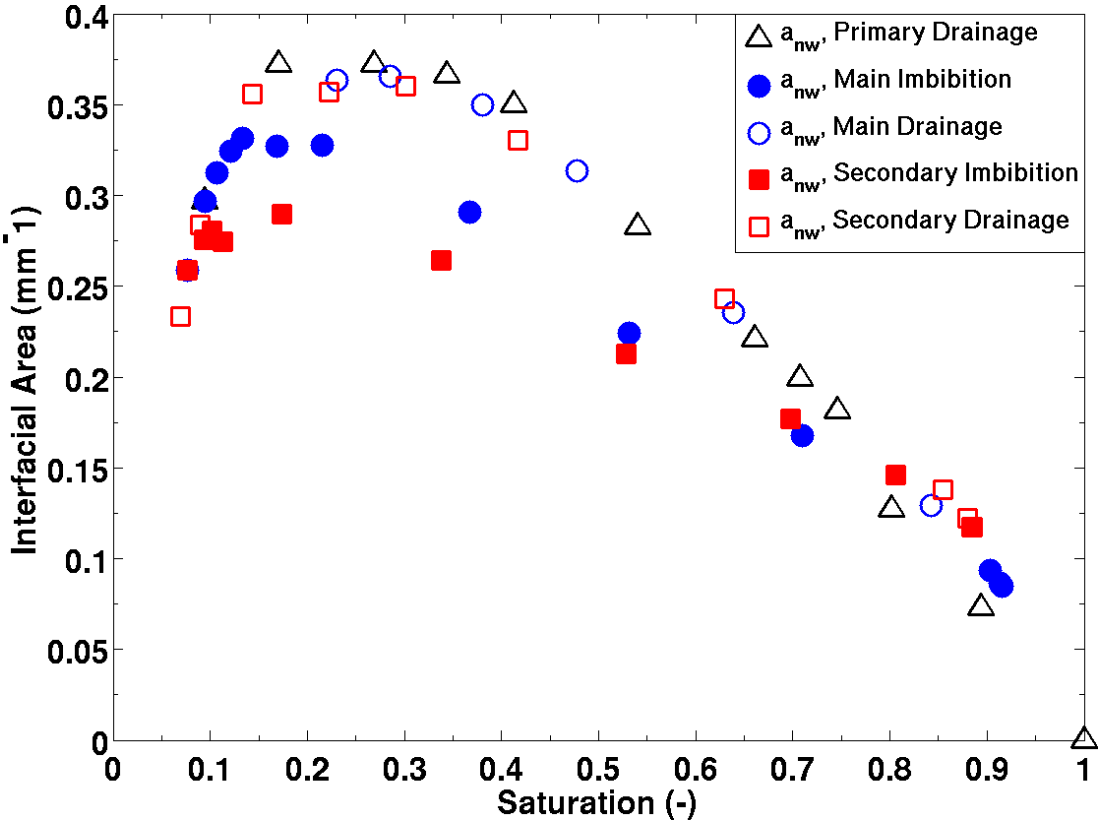

Figure 4.11: a_{nw} as a function of saturation. The solid lines indicate drainage, whereas the dashed lines are imbibition.

imbibition based on a simple capillary tube model. In their argument they claimed that during drainage the interface would be stretched (leading to higher interfacial area), whereas during imbibition the interface would be flatter (less interfacial area). It is noted that this argument only applies to a system that is not in equilibrium, since at equilibrium the interfaces would relax to the same shape. However, this argument may apply to the CMT data presented here, since the system was only allowed to equilibrate for 15 minutes resulting in quasi-equilibrium conditions.

In addition to a_{nw}, which includes all interfaces between the nonwetting phase and the bulk and disconnected wetting phase, in Figure 4.12 we present a_{eff}, which is the portion of a_{nw} associated with only the bulk wetting phase. Based on the histogram of all the distinct wetting phase regions in the square subvolume, it was assumed that those regions under a certain size (5000 voxels) were associated with disconnected wetting phase pendular rings and bridges, this assumption was required since only a square of the imaged section was analyzed. The validity of this assumption was verified by visual inspection of the disconnected regions identified, see Figure 4.9. Furthermore, visual observation of the connected wetting phase (in the cube) swelling for the first few imbibition steps verified that the funicular patterns were connected to the bulk wetting phase at the outlet of the column. Additionally, no swelling of the pendular rings was observed, suggesting that wetting phase films were not present in the system.

The difference between corresponding a_{nw} and a_{eff} in Figure 4.12 clearly shows the contribution of disconnected wetting phase films to a_{nw}. During drainage the formation of pendular rings in the cube does not occur until a saturation of approximately 0.70, and the number of pendular rings continues to increase throughout drainage as expected. Upon turn around for imbibition the first four (secondary) and five (main) imbibition steps indicate that the increase in wetting phase saturation was due to the expansion of the connected wetting phase paths and not the absorption of disconnected wetting phase. This was verified by calculating the difference between a_{nw} and a_{eff} and noting the points for which the difference was constant. The saturation values with a constant difference between a_{nw} and a_{eff} range from approximately 0.07-0.15 and are associated with the reversible work in the cube, since the only change in saturation was associated with swelling of the connected wetting phase and not invasion of pores or absorption of disconnected pendular rings. Subsequent imbibition points show some pendular rings reconnecting to the bulk wetting phase, however a significant proportion remain disconnected until a saturation greater than 0.50 is achieved and the rings are not fully absorbed until the residual nonwetting phase saturation is almost reached. This indicates that the majority of the disconnected wetting phase is associated with larger pores for which the water invaded last.

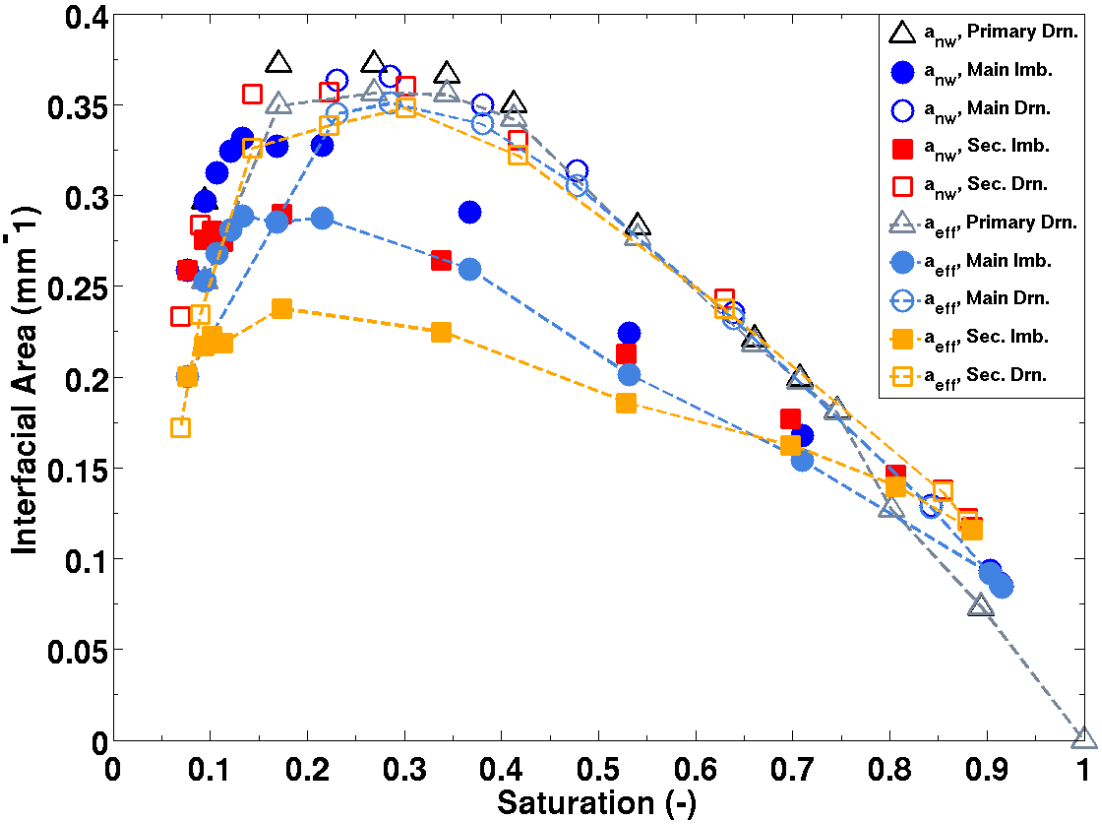

Figure 4.12: a_{nw} and a_{eff} as a function of saturation. The difference between a_{nw} and a_{eff} shows the amount of disconnected wetting phase in the system. The solid lines indicate drainage, whereas the dashed lines are imbibition.

4.4.4 Explicit IFA Predictions

The comparison between the observed and predicted a_{eff} values are presented in Figure 4.13. It is noted that no calibration of the model to the data was required for the prediction of a_{eff} using the explicit IFA submodel. Furthermore, the $P_c - S$ data for the entire column was used to predict interfacial areas for a subvolume of the full column. With this in mind, the comparison between the observed and predicted values is excellent, especially for main drainage and imbibition in the region near the peak of the $a_{eff} - S$ curves. The magnitudes the predicted main imbibition and main drainage curve peak is essentially identical to the magnitude of the corresponding observed data. The predicted primary drainage is lower than the observed primary drainage a_{eff} values by a maximum value of approximately 1.6 at the $a_{eff} - S$ peak. There are some discrepancies between the observed and predicted a_{eff} values at residual nonwetting phase saturation ($S_w = 0.90$) and irreducible wetting phase saturation ($S = 0.07$). These discrepancies at $S = 0.90$) are due to the shape and size of the residual nonwetting phase blobs. The residual nonwetting phase in the experiments (within the analyzed cube) was observed to consist of only a few small blobs and a couple larger ganglia, thus the IFA at this saturation was relatively small. In the explicit IFA submodel the predicted a_{eff} values are determined by the difference between the main imbibition and primary drainage $P_c - S$ curves, which predicts that a_{eff} is higher than the observed values by a factor of approximately 1.6. At $S = 0.07$ the model assumes that the bulk wetting phase is virtually nonexistent (i.e., the irreducible wetting phase saturation exists in the form of disconnected pendular rings), however it was observed that the wetting phase in the experiments was well connected at $S = 0.07$ indicating that irreducible saturation was not achieved. It should be noted that numerous authors have shown that irreducible saturation is more of a theoretical concept and the value achieved in experiments rarely corresponds to a saturation for which no more water may flow out of the porous medium due to an increase in capillary pressure [Dullien et al., 1989; Dullien, 1992; Corey, 1986; Miller et al., 1998].

4.5 Conclusions

In this study, 3D CMT image data was collected and analyzed to estimate fluid-fluid interfacial area for NAPL-water $P_c - S$ curves. Primary drainage and two imbibition and drainage hysteretic $P_c - S$ loops were measured and investigated. The second imbibition and drainage loop was similar in nature to the main imbibition and drainage loop showing reproducibility of the experiments. Furthermore, two simple scaling relationships were calculated in order to compare the $P_c - S$ curves to similar experiments presented in the literature. The scaling relationships indicated that the $P_c - S$ curves were in agreement with published data.

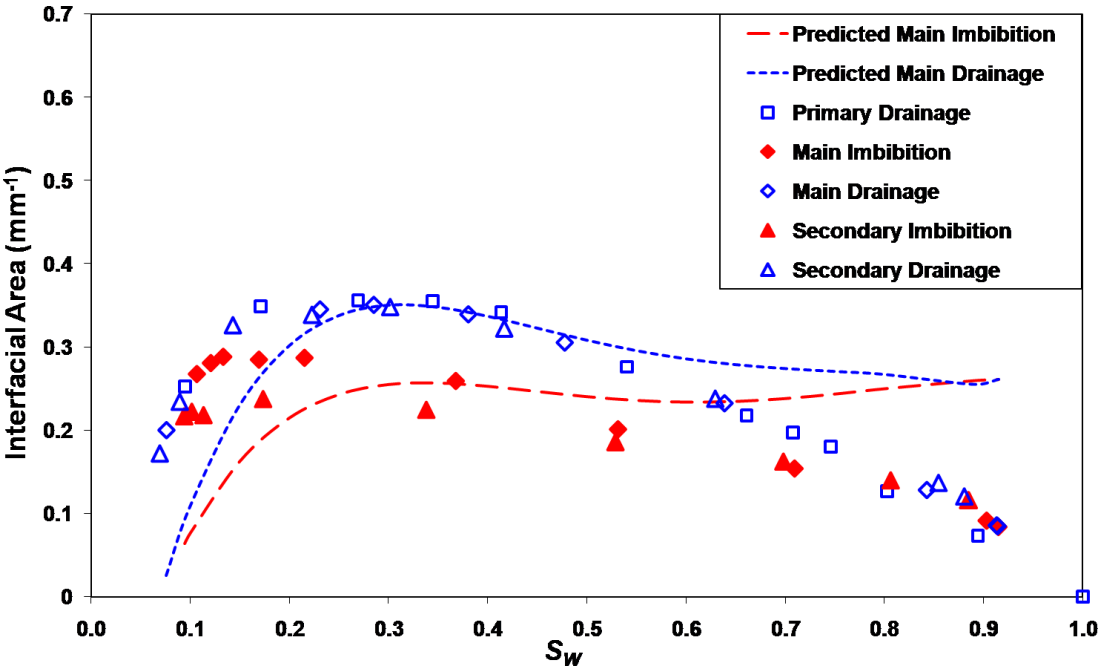

Figure 4.13: Comparison between observed (symbols) and predicted (lines) $a_{eff} - S$ curves. Predicted values were obtained from the explicit IFA model proposed by Grant and Gerhard [2007a], which requires on the $P_c - S$ curves and porosity. No calibration to the data was required.

Various components of fluid-fluid IFA were quantified by analyzing the CMT data of a section of the experimental column. The capillary-associated and effective IFA were directly observed and estimated from the CMT image data. Total and film fluid-fluid IFA was not resolved at the resolution of 13 μm, thus assuming that films existed in the glass bead system allowed us to infer these estimates from the CMT image data. Comparison of the total, film and capillary-associated interfacial IFA showed that a_{total} was primarily composed of a_{film}, which is expected since the solid surface area was greater than all of the estimated fluid-fluid IFA values. The linear trend of the total IFA was in agreement with trends observed in interfacial tracer and other CMT image experiments. The magnitudes of a_{total} were found to be similar to other CMT experiments, but significantly lower than interfacial tracer tests. This difference was attributed to resolution limitations in the CMT image data. It is noted that comparison of a_{nw} and a_{eff} values suggest that either wetting phase films were not present in the system or did not significantly contribute to flow in the system since it was observed that the disconnected pendular rings did not swell during imbibition. Thus, the estimates for a_{total} and a_{films} should be interpreted with caution. These estimates are reported in this study primarily to demonstrate that they can be estimated from CMT image data despite the lack of direct observation.

$a_{nw} - S$ and $a_{eff} - S$ curves were in agreement with experimental curves reported in the literature. The fact that a_{nw} is not constant for different saturation values supports the theory proposed by Hassanizadeh and Gray [1993] and Gray et al. [2002]. However, we were not able to investigate the uniqueness of the $P_c - S - a_{nw}$ relationship since scanning curves were not measured. The comparison between corresponding a_{nw} and a_{eff} values allowed for the identification of disconnected pendular rings. It was shown that the wetting phase was primarily composed of connected funicular water paths at low saturations in addition to disconnected pendular rings, thus it is likely that more water could have been drained from the porous medium. The observation of a connected wetting phase at low saturation values suggests that at low saturations in natural systems flow likely occurs along connected, funicular wetting phase paths rather than by displacement of the nonwetting phase or coalescence of disconnected pendular rings.

The explicit IFA submodel reported by Grant and Gerhard [2007a] was used to predict a_{eff} based on the measured $P_c - S$ curves and porosity of the porous medium. The predicted a_{eff} were in excellent agreement with the measured data for main drainage and imbibition near the peak of the $a_{eff} - S$ curve. Discrepancies between predicted and measured a_{eff} were observed at irreducible wetting phase saturation and residual nonwetting phase saturation. These discrepancies were due to differences in observed fluid configurations and configurations assumed in the model. The fact that the shape and magnitude of the predicted values are in agreement with the measurements is quite remarkable considering there was no calibration to

the measured data. The ability to accurately predict a_{eff} from $P_c - S$ curves and porosity using the explicit IFA submodel is a powerful tool, since measurement of a_{eff} is extremely difficult and expensive.

It is noted that our results pertain to an idealized porous system, which most likely does not hold for natural porous systems. However, it is precisely studies like this that are required to validate macro-scale models (as shown here) that can be applied to field scale studies. Additional experiments in which the entire porous medium is image are required in order to verify the connectedness of the fluid phases and the influence the connected fluid paths have on flow and transport processes. This is of importance since the many variables in macro-scale multiphase flow models based on thermodynamic considerations apply only to the portion of the fluids connected to the tensiometer used to measure pressure or the fluid reservoir in which the pressure was measured. Current macro-scale $P_c - S$ experiments are not capable of providing this level of detail.

4.6 Acknowledgments

Porter and Wildenschild were supported by NSF-EAR-06101108 and NSF-EAR-0337711. The author would like to thank Kendra Brown for her assistance with the experiments at Argonne National Lab and in the laboratory at Oregon State University. A portion of this work was conducted at GeoSoilEnviroCARS (Sector 13), Advanced Photon Source (APS), Argonne National Laboratory. GeoSoilEnviroCARS is supported by the National Science Foundation - Earth Sciences (EAR-0622171) and Department of Energy - Geosciences (DE-FG02-94ER14466). Use of the Advanced Photon Source was supported by the U. S. Department of Energy, Office of Science, Office of Basic Energy Sciences, under Contract No. DE-AC02-06CH11357. We thank all of the staff for research support.

Chapter 5. Comparison of Interfacial Area Estimates for Multiphase Flow Through Porous Media Using Computed Microtomography and Lattice-Boltzmann Simulations

Mark L. Porter[1], Marcel G. Schaap[2] and Dorthe Wildenschild[1]

1. Department of Chemical, Biological and Environmental Engineering, Oregon State University, 102 Gleeson Hall, Corvallis, OR 97331, USA

2. Department of Soil, Water and Environmental Sciences, University of Arizona, Tucson, AZ 85721, USA

Water Resources Research
2000 Florida Avenue N.W., Washington, DC 20009-1277 USA
To be submitted

5.1 Abstract

A multi-phase lattice-Boltzmann model was used to simulate computed microtomographic image data of air-water drainage and imbibition experiments in a glass bead porous system. The geometry of the porous medium as obtained from the experimental images was used to define the pore space geometry in the simulations. Both pressure and flux boundary conditions were investigated with the simulations. Results showed that, overall there was a good match between measured and simulated capillary pressure - saturation data, however there were some differences at low saturation values. Comparison of observed and simulated phase distributions within the pores showed remarkable correspondence for drainage over the entire simulated saturation range and for imbibition at high saturation values. At low saturation during imbibition, the phase distribution comparison was most likely affected by differences in the boundary conditions between the experiments and the simulations. Comparison of interfacial area - saturation curves also showed a close match for drainage, whereas the simulated imbibition curves were higher than observed curves by a maximum factor of approximately 3.5. Furthermore, the comparison between observed and simulated interfacial area - saturation curves showed that imbibition curves were lower than drainage curves for the observed data, whereas in the simulations imbibition was higher than drainage. This discrepancy is likely due to simplifying assumptions in the simulations, which do not fully capture the physics of the experimental system during imbibition.

5.2 Introduction

Multiphase flow and transport in subsurface environments is important in many scientific and engineering applications, often in situations of great economic concern, including the movement of fluids in the vadose zone where air and water share the pore space; in monitoring and remediation of contaminants, such as nonaqueous phase liquids (NAPLs), that have been introduced into the subsurface; in managing sequestration of CO_2 operations; and in enhanced oil recovery from underground reservoirs. Multiphase flow differs from single phase flow in that there exist two or more fluids that do not readily mix (immiscible fluids) in the pore space. Thus, an interface is present that separates the fluids, and this fluid-fluid interface is potentially a controlling factor for many multiphase flow and transport processes including capillary pressure dominated flow, entrapment of fluids in the pore space, dissolution of contaminants into passing water, volatilization of contaminants in the vadose zone and any chemical reaction or transformation that may occur between the two fluids.

Classical macro-scale multiphase flow models rely heavily on extensions of Darcy's law and empirical relationships that do not fully capture all of the important physical phenomena

of such multiphase systems [Muccino et al., 1998]. For example, a common approach used to model two-phase flow of air-water or NAPL-water systems in subsurface environments is to model each phase separately using Darcy's law and account for the interaction between the fluids by (1) introducing a relative permeability term and (2) by assuming the pressure gradients between the two phases are related by the capillary pressure [Dullien, 1992]. This approach does not explicitly account for fluid-fluid interfaces and the result is a relationship in which the macroscopic capillary pressure is assumed to be a function of wetting phase saturation only [Bear, 1988; Hassanizadeh et al., 2002]. Additionally, this traditional capillary pressure - saturation ($P_c - S$) relationship assumes that, at static conditions, the capillary pressure is uniquely described by the wetting phase saturation. Nevertheless many pore-scale fluid configurations can correspond to a given saturation [Gray and Hassanizadeh, 1991]. This suggests that in addition to saturation, a macro-scale variable that accounts for multiple pore-scale fluid configurations is required to accurately characterize multiphase systems.

Based on thermodynamic considerations that conserve mass, momentum and energy at the interfaces between phases, Hassanizadeh and Gray [1990, 1993] developed a functional relationship between capillary pressure, saturation and nonwetting-wetting phase interfacial area per volume ($P_c - S_w - a_{nw}$). Accordingly, the interfaces between phases are explicitly taken into account and the pore-scale fluid configuration is quantified by a_{nw}. Validation of this theory is currently of great interest, and both experimental and theoretical developments have recently been presented in the literature. Culligan et al. [2004, 2006] used computed microtomographic (CMT) image data from drainage and imbibition experiments to estimate interfacial area per volume. The data collected in these investigations was found to be consistent with the theory presented by Hassanizadeh and Gray [1990, 1993], however, due to the sparse number of data points, no attempt was made to investigate the uniqueness of the $P_c - S_w - a_{nw}$ relationship. Cheng et al. [2004] estimated a_{nw} for a 2D synthetic porous medium and concluded that a_{nw} lifts the ambiguity associated with the hysteretic nature of the $P_c - S$ relationship. Various researchers [e.g., Leverett, 1941; Hassanizadeh and Gray, 1993; Bradford and Leij, 1997; Oostrom et al., 2001; Grant and Gerhard, 2007a,b] have developed a theoretical framework for $P_c - S_w - a_{nw}$, yet further study is warranted, in large due to the lack of experimental data available.

In addition to experimental and theoretical work, pore-scale modeling techniques have been used to estimate a_{nw} [Berkowitz and Hansen, 2001; Gladkikh and Bryant, 2003] and investigate the $P_c - S_w - a_{nw}$ relationship [Reeves and Celia, 1996; Held and Celia, 2001; Dalla et al., 2002; Joekar-Niasar et al., 2007]. Reeves and Celia [1996] developed a pore network model consisting of spherical pore bodies and biconical throats, and concluded that the complex relationship was consistently smooth and well behaved for a wide range of capillary pressure and saturation values. Held and Celia [2001] developed a pore network model that included a

snap-off mechanism and the resulting $P_c - S - a_{nw}$ surface enclosed in the main hysteresis loop exhibited a pronounced concave curvature, thus $P_c = f(S_w, a_{nw})$ was not single valued, whereas they observed that $a_{nw} = f(S_w, P_c)$ was single valued and may be a preferable functional form. Dalla et al. [2002] simulated primary drainage in a random 3D packing of non-overlapping spheres using a pore morphology simulator [Hilpert and Miller, 2001] and estimated interfacial areas with isosurfaces generated by a standard marching cubes algorithm from discrete phase data. Their estimates were in good agreement with experimental estimates obtained from interfacial tracers, however, they concluded that interfacial areas could not be deduced from the primary drainage curve. This suggests that they did not observe a unique functional relationship between $P_c - S_w - a_{nw}$ in their numerical investigation. Joekar-Niasar et al. [2007] recently developed a pore network model and found that hysteresis was minimal in $P_c - S_w - a_{nw}$ when there was increased overlapping of pore bodies and throats in the pore size distribution. From this brief review it is clear that no definitive conclusions can be drawn from current experimental and numerical studies regarding the functional relationship of $P_c - S_w - a_{nw}$ to validate theories such as those proposed by Hassanizadeh and Gray [1990, 1993].

Accordingly, the focus of this study is to compare interfacial area estimates obtained from experimental CMT image data with those obtained from lattice-Boltzmann (LB) simulations. The experimental data used in this investigation was the air-water drainage and imbibition data obtained by Culligan et al. [2004]. A Shan and Chen type (hereafter, SC type) two-component model as described by Shan and Chen [1993, 1994] and Martys and Chen [1996] was used for the simulations in this study. The LB method was chosen over other pore-scale modeling techniques because of the availability of high resolution CMT image data of the pore geometry, which was used as input for the simulations and for model comparison. In addition, numerous authors have shown that LB model are capable of simulating 3D multiphase and multi-component fluid flow in complex porous systems [e.g., Martys and Chen, 1996; Tölke et al., 2000; Bekri and Alder, 2001; Sukop and Or, 2003; Pan et al., 2004; Vogel et al., 2005; Li et al., 2005; Schaap et al., 2007]. Pan et al. [2004] conducted a thorough investigation of drainage and imbibition in a synthetic packing of uniformly distributed spheres using a SC type model and observed good agreement between experimental and simulated results for the $P_c - S$ relationship. Vogel et al. [2005] compared three different pore-scale modeling techniques and concluded that, of the three, the LB model was able to simulate a more realistic nonwetting phase entry pressure. Schaap et al. [2007] obtained good agreement between LB simulated and measured $P_c - S$ data for the air-water drainage and imbibition data from Culligan et al. [2004]. The simulations presented here are unique in that they were conducted on the pore geometry (as imaged in the CMT experiments) covering the entire volume of the data presented by Culligan et al. [2004]. Additionally, this investigation compares interfacial area estimates obtained from

the experiments and LB simulations, which, to the best of our knowledge, has not yet been presented in the literature.

In Section 5.3 an overview of the experiments conducted by Culligan et al. [2004] will be presented. This will be followed by an overview of the LB model and a description of the simulations conducted in Section 5.4, which also includes a discussion of scaling lattice units to physical units, the boundary conditions employed and the dimensional analysis required to match experimental conditions in the simulations. Section 5.5 includes a description of the methods used for estimating interfacial area from the experimental and LB data. This will be followed by a presentation of the results in Section 5.6, which includes a discussion of the equilibration of the simulations, and a comparison between simulated and experimental $P_c - S$ curves, saturation profiles, cross sectional fluid distributions and $a_{nw} - S$ curves. Lastly, Section 5.7 will present the summary and general conclusions from the study.

5.3 Experimental Methods

This investigation focuses on the air-water drainage and imbibition experiments described by Culligan et al. [2004]. The experiments were carried out at the GeoSoilEnviro Consortium for Advanced Radiation Sources (GSECARS) bending magnetic beamline, Sector 13, Advanced Photon Source (APS), Argonne National Laboratory. The experiments were conducted in an acrylic column with an inside diameter of $7\,mm$ and $70\,mm$ length. The column was loose packed with soda lime glass beads with diameters ranging from $0.6 - 1.4\,mm$, to a porosity of 34%. A semi-permeable membrane was placed at the bottom of the column to prevent air from entering the water line. The top of the column was open to the atmosphere with measures to prevent evaporation and all capillary pressures were referenced to ambient atmospheric pressure. The column was initially dry packed and subsequently fully saturated. A primary drainage curve and two main imbibition and drainage cycles were measured.

A syringe pump (Harvard Apparatus, Inc.) was connected to the water line and used to pump a precise amount of water in or out of the column and then shut off to allow for equilibration. This was repeated multiple times in each cycle to obtain enough points to fill out the drainage and imbibition portions of the $P_c - S$ curve. Each point was allowed to equilibrate for 10 minutes and then imaging began, which took an additional 10 minutes. It was assumed that the system was near equilibrium after 10 minutes and this was verified since there was no evidence of fluid movement in the CMT images. The Darcy velocity for primary drainage and the first imbibition and drainage cycle was $1.8 \cdot 10^{-3}\,mm/s$, whereas the Darcy velocity for the second imbibition and drainage cycle was $1.4 \cdot 10^{-2}\,mm/s$. Pressure was measured directly above and below the imaged section as well as in the water line outside of the column.

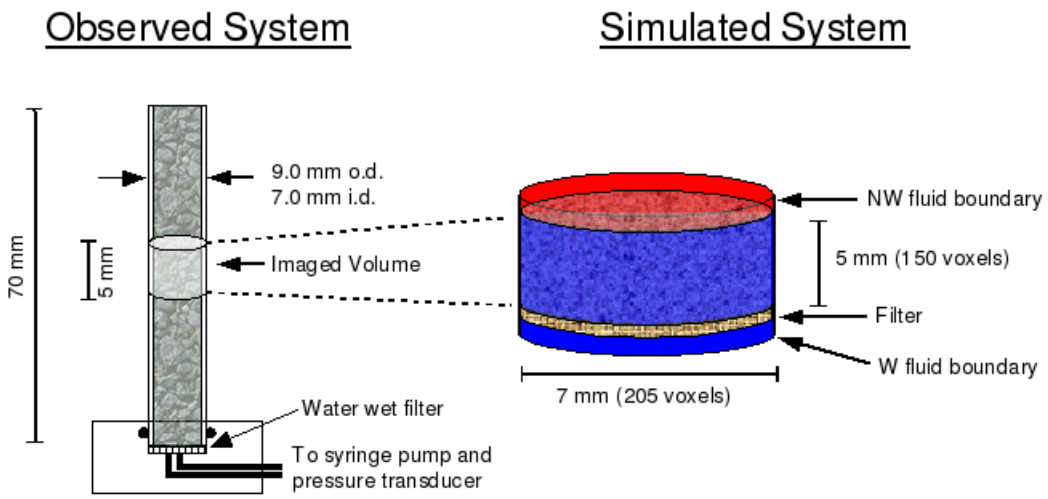

Figure 5.1: Illustration of the experimental system and the portion of the sample being modeled in the LB simulations.

CMT image data was collected for each $P_c - S$ point in the experiments. For detailed information pertaining to the use of synchrotron-based x-ray microtomography for applications of this nature see Wildenschild et al. [2002, 2005]. A 5 mm section of the column, see Figure 5.1 was imaged and the resolution of the 3D CMT images was 17 μm per voxel, which allowed for estimation of the solid, wetting and nonwetting phase distributions for each point on the $P_c - S$ curve. More details pertaining to the experiments may be found in Culligan et al. [2004].

5.4 Numerical Methods

5.4.1 Lattice-Boltzmann Model

The fundamental idea behind the LB modeling technique is the construction of simplified kinetic models that incorporate the essential physics of the microscopic processes such that the macroscopic averaged properties obey the desired macroscopic equations, in this case the Navier-Stokes equations [Chen and Doolen, 1998]. For a full description of the LB model used in this study, see Schaap et al. [2007]. In the multi-component SC type model, interaction between phases, namely the fluid-fluid cohesive force and fluid-solid adhesive force, is taken into account phenomenologically by modifying the macroscopic momentum variable.

The fluid-fluid cohesive force is calculated based on the presence of the other fluid in neighboring lattice sites and is given as:

$$\mathbf{F}_{c,\alpha}(\mathbf{x}) = -n_{\sigma}(\mathbf{x}) \sum_{i}^{19} G_a^{\alpha} n_{\alpha'}(\mathbf{x}+\mathbf{e}_i)\,\mathbf{e}_i,\ \alpha \neq \alpha' \tag{5.1}$$

where $n(\mathbf{x})$ is the number density, G_a^{α} is the fluid-fluid interaction potential, the vector $\mathbf{e}_i$ accounts for the relative position of neighboring lattice sites and the subscripts α and α' denote different components. It is the fluid-fluid cohesive force that gives rise to surface tension. The value of G_a^{α} is positive and identical for both fluid components. The choice of G_a^{α} determines the nature of the interaction between the two fluids; smaller values lead to unsharp interfaces and a considerable amount of diffusion from one component to the other, whereas larger values lead to sharp interfaces and purer component mixtures.

The fluid-solid adhesive force is determined by the presence of the solid phase at neighboring lattice sites and is given as:

$$\mathbf{F}_{a,\alpha}(\mathbf{x}) = -n_{\alpha}(\mathbf{x}) \sum_{i}^{18} G_c^{\alpha} s(\mathbf{x}+\mathbf{e}_i)\,\mathbf{e}_i \tag{5.2}$$

where G_c^{α} is the fluid-solid interaction potential and $s(\mathbf{x}+\mathbf{e}_i)$ is an indicator function that is 1 and 0 for solid and fluid lattice sites, respectively. In this model $G_c^1 = -G_c^0$ where G_c^1 is the interaction potential for the nonwetting phase and G_c^0 is the interaction potential for the wetting phase.

The choice of G_c^{α} along with G_a^{α} determines the contact angle in the simulations. These parameters are generally determined via simulation. Schaap et al. [2007] performed bubble and tube simulations to obtain suitable values for G_a^{α} and G_c^{α}. The bubble simulations indicated that $G_a^{\alpha} = 0.025$ was a suitable choice for the applications in this study. The lattice surface tension was determined by combining bubble simulations with Laplace's law to obtain a value of 0.1773. The tube simulations indicated that $G_a^{\alpha} = 0.0120$ corresponded to a 0° contact angle. However, it has since been proposed that G_a^{α} may be determined a priori using the Young-Laplace equation [Sukop and Thorne, 2006]. Using LB parameters the Young-Laplace equation takes the following form:

$$cos(\theta) = \frac{G_c^1 - G_c^0}{G_a} \tag{5.3}$$

where θ is the contact angle. Since $G_c^1 = -G_c^0$ Eq. 5.3 reduces to $cos(\theta) = 2G_c^1/G_a$ and one can easily show that $G_c^1 = 0.0125$ and $G_c^0 = -0.0125$ for a contact angle of 0° and $G_a = 0.025$. The value of G_c as determined by Eq. 5.3 was used in the new simulations presented in this study.

This is slightly different than the value obtained from the tube simulations used in previous simulations [Schaap et al., 2007]. It is noted here that further improvements to Eq. 5.3 have recently been published by Huang et al. [2007], in which Eq. 5.3 has additional dependence on the component densities. At the chosen G_a value, the system is sufficiently pure that this correction is small, thus it was not accounted for in this paper. It is noted that Eq. 5.3 makes the simulated contact angle slightly dependent upon curvature and therefore capillary pressure.

The fluid pressure, $p(\mathbf{x})$ is determined by the combined fluid mixture density, $\rho(\mathbf{x}) = n_1(\mathbf{x}) + n_0(\mathbf{x})$, at a given lattice site and the fluid-fluid interaction potential [Shan and Doolen, 1996]:

$$p\left(\mathbf{x}\right) = \frac{\rho\left(\mathbf{x}\right)}{3} + 12G_a n_1\left(\mathbf{x}\right) n_0\left(\mathbf{x}\right) \tag{5.4}$$

In this study, the macroscopic capillary pressure is defined in a similar manner as in the experiments; namely the difference between the pressure in nonwetting and wetting phases calculated at the nonwetting phase boundary (above the porous medium) and the wetting phase boundary (below the porous medium), respectively.

5.4.2 Scaling Lattice Parameters

The LB method was developed using dimensionless numbers, thus it is necessary to derive scaling relationships to compare lattice quantities to physical quantities obtained from the experiments. The physical quantities of interest in this study are length, capillary pressure and time. The CMT images provide information pertaining to the length scale. The resolution in the CMT images was $17\,\mu m$ per voxel, so a natural choice for the physical length scale is $dx = 17\,\mu m$. This is the length scale used in Schaap et al. [2007], however, this leads to a lattice that is at least 414x414x300 voxels for the imaged section of the air-water experiments. Due to computational demands it is not feasible to run simulations on a domain this large, thus Schaap et al. [2007] only simulated a subset (100 slices) of the imaged section. Another option is to coarsen the lattice resolution to $dx = 34\,\mu m$ by binning the CMT image data. The binning step consists of combining every 8 voxels into 1 voxel, thus reducing the lattice size to 207x207x150. This greatly reduces the computational demands at the cost of discarding some information in the binning step. The percent change in the solid surface area before and after binning was approximately 4%. Despite the introduction of error with binning, it was decided that simulating the entire imaged section was of greater interest than simulating a subsection of the imaged volume.

Knowledge of the length scale allows for the use of Laplace's law to scale capillary pressure. If $R = R^* dx$ where R^* is the lattice radius of curvature, then it can be shown that:

$$P_c = \frac{\sigma^* P_c^*}{\sigma dx} \tag{5.5}$$

where σ is the surface tension, dx is the length scale and the superscript * indicates lattice parameters. A similar scaling equation was used in Pan et al. [2004] and Schaap et al. [2007].

Time can be scaled by relating the physical kinematic viscosity of water, ν_w to the kinematic viscosity, ν^*, in the LB model:

$$dt = \nu^* \frac{dx^2}{\nu_w} \tag{5.6}$$

The kinematic viscosity is defined in the LB model as $\nu^* = (2\tau - 1)/6$ where τ is a relaxation parameter. In our simulations $\tau = 1$ for both components and $\nu^* = 0.1667$. Assuming $\nu_w = 1.01\, mm^2/s$ (@$20^\circ C$) and letting $dx = 0.034\, mm$, then $dt = 2 \cdot 10^{-4}\, ts/s$ (ts means time steps), which means that it takes $5000\, ts$ to simulate $1\, s$ of physical time.

5.4.3 LB Simulations

The model domain consists of a cubic lattice that is 207x207x166, which is larger than the porous medium on the sides and ends of the imaged column. The lattice exceeds the diameter of the cylinder by two pixels to preserve the solid boundaries of the cylinder, allowing for the use of the standard "bounce back" algorithm at column boundaries, while assuming that the column had the same wetting properties as the glass beads. A water-wet semi-permeable layer was included in the lattice at the bottom of the porous media to simulate the membrane in the experimental system and a buffer of eight fluid layers were included at the top (nonwetting) and bottom (wetting) boundaries of the lattice (see Figure 5.1).

Dimensional analysis [Culligan et al., 2004; Schaap et al., 2007] indicated that the dominating force in the experiments was capillarity. Based on these findings, the effects of gravity were not considered in the simulations, and the density and viscosity ratios between the simulated fluids were set to one. This greatly reduced the computational complexity of the model system.

In this study two different types of simulations are presented. In the first type of simulations flux boundary conditions were used at the inlet and outlet boundaries to mimic the experimental system as closely as possible. In the second type of simulations constant pressure boundary conditions were used at the inlet and outlet. Hereafter the two types of simulations will be referred to as flux simulations and pressure simulations.

The flux simulations were designed to follow the procedure used in the experiments, which consisted of pumping a precise amount of water at a specified flow rate into (or out of) the system and then allowing the system to equilibrate. In the simulations a flux boundary condition

was used to simulate the pumping of wetting fluid into and out of the porous medium. The boundary conditions were determined by scaling the characteristic flow rate from the experimental system using the Reynolds number:

$$Re = Re^* \longrightarrow \frac{u_w R_{char}}{\phi \nu_w} = \frac{u^* R^*_{char}}{\phi^* \nu^*} \tag{5.7}$$

where u is the Darcy velocity, R_{char} is the characteristic pore radius, ϕ is the porosity, ν is the kinematic viscosity and the superscript * indicates lattice parameters. It is u^* that was used as the flux at each boundary node. Two different flow rates were used in the experiments showing little difference in the results, thus two flux values were available from which to choose, namely $u^* = 0.00001\, mu\, ts^{-1}$ (where mu refers to lattice mass units) and $u^* = 0.00008\, mu\, ts^{-1}$. A flux of $0.00008\, mu\, ts^{-1}$ was used in the simulations presented here since the use of $0.00001\, mu\, ts^{-1}$ would require 8 times more iterations to imbibe/drain the same amount fluid. At a flux of $0.00008\, mu\, ts^{-1}$, approximately $50,000\, ts$ were required to obtain a 5 % change in saturation, which took about 1.25 day to run in parallel on four amd64 CPU (2.8 GHz) machines for a lattice domain of 207x207x166 voxels.

The flux simulations were conducted in sequence starting from a fully saturated porous medium. The final fluid distributions and capillary pressures from each simulation were used as initial conditions for subsequent simulations. In each simulation, a prescribed amount of fluid was allowed to drain or imbibe into the porous medium at a flux of $0.00008\, mu\, ts^{-1}$ followed by a period in which the flux was set to zero, allowing the system to equilibrate. In this fashion a primary drainage curve was simulated followed by a main imbibition curve.

The motivation for the pressure simulations was to investigate the difference in results obtained from different boundary conditions and different wetting/drying histories. Additionally, the standard method for determining $P_c - S$ curves in the laboratory is to employ constant pressure boundary conditions at the inlet and outlet of the column. In these simulations, a constant pressure was prescribed at each of these boundaries. The prescribed boundary conditions were determined from duct simulations, see Schaap et al. [2007]. The pressure simulations were conducted as single step drainage and imbibition simulations, which consisted of starting each simulation from a completely saturated (drainage) or dry (imbibition) porous medium. By conducting single step simulations all of the points on the curve could be simulated simultaneously, reducing the total amount of time to obtain a drainage and imbibition curve. Thus, in these simulations a primary drainage and primary imbibition curve were obtained.

5.5 Data Analysis

Estimates of saturation and interfacial area per volume were of primary interest in this study. Additional analysis was required to obtain this information from both the CMT and LB data. Due to differences in the data format, slightly different analysis methods were required. The CMT data consists of gray scale intensity values that were filtered using an anisotropic diffusion filter to remove random noise in the data. This was followed by segmentation using a k-means cluster analysis. Complete details pertaining to the procedure may be found in Porter and Wildenschild [2008]. The segmented data consisted of trinary data with each phase represented by a single integer value, which was used to estimate the porosity and saturation by counting voxels. The LB data did not require segmentation since the solid phase was already determined and a smooth gradient existed between the wetting and the nonwetting phases. The saturation was simply determined from component densities using the following rule: if the nonwetting component density was greater than or equal to the wetting component density at a given lattice site, then the lattice site was considered to be nonwetting phase, otherwise it was wetting phase.

Interfacial area estimates were obtained using Amira^{TM} for both the experimental and LB data. This software uses a generalized marching cubes algorithm to generate isosurfaces from which interfacial areas are estimated. Isosurfaces were generated for the total interfacial area for the solid phase, a_s, wetting phase, a_w, and nonwetting phase, a_n, for each point on the $P_c - S$ curve. In a three phase system the total interfacial area for each phase is defined as follows:

$$\begin{aligned} a_s &= a_{ws} + a_{ns} \\ a_w &= a_{nw} + a_{ws} \\ a_n &= a_{nw} + a_{ns} \end{aligned} \tag{5.8}$$

where a_{nw} is the interfacial area of the nonwetting - wetting interface, a_{ns} is the interfacial area of the nonwetting - solid interface, and a_{ws} is the interfacial area of the wetting - solid interface. From Eq. 5.8 it can be shown that the interfacial areas for the interfaces between the different phases are defined as follows:

$$\begin{aligned} a_{nw} &= \frac{1}{2}\left(a_w + a_n - a_s\right) \\ a_{ns} &= \frac{1}{2}\left(a_n + a_s - a_w\right) \\ a_{ws} &= \frac{1}{2}\left(a_s + a_w - a_n\right). \end{aligned} \tag{5.9}$$

For the experimental data, the segmented trinary data was used to create a binary data set for each phase. In the binary data sets the phase of interest was set equal to one and the other two phases were set equal to zero. Each of these binary data sets were used to estimate interfacial area for a_s, a_w and a_n in AMIRA^{TM} using an isovalues of 0.5. In practice, it was found that smoothing the data with a Gaussian filter (3x3x3 kernel) prior to generating the isosurface resulted in smoother, more realistic interfaces without substantially decreasing the interfacial area estimate.

For the LB data, the isosurface for a_s was generated from a two phase data set (i.e., completely saturated), whereas the isosurfaces for a_n and a_w were generated from three phase data sets. The choice of each isovalue proved difficult since the isosurfaces needed to correspond to the saturations reported and the surfaces need to be in contact with all other phases. Furthermore, contact between phases was not easily realized using a single isovalue for a_n and a_w since the values separating the two fluids were different from the values separating a fluid phase and the solid phase. It was determined that an isovalue that corresponded to the average component density used to estimate saturation resulted in good contact between two of the phases and satisfactory contact for the third. Thus, good contact was obtained for the nonwetting-wetting and wetting-solid interfaces, whereas satisfactory contact was obtained for the nonwetting-solid phases. Additional difficulties arose since the solid phase was a single integer value (zero) and the fluid phase data was continuous. Figure 5.2 illustrates a typical normalized histogram obtained from a LB simulation. The discontinuity between the solid phase and the fluid phases lead to blocky (pixelated) isosurfaces, thus resulting in higher interfacial areas between fluid and solids than between the two fluid phases. In practice, smoothing the LB data with a Gaussian filter (3x3x3 kernel) prior to generating the isosurface reduced the pixelation effects between the fluid and solid phases.

Dalla et al. [2002] investigated the error associated with Eq. 5.9 using a geometry that is representative of a wetting phase bridge that forms in porous media at low wetting phase saturation. They found that the marching cubes algorithm did not faithfully represent the thin wetting phase film near the three phase contact line. In this study, simulations in cylindrical (pixelated) capillary tubes were investigated and a_{nw} was estimated for the resulting spherical caps. Figure 5.3 shows the isosurfaces obtained for the fluid phases in a capillary tube with a radius of 5 pixels. Although the isosurfaces are smooth, it is apparent that the thin film of the wetting phase near the three phase contact line was not captured by the isosurfaces, thus introducing error into the interfacial area estimate. A comparison between the analytical and estimated a_{nw} for spherical caps of varying sizes is presented in Figure 5.3 along with the relative error obtained. The largest error is 12.4 % for a spherical cap with a radius of 6 pixels. The negative error values indicate that the estimates were lower than the analytical solution. The estimates were lower than the analytical solution in all case indicating that the method

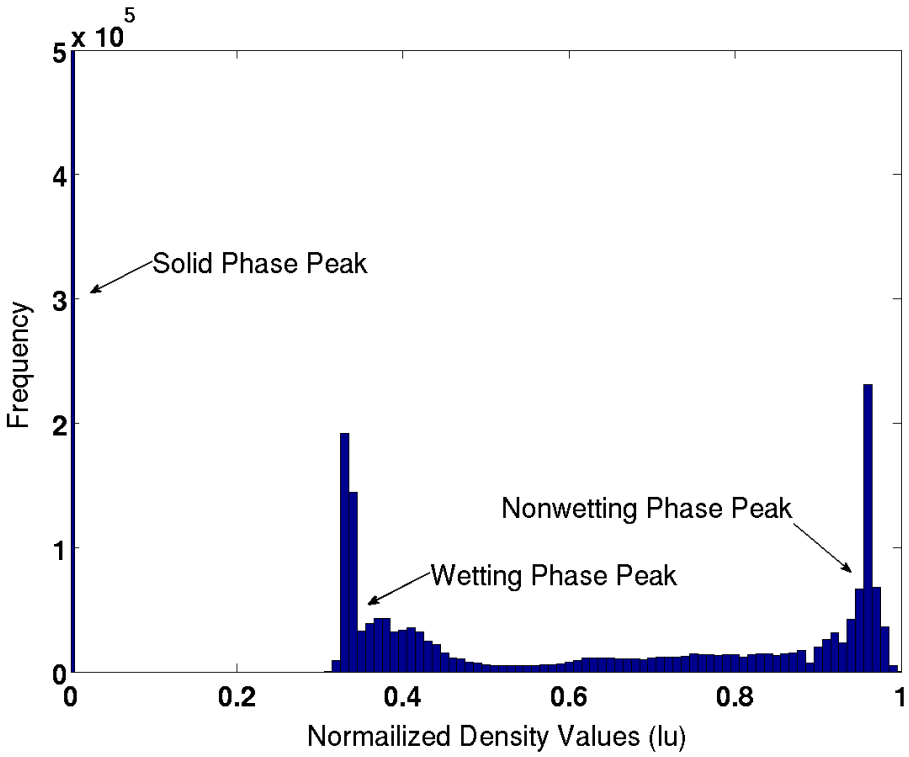

Figure 5.2: Example of a typical histogram of the total density for an LB simulation. The arrows indicate the phases that each peak represents.

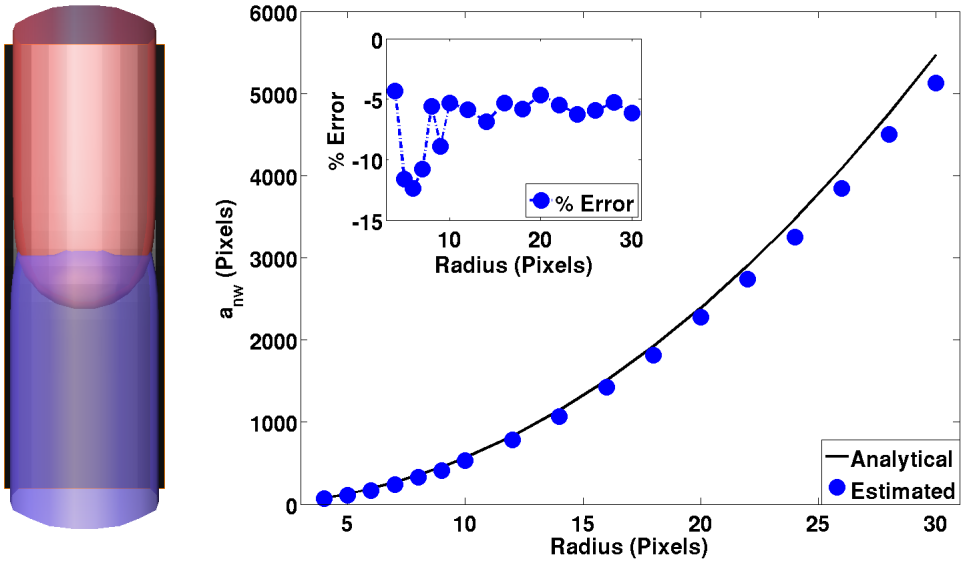

Figure 5.3: On the left is an example of the isosurface obtained for the fluid phases in capillary tube that has a radius of 5 pixels. On the right is the estimated areas of spherical caps in a capillary tube are compared to the analytical solution and plotted as function of the radius. The relative error (top left inset) indicates that overall errors are within 12.5 % with a mean error of approximately 7 %. The negative errors indicate that the estimate is lower than the analytical solution.

used to analyze the LB data most likely under estimated the interfacial are per volume for the porous medium. This is likely due to a lack of accuracy in the wetting phase interfacial area near the three phase contact line. McClure et al. [2007] recently proposed a porous media marching cubes (PMMC) which improves the accuracy of the marching cubes algorithm near the three phase contact line. Additional information pertaining to image processing applied to estimating interfacial area in porous media may be found in Porter and Wildenschild [2008].

5.6 Results and Discussion

5.6.1 Equilibrium Validation

In the LB simulations it was assumed that equilibrium was obtained when the change in capillary pressure (for the flux simulations) and the change in saturation (for the pressure simulations) over time became negligible. Thus, the change in P_c and the change in S for the last

$10,000$ ($\Delta P_c^{10,000}$ and $\Delta S_w^{10,000}$) iterations was estimated for all simulations. The values for $\Delta P_c^{10,000}$ ranged from $0 - 0.25\,Pa$ for all simulations. These values represent less than 1 % change in P_c near the end of these simulations. The values for $\Delta S_w^{10,000}$ ranged from 0-0.00012. Based on this analysis it was assumed that the simulations had reached equilibrium.

5.6.2 Capillary Pressure - Saturation Curves

$P_c - S$ curves for the experiments and both sets of simulations are presented in Figure 5.4. It is emphasized that the simulations presented here are truly predictive in nature, requiring no parameter optimization. With this in mind, the similarities between the experimental and both simulated drainage curves are promising. The nonwetting phase entry pressure is slightly lower in both simulations than in the experiments. In contrast, Schaap et al. [2007] reported a better entry pressure correspondence between simulated drainage and main the drainage experimental curves. One possible explanation for this is that $G_c = 0.025$ in these simulations, whereas Schaap et al. [2007] used a value of $G_c = 0.02$, thus the contact angle was slightly different in the two studies. Additionally, the simulations presented by Schaap et al. [2007] were conducted on a porous medium with the same resolution as the experiments whereas in this study the resolution was decrease by a factor of two. In the study conducted by Pan et al. [2004] the simulated nonwetting phase entry pressures were also slightly lower than the experimental values. Thus, it appears that the SC type model tends to slightly under predict the nonwetting phase entry pressure.

For the flux simulations, numerical instabilities were encountered at higher capillary pressure values, thus it was not possible to simulate the full drainage curve. The instability is likely due to a combination of factors including the choice of LB parameters, the lattice resolution and the compressibility of the fluids at the higher capillary pressures. Schaap et al. [2007] used similar LB parameters in similar simulations without encountering numerical instabilities. In the simulations presented here the lattice resolution was changed from $17\,\mu m$ to $34\,\mu m$ by rebinning the porous medium data. According to Eq. 5.5 the rebinning step reduces the magnitude of the capillary pressure that can be simulated by a factor of 2. Thus, it is likely the instabilities encountered here could be avoided with a different choice of LB parameters at the expense of preserving phase separation.

The simulated imbibition curves are different than the experimental imbibition curves at low saturations, but are in excellent agreement at higher saturations. In the flux simulations the imbibition curve is initially a scanning curve, thus it was not expected to match the main imbibition curve from the experiments at low saturations. It is encouraging that the scanning curve behaves as expected and returns to the main imbibition curve at higher saturations. The pressure imbibition simulation was a primary imbibition curve. This curve unexpectedly

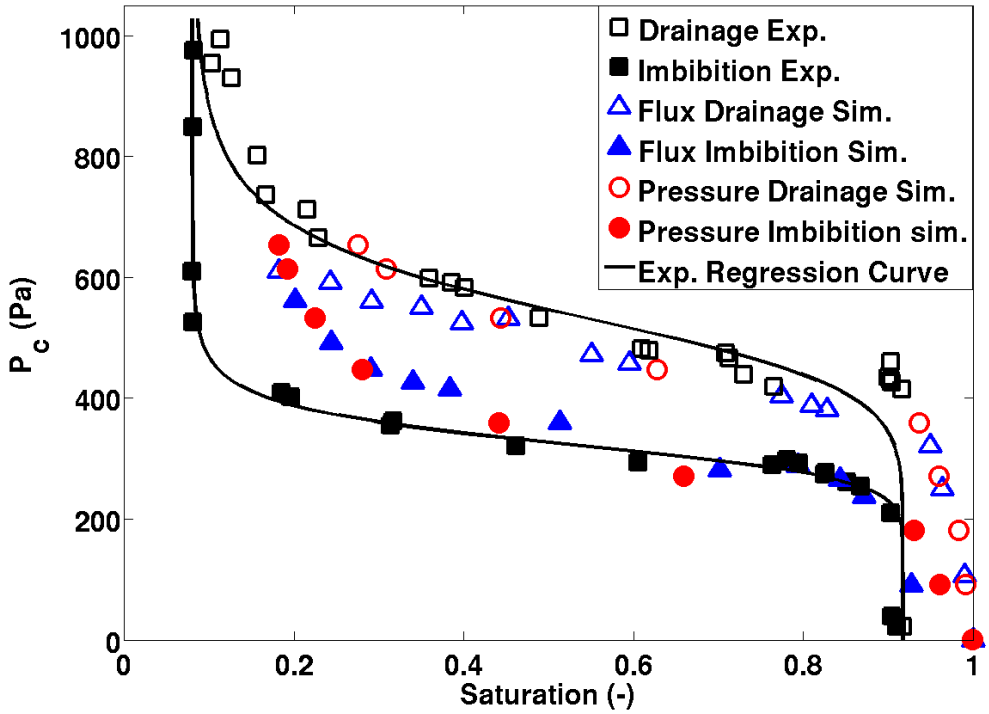

Figure 5.4: Comparison of the $P_c - S$ curves obtained from the experiments and LB simulations.

matches the scanning curve of the flux simulations extremely well and not the experimental imbibition curve. Schaap et al. [2007] showed good agreement at low saturations between LB simulations and the same experiments. One possible explanation for the current discrepancies is that the coarsening of the lattice in the rebinning step changed the geometry of the porous medium such that the smallest pores and throats became smaller and/or removed from the system leaving less space in which the wetting phase pendular rings could reside. Additionally, the flux imbibition simulations predicted trapped nonwetting phase similar to that observed in the experiments, whereas the pressure simulations predict no nonwetting phase entrapment.

5.6.3 Saturation Profiles

Figure 5.5 shows the wetting phase saturation as function of depth for equilibrium points during drainage (top row) and imbibition (bottom row) for the experiments (left column), flux

simulations (middle column) and pressure simulations (right column). In all of the simulation profiles there are large saturation gradients near the inlet (0 mm) and outlet (5 mm) of the column. At the inlet, the saturation gradient is most likely a result of the nonwetting phase boundary, which causes nonwetting phase to enter every pore. At the outlet, the presence of the filter prevents nonwetting phase to enter pores that it would normally enter if the filter was removed. Since these saturation gradients are an artifact of the boundaries and not characteristic of a capillary dominated porous system, the fluid configurations in these regions were not considered in the analysis of the $P_c - S$ and $a_{nw} - S$ curves. The horizontal lines indicate the regions near the inlet and outlet that were excluded from subsequent analysis.

The trends observed in the drainage experiments (see Figure 5.5, A) are similar to those observed in the drainage simulations, suggesting that during drainage the flow processes and model conditions were similar to those in the experiments. At a depth of approximately $1.5\,mm$ and $4\,mm$ large saturation gradients occur in all three systems. The porosity profile (not shown here) indicates a sharp transition from high to low porosity at similar depths. This suggests that the pore size distribution at these depths are controlling factors in the invasion of the nonwetting phase fluid. It is likely that very few large pores are present at these depths and that a larger capillary pressure is required for significant invasion of nonwetting fluid. Pyrak-Nolte et al. [In Press] observed large saturation gradients in 2D micromodel experiments and argued that saturation gradients are a fundamental property of imbibition and drainage processes in which the porous medium is connected to fluid reservoirs at the inlet and outlet. A similar argument could explain the gradients in the profiles presented here, however, homogeneous saturation profiles are observed late in the drainage process at high capillary pressures. Due to the lack of homogeneous saturations throughout the column the assigned average saturation values are not representative of the entire column and may have implications when interpreting the $P_c - S$ and $a_{nw} - S$ results.

During imbibition (see Figure 5.5, B) the saturation profiles for the experiments are noticeably different than those obtained in the LB simulations. The experimental results indicate that saturation gradients occur at approximately the same depths during drainage, whereas the simulation results show relatively uniform saturation profiles for each point on the imbibition curve. This suggests that during imbibition the LB model is simulating different flow processes that were either not present during the experiments or not resolved with a resolution of $17\,\mu m$ in the CMT data. One such flow phenomena could be film flow, which was not resolved in the experiments. If indeed film flow occurred in the LB imbibition simulations this would greatly overestimate that contribution of flow since the resolution in the simulations is $34\,\mu m$. Another possibility for the discrepancy between the saturation profiles is that the imposed boundaries are causing the uniform profiles in the simulations, which is not the case in the observed data since only a section of the column was imaged.

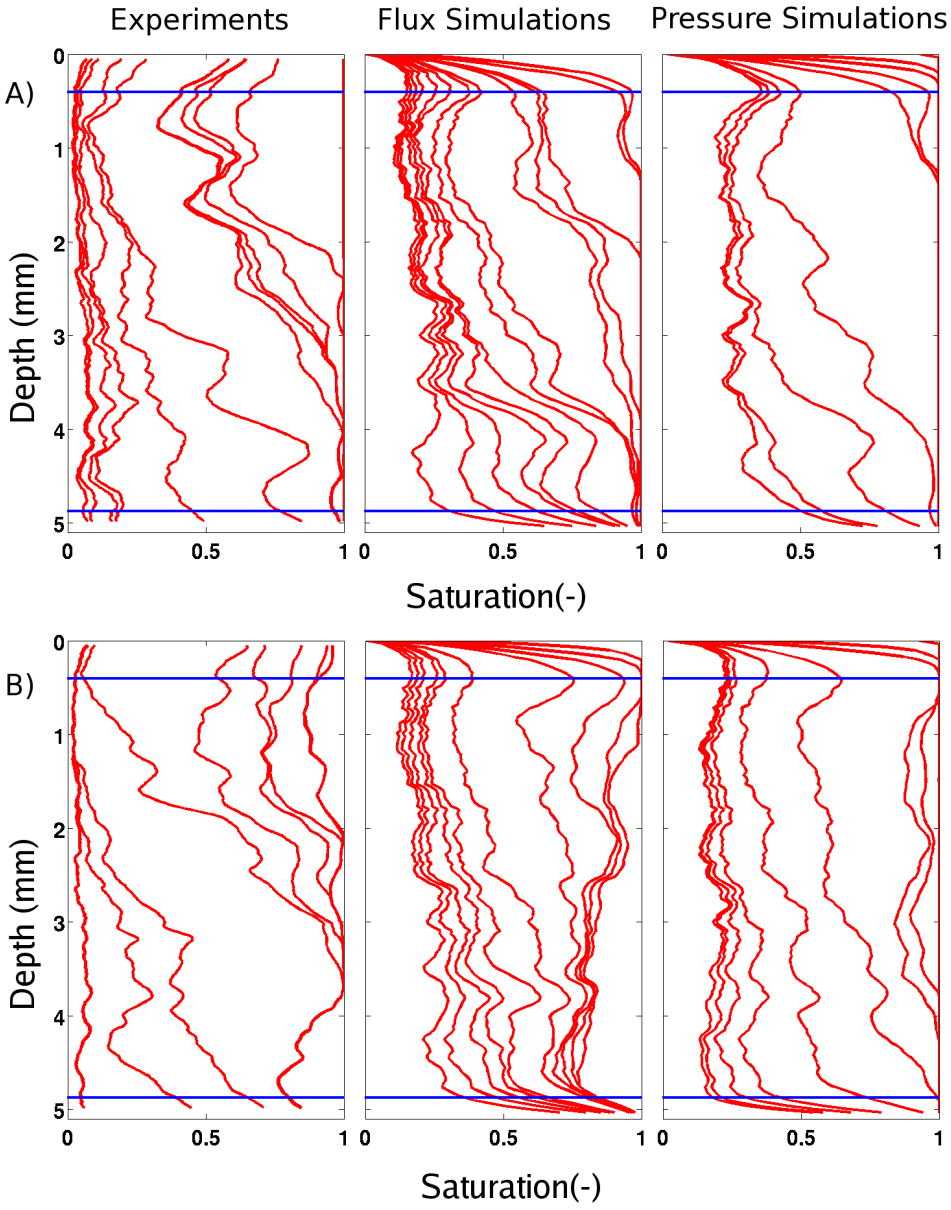

Figure 5.5: Saturation profiles for drainage (A) and imbibition (B) for the experiments (left), flux simulations (middle) and pressure simulations (right). The horizontal lines indicate unphysical saturation gradients that arise in the simulations due to the boundary conditions. Subsequent analysis is performed on data between the horizontal lines to minimize the effects of the boundary conditions.

5.6.4 Phase Distributions

To further investigate the nature of the flow processes and fluid distributions in the experiments and LB simulations, Figure 5.6 and 5.7 compare vertical cross sections of the fluid distributions for various saturations on the drainage and imbibition curves. It is noted that these cross sections are for the full imaged and full simulated volumes, thus the saturations are slightly different than those presented in the $P_c - S$ and $a_{nw} - S$ curves since smaller cubes were analyzed for those curves. The saturations in each column were matched as closely as possible, but in some cases a near match was not possible because the simulations were not controlled for saturation. Figure 5.6 indicates that, qualitatively, the fluid distributions are in very good agreement between all three systems. This result is somewhat unexpected since the boundary conditions in each system are different. Additionally, the fluid-fluid and fluid-solid interactions in the LB model were incorporated phenomenologically, however they seem to capture the overall pattern of the fluid phases at equilibrium. These results suggest that during primary drainage the pore geometry is the controlling factor in the final-fluid distribution for a given equilibrium point. During imbibition, see Figure 5.7, it is evident that the fluid distributions do not agree well, especially at higher saturations. There is a large nonwetting phase blob in the upper right hand corner of the images for all saturation values for imbibition, whereas, in the imbibition simulations this nonwetting phase blob is not present because of the location of the boundary in the simulation. It is likely that the nonwetting phase near the top of the imaged section is disconnected (since the column is longer than the imaged section) and immobile, whereas in the simulations, the nonwetting phase near the inlet is connected to the inlet boundary and moves out of the pores as wetting phase enters the system. This suggests that immobile nonwetting phase plays a significant role in the imbibition processes presented in this study.

5.6.5 Interfacial Area - Saturation Curves

Interfacial area per volume for the nonwetting-wetting interface (a_{nw}) is presented in Figure 5.8. Drainage and imbibition are represented by the open and solid symbols, respectively. There is very good agreement between the experimental drainage data and both drainage simulations. The simulated imbibition curves, on the other hand, predict considerably more a_{nw} for a given saturation than the experimental imbibition data. Additionally, the experimental and simulated imbibition and drainage curves are opposite in relation to each other; the experimental imbibition curves are lower than the experimental drainage curves, whereas the simulated imbibition curves are higher than the simulated drainage curve. Culligan et al. [2004, 2006] argued that a_{nw} should be lower during imbibition than in drainage based on consideration of a simple

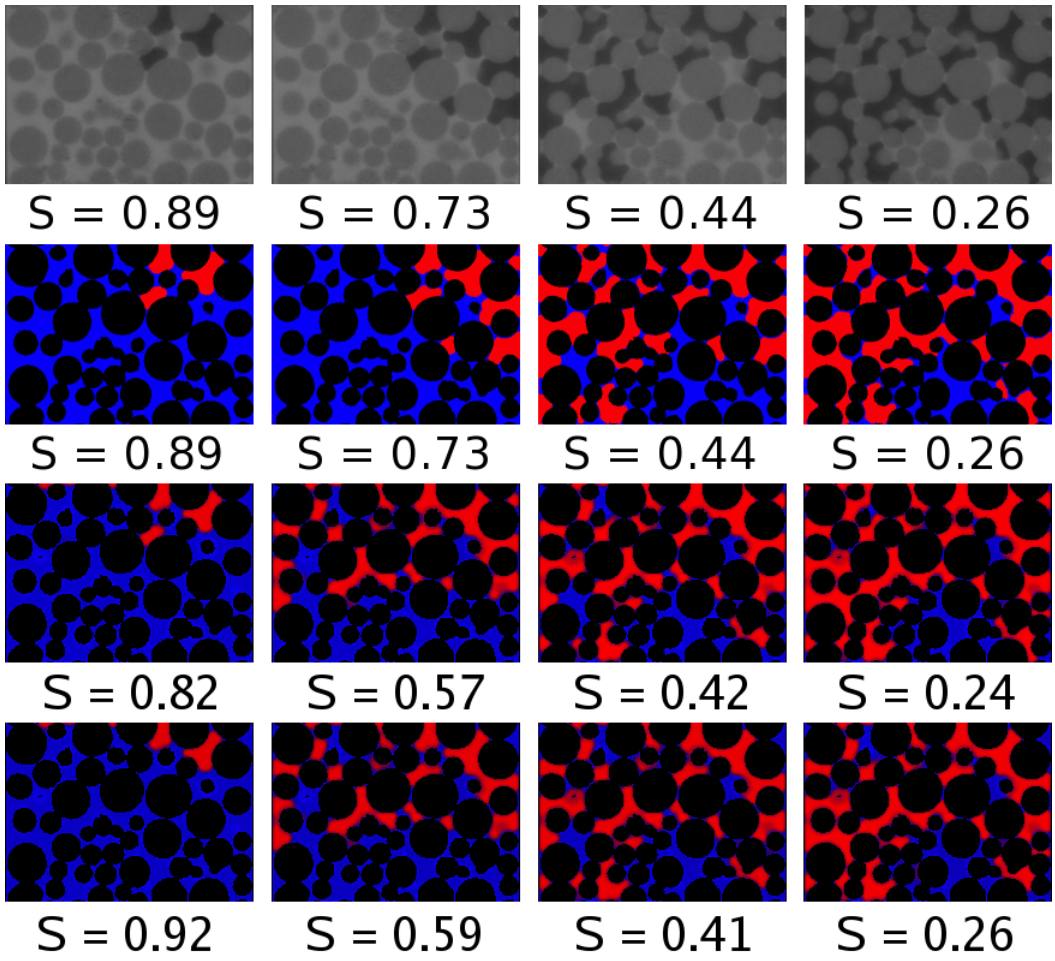

Figure 5.6: Comparison between fluid distributions of the gray-scale experimental data (1^{st} row), segmented data (2^{nd} row), flux simulations (3^{rd} row) and pressure simulations (4^{th} row) at various saturations during drainage for a vertical cross section where red and blue are the nonwetting and wetting fluids, respectively.

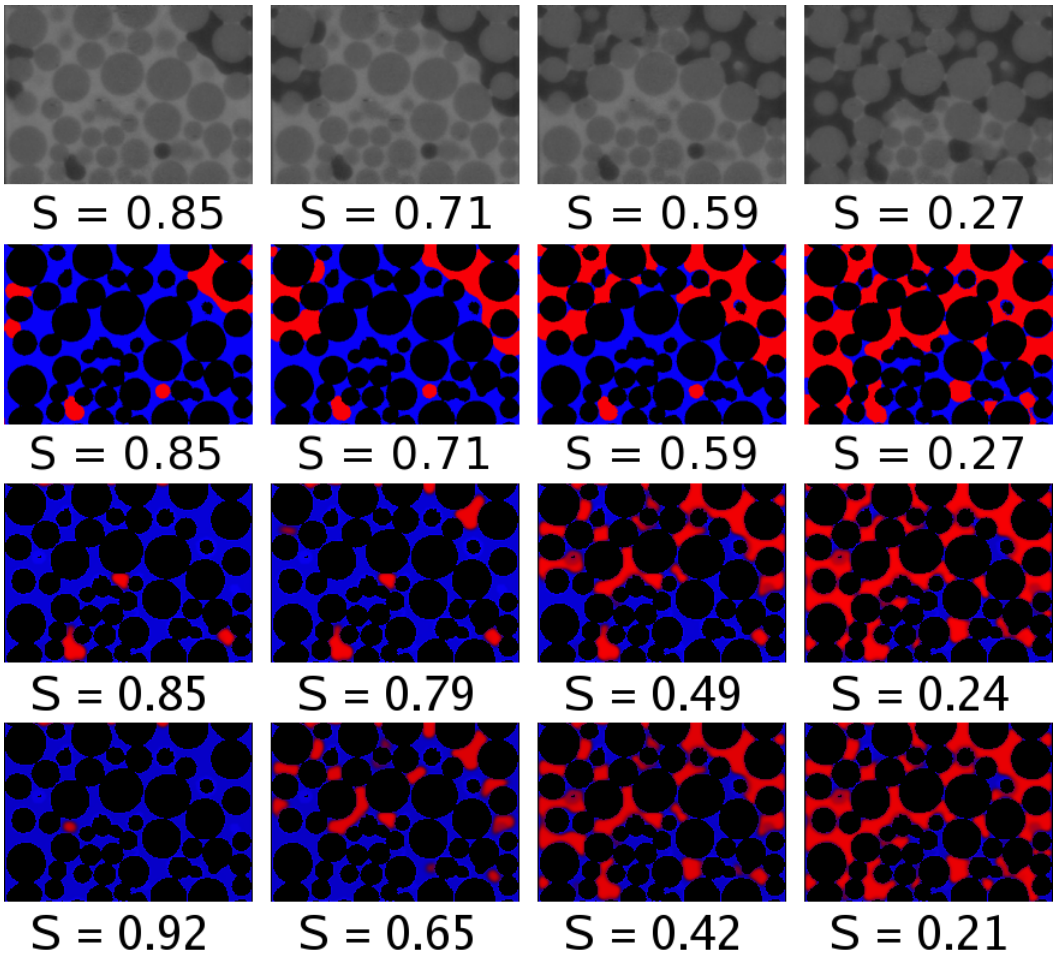

Figure 5.7: Comparison between fluid distributions of the gray-scale experimental data (1^{st} row), segmented data (2^{nd} row), flux simulations (3^{rd} row) and pressure simulations (4^{th} row) at various saturations during imbibition for a vertical cross section where red and blue are the nonwetting and wetting fluids, respectively.

capillary tube, in which, during imbibition the nonwetting-wetting phase meniscus would flatten leading to smaller a_{nw} values, whereas during drainage the meniscus would stretch leading to larger a_{nw} values. This argument seems to apply to situations in which equilibrium has not been achieved since Laplace's law would predict the same a_{nw} irrespective of the direction of flow prior to reaching equilibrium and assuming identical contact angles. It is also noted that this explanation does not account for the existence of disconnected phases, which may play a significant role. Brusseau et al. [2007] presented $a_{nw} - S$ curves for drainage and imbibition estimated from CMT image data, which are similar to the experimental estimates presented here. Their imbibition curve also lies below the drainage curve, but they provide no explanation as to why a_{nw} is lower during imbibition than in drainage. The LB modeling results are consistent with LB results presented by McClure et al. [2004] and network modeling results presented by Held and Celia [2001] and Joekar-Niasar et al. [2007], in that these numerical investigations predicted higher a_{nw} during main imbibition than in primary drainage. Reeves and Celia [1996], on the other hand, reported a_{nw} values that cross during primary drainage and main imbibition. In these numerical investigations no conclusive argument was presented as to why imbibition $a_{nw} - S$ were higher than drainage a_{nw}.

In the comparison presented in this study it appears that the discrepancies in the $a_{nw} - S$ curves during imbibition are, to some degree, caused by the existence of trapped nonwetting phase in the experiments near the top of the imaged section, which is not present in the simulations. This is evident in cross section images presented in Figure 5.7. Additionally, the relatively uniform simulated imbibition saturation profiles suggest that a significant amount of wetting phase is capable of invading pores throughout the entire length of the domain at all instances during imbibition. This could be caused by the presence of the nonwetting phase boundary in the simulations that does not exist in the experiments. Additionally, this could be an artifact of the LB model since the model is slightly compressible, allows for a small amount of diffusion, and in these simulations, simplify assumptions have been made about gravity and the dynamic viscosity ratio, however, we do not currently have an explanation as to why these artifacts would be more pronounced during imbibition than in drainage.

5.7 Summary and Conclusions

In this study an LB model was used to simulate experimentally measured $P_c - S$ curves and estimate interfacial area per volume for the nonwetting-wetting interface (a_{nw}) from the resulting data. Using CMT image data, the porous medium from the experiments was used as input to the LB model, resulting in the same pore geometry in both systems. The lattice was coarsened such that the full experimental domain could be simulated and two different types of simulations were developed and compared to the experimental data. One type of simulations

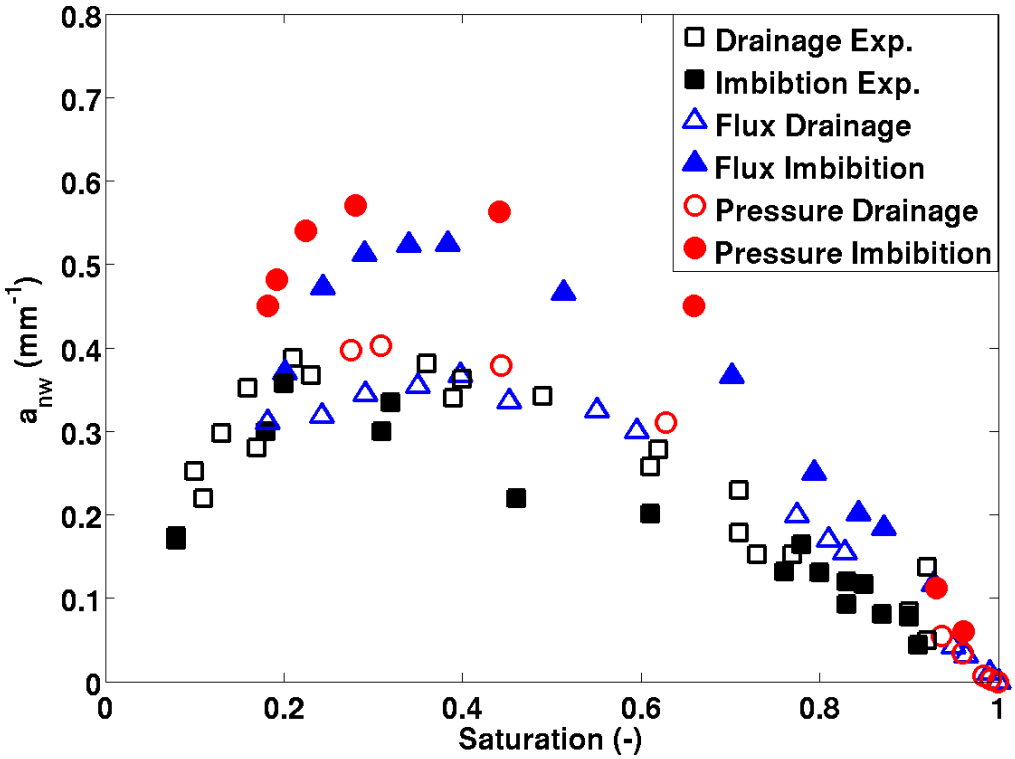

Figure 5.8: Comparison of the $a_{nw} - S$ curves obtained from the experiments and LB simulations. The open symbols represent drainage, whereas the filled symbols represent imbibition

consisted of multiple drainage and imbibition steps performed in succession. These simulations matched the experimental procedure as closely as possible and employed flux boundary conditions at the inlet and outlet. The other type of simulations consisted of multiple single step drainage and imbibition events starting from a fully saturated or fully drained porous medium. In these simulations constant pressure boundary conditions were employed.

A comparison between the experimental and simulated $P_c - S$ curves indicated that the simulated drainage curve was in good agreement with the experimental observations. However, for the flux simulations numerical instabilities were encountered at higher capillary pressure values, resulting in an incomplete drainage curve. Neither of the simulated imbibition curves matched the experiments at low saturations, but tended to agree at higher saturations. The flux imbibition curve was a scanning curve, thus it was not expected to agree with the observed data at low saturations. At higher saturations the comparison indicates that the scanning curve returned to the main imbibition curve as expected. The pressure imbibition curve was a primary imbibition curve which resulted in substantially more residual wetting phase than was observed in the experiments. Additionally, the flux simulations predicted the trapped nonwetting phase that was observed in the experiments, whereas the pressure simulations predicted no trapped nonwetting phase.

A comparison of the saturation profiles and cross sections of the fluid distributions within pores showed good agreement during drainage and some discrepancies during imbibition. The drainage saturation profiles exhibited large saturation gradients at approximately the same depths for the experimental and simulated systems. The cross sections for drainage showed remarkable correspondence between all three systems. During imbibition the experimental system exhibited large saturation gradients, whereas the simulations exhibited relatively uniform saturation profiles. The cross section images for imbibition showed that there was a significant amount of nonwetting phase in the upper portion of the porous medium for the experimental system, whereas in the simulations the nonwetting phase was able to flow out of the upper portion of the porous media since it was connected to the nonwetting phase boundary.

The comparison between $a_{nw} - S$ curves showed very good agreement for drainage, however, the imbibition curves were significantly higher in the simulations than in the experiments. Furthermore, the position of the imbibition curves relative to the drainage curves were opposite in the simulations than in the experiments. We argue that this discrepancy is in part due to disconnected phase present in the experiments near the top of the imaged section, which was not present in the simulations since the nonwetting phase was connected to the nonwetting phase boundary and thus mobile. A review of the literature suggests that experimental results generally show $a_{nw} - S$ curves with imbibition lower than drainage, whereas numerical and theoretical predictions show $a_{nw} - S$ curves with imbibition greater than drainage, however we only found a few studies that addressed this topic. Thus, there is a need for further investigation

(experimental, theoretical and numerical) and conceptual understanding of the evolution of interfacial area as a function of saturation during imbibition and drainage.

We have made no attempt to investigate the uniqueness of the $P_c - S - a_{nw}$ relationship proposed by Hassanizadeh and Gray [1990] due to the sparse number of data points and lack of scanning curve simulations and observations. However, based on this study, it appears that $a_{nw} - S$ provides insights into the nature of flow in porous media that is not obtained through the $P_c - S$ relationship alone.

Current research is focused on the improvement of the simulations especially during imbibition. Simulations conducted at the original resolution 414x414x300, as opposed to 207x270x150, may help explain some of the discrepancies in the LB simulations encountered during imbibition. Additionally, simulations of scanning curves are currently underway to fully investigate the uniqueness of the $P_c - S - a_{nw}$ relationship. Scanning curves were not conducted for this study due to computational expenses. Improvements in the efficiency of the code will likely allow for faster simulations, including a series of simulations conducted on the full volume at the observed resolution.

5.8 Acknowledgments

Porter and Wildenschild were supported, in part, by NSF-EAR-06101108 and NSF-EAR-0337711. Schaap was supported, in part, by NSF-EAR-0337378 and NSF-EAR-061003. A portion of this work was conducted at GeoSoilEnviroCARS (Sector 13), Advanced Photon Source (APS), Argonne National Laboratory. GeoSoilEnviroCARS is supported by the National Science Foundation - Earth Sciences (EAR-0622171) and Department of Energy - Geosciences (DE-FG02-94ER14466). Use of the Advanced Photon Source was supported by the U. S. Department of Energy, Office of Science, Office of Basic Energy Sciences, under Contract No. DE-AC02-06CH11357.

Chapter 6. Discussion and Conclusions

6.1 Summary

The research presented in this dissertation has focused on improving the understanding of multiphase flow and transport in porous media, with the goal of providing experimental observations and numerical simulations that can serve as a guide in the development of more robust macro-scale multiphase flow simulators. The analysis of 3-dimensional high resolution CMT images and LB simulations of drainage and imbibition experiments has enabled us to investigate the dependence of capillary pressure on saturation and fluid-fluid interfacial area per volume. Specifically, the objectives of this research were to:

1. Develop and thoroughly validate an image analysis technique that may be used to estimate properties such as phase distributions (i.e., porosity and saturation) and interfacial area from CMT image data.

2. Collect 3D CMT image data for NAPL-water-glass bead drainage and imbibition experiments.

3. Investigate the relationship between capillary pressure, saturation and interfacial area per volume by comparing experimental results with empirical relationships reported in the literature.

4. Develop new LB drainage and imbibition simulations of air-water experiments and compare results directly to the experimental system with an emphasis on the relationship between capillary pressure, saturation and interfacial area.

In Chapter 3 the image analysis algorithm used to estimate interfacial area from CMT data was discussed, which involved three main steps. First, the images were filtered with an anisotropic diffusion filter to remove noise in the original gray-scale images. The second step involved segmenting the filtered data with a k-means cluster analysis algorithm. Due to relatively smooth phase boundaries between the nonwetting and wetting fluids in the original gray-scale images, the k-means algorithm was not capable of segmenting the three phase data, and therefore knowledge of the solid phase, obtained from a dry image, was required to separate the nonwetting and solid phases. The resulting trinary data set was used to estimate porosity and saturation values. The third image analysis step involved constructing isosurfaces from

which interfacial area was estimated. The isosurfaces were constructed in Amira^{TM}, which uses a generalized marching cubes algorithm. The image analysis technique developed for this research was successfully validated by estimating porosity and interfacial area for two simple data sets and comparing the results to laboratory measurements and other image analysis methods commonly used in the literature.

Chapter 4 focused on the analysis and interpretation of imbibition and drainage experiments conducted at the GSECARS beam-line at the Advanced Photon source (APS), Argonne National Laboratory. Fluid-fluid interfacial area estimates were derived from CMT images of the quasi-static fluid configurations of each point on the $P_c - S$ curves. It was demonstrated that CMT imaging is a powerful, nondestructive tool for quantifying porosity, saturation and interfacial area per volume. CMT imaging is especially useful in quantifying the different components of interfacial area and it was shown that the trends observed in the measured data were in agreement with data presented in the literature. Furthermore, the $P_c - S$ curves were used to predict interfacial area using a recently proposed interfacial area model.

The development of lattice-Boltzmann simulations for air-water drainage and imbibition experiments was the focus of Chapter 5. The porous medium for the LB simulations was defined using the CMT image data from previous air-water experiments [Culligan et al., 2004], allowing for the direct comparison of fluid configurations within the pores. Two sets of LB simulations were developed to investigate differences in boundary conditions and flow history on the resulting $P_c - S$ and $a_{nw} - S$ curves. Simulated fluid distributions within the pores were compared to the fluid distribution in the experiments showing similarities that were beyond our expectations. Furthermore, the experimental and simulated $P_c - S$ and $a_{nw} - S$ curves were compared with favorable results.

Collectively, the results show that there is a functional relationship between the fluid-fluid IFA and saturation. Furthermore, it was shown that the various IFA components, a_{total}, a_{film}, a_{nw} and a_{eff}, as defined in this manuscript show significantly different trends as a function of saturation. A complex functional $P_c - S - a_{nw}$ relationship was also shown to exist, although its uniqueness was not investigated. The inclusion of a_{nw}, in addition to S, into the functional dependence of P_c at the macro-scale provides information about the state of the system, which is not elucidated from the $P_c - S$ curves alone, suggesting that the traditional macro-scale $P_c - S$ curves do not sufficiently describe the physics of a multiphase porous system.

6.2 Notable Findings

Validation of the image analysis method developed in this research showed that the method obtained estimates that were in agreement with laboratory measurements and other commonly used image analysis methods. Specifically, it was shown that:

- Both k-means and indicator kriging segmentation algorithms produced essentially identical volume averaged porosity estimates that were in excellent agreement with laboratory measurements.
- Marching cubes based interfacial area estimates for simple 2-phase and 3-phase data sets provided consistent interfacial area estimates that were 1-20 % of laboratory estimates, whereas voxel counting and 2-point correlation functions overestimated interfacial area by 20-45 %.
- In both the 2-phase and 3-phase data, an increase in resolution by a factor of two (or more) did not show significant improvements in the resulting quantities of interest. This is of importance since the size of the data set and the computational cost associated with processing the data increased by a factor of eight.

Analysis and interpretation of CMT image data of drainage and imbibition experiments showed fluid-fluid interfacial area can be divided into components associated with different flow processes, which is of importance when: (1) investigating the functional $P_c - S - a_{nw}$ relationship, and (2) considering mass transfer processes that are controlled by fluid-fluid interfaces. Most importantly, with this data set it was shown that:

- To the best of our knowledge, the experimental $P_c - S - a_{nw}$ data set is only the third of its kind reported in the literature and an improvement to the oil-water data set reported by Culligan et al. [2006]. It was shown that the trends in $a_{nw} - S$ observed in this data set for drainage and imbibition contradict typical pore-scale modeling results, thus new experimental observations are required to further validate these results, as well as validate pore-scale numerical models.
- Knowledge of interfacial area provides information about the state of the fluids and system that can not be obtained by the $P_c - S$ curve alone. For example, the $P_c - S$ curves presented in this dissertation show that flow processes were virtually identical for imbibition, whereas differences in the $a_{nw} - S$ curves for imbibition suggest that the flow processes were different.
- $P_c - S$ and porosity data was input into the explicit IFA model [Grant and Gerhard, 2007a], which successfully predicted the measured effective interfacial area per volume. This result is particularly significant since (1) the data set was used to validate the only macro-scale model available for this type of prediction, and (2) the $P_c - S$ data used in the model corresponded to the entire column whereas the measured interfacial area data corresponded to a subvolume of the column, demonstrating that the concept of an REV was sufficient to compare two different volumes of porous media.

Lattice-Boltzmann simulations of air-water drainage and imbibition experiments demonstrated that the method is capable of predicting experimental $P_c - S$ curves well. Additionally, it was shown that there was very little difference between the two sets of simulations (flux and pressure boundary conditions) despite the differences in boundary conditions and flow histories. Notable findings include the following:

- The LB simulations presented in this dissertation are unique in that they are the first simulations conducted on the exact same geometry of the pore space in which the experiments were conducted, and the lattice spanned the entire imaged section of the experiments.
- The comparison of experimental and simulated phase distributions within the pores is, to the best of our knowledge, the only comparison of its kind found in the literature. The comparison during drainage showed excellent agreement between both simulations and the experiments. During imbibition it is likely that the location of the boundaries in the simulations influenced the phase distributions, whereas in the experiments nonwetting phase most likely became disconnected since the experimental column was much longer than the imaged section.
- The $P_c - S$ curves were in good agreement with the experimental observations. Additionally, simulated $a_{nw} - S$ curves were very similar to those observed. However, the simulated imbibition $a_{nw} - S$ curves were higher than the simulated drainage $a_{nw} - S$ curves. This is contradictory to the experimental system in which the drainage $a_{nw} - S$ curves were higher than the imbibition drainage curves. These results suggest that simplifying assumptions and differences in boundary conditions defined in the LB simulations influence the flow processes, however these differences in flow processes are not evident in the traditional $P_c - S$ curves.

6.3 Future Directions

Based on the literature review discussed here, the research that motivated this study, and the results presented in this dissertation, it is apparent that there are many open questions that still need to be addressed in the realm of multiphase flow and transport in porous media. It has been demonstrated that CMT imaging of multiphase flow experiments combined with pore-scale modeling using the lattice-Boltzmann technique is a powerful research tool, capable of leading the scientific community to a better understanding of the essential physics required to develop more robust macro-scale models. Recommendations for future study that are extensions of this research and could provide further insights into the physics of multiphase flow in porous media include the following:

- Conduct new experiments for numerous unconsolidated materials with the goal of characterizing $P_c - S - a_{nw}$ for the entire column. It was shown in this research that increasing the resolution was not beneficial for coarse grained material, thus some of these experiments could work toward imaging larger porous systems at lower resolutions. In some of these experiments imaging the entire column would be especially beneficial since one could then investigate the role of connectivity of the fluid phases on the flow processes. With these experiments one could relate the externally measured capillary pressure to an average saturation value associated with the connected phase rather than an average saturation value associated with both the connected and disconnected phase.

- Measure main drainage and imbibition $P_c - S$ curves, followed by multiple imbibition and drainage scanning curves in order to generate a $P_c - S - a_{nw}$ surface. To date there are no 3D experimental results that have investigated the uniqueness of the $P_c - S - a_{nw}$ relationship.

- Develop LB simulations, or other pore-scale numerical simulations, of drainage and imbibition that do not require simplifying assumptions about the fluid properties, or flow processes, and compare them to experiments, especially $a_{nw} - S$ curves, for which the pore geometry can be defined in detail. Numerous researchers have shown that pore-scale modeling techniques, based on simplifying assumptions, are capable of simulating $P_c - S$ curves, however the results presented in Chapter 5, and references therein, indicate that the models predict higher interfacial areas during imbibition than observed in experimental systems. Currently, there is not enough experimental data that addresses this issue, and the majority of pore-scale modeling efforts do not adequately validate their results with experimental observations.

- Investigate fluid configurations at irreducible wetting phase saturation and residual nonwetting phase saturation. The interfacial area comparison with the explicit IFA model indicated that these situations were the least accurately predicted.

Bibliography

Al-Raoush, R. I. and C. S. Wilson (2005a), Extraction of physically realistic pore network properties from three-dimensional synchrotron x-ray microtomography images of unconsolidated porous media systems, *J. Hydrol.*, 300:44–64, doi: 10.1016/j.jconhyd.2004.12.001.

Al-Raoush, R. I. and C. S. Wilson (2005b), A pore-scale investigation of a multiphase porous media system, *J. Cont. Hydrol.*, 77:67–89, doi: 10.1016/j.jhydrol.2004.05.005.

Altman, S. J., W. J. Peplinski and M. L. Rivers (2005), Evaluation of synchrotron x-ray computerized microtomography for the visualization of transport processes in low-porosity materials, *J. Contam. Hydrol.*, 78:167–183, doi: 10.1016/j/jconhyd.2005.05.004.

Anderson, W. G. (1987), Effects of wettability on capillary pressure, *J. Pet. Technol.*, 4:1283–1299.

Annable, M., J. J. P. R. D. Dai, H. Kim and A.L.Wood (1998), Field evaluation of interfacial and partitioning tracers for characterization of effective napl-water contact areas., *Ground Water*, 36(3):495–503.

Anwar, A., M. Bettahar and U. Matsubayashi (2000), A method for determining air-water interfacial area in variably saturated porous media., *J. Contam. Hydrol.*, 43:129–146.

Arns, C., M. Knackstedt and K. Mecke (2003), Reconstructing complex materials via effective grain shapes, *Phys. Rev. Lett.*, 91(21).

Bear, J. (1988), *Dynamics of Fluids in Porous Media*, Dover Publications, Inc.

Bedient, P. B., H. S. Rifai and C. J. Newell (1997), *Ground Water Contamination Transport and Remediation*, Prentice Hall, second edition.

Bekri, S. and P. Alder (2001), Dispersion in multiphase flow in porous media, *Int. J. Multiphase Flow*, 28:665–669.

Berkowitz, B. and D. P. Hansen (2001), A numerical study of the distribution of water in partially saturated porous rock, *Trans. Porous Media*, 45:303–319.

Berryman, J. (1985), Measurement of spatial correlation functions using image processing techniques, *J. Appl. Phys.*, 57(7):2374–2384.

Betson, M., J. Barker, P. Barnes and T. Atkinson (2005), Use of synchrotron tomographic techniques in the assessment of diffusion parameters for solute transport in groundwater flow, *Trans. Porous Media*, 60:217–223, doi: 10.1007/s11242-004-5737-0.

Blunt, M. J. (2001), Flow in porous media - pore-network models and multiphase flow, *Current Opinion in Colloid & Interface Science*, 6:197–207.

Bradford, S. A. and F. J. Leij (1996), Predicting two- and three-fluid capillary pressure-saturation relationships of porous media with fractional wettability, *Water Resour. Res.*, 32(2):251–259.

Bradford, S. A. and F. J. Leij (1997), Estimating interfacial areas for multi-fluid soil systems, *J. Contam. Hydrol.*, 27:83–105.

Brooks, R. H. and A. T. Corey (1964), Hydraulic properties of porous media, *Hydrology Papers*, colorado State University, Ft. Collins, CO.

Brusseau, M. L., H. Janousek, A. Murao and G. Schnaar (2008), Synchrotron x-ray microtomography and interfacial partitioning tracer test measurements of NAPL-water interfacial area, *Water Resour. Res.*, 44, doi: 10.1029/2006WR2006WR005517.

Brusseau, M. L., S. Peng, G. Schnaar and M. S. Costanza-Robinson (2006), Relationship among air-water interfacial area, capillary pressure and water saturation for a sandy porous medium, *Water Resour. Res.*, 42, doi: 10.1029/2005WR004058.

Brusseau, M. L., S. Peng, G. Schnaar and A. Murao (2007), Measuring air-water interfacial areas with x-ray microtomography and interfacial partitioning tracer tests, *Environ. Sci. Technol.*, 41:1956–1961.

Brusseau, M. L., J. Popovicova and J. Silva (1997), Characterizing gas-water interfacial and bulk-water partitioning for gas- phase transport of organic contaminants in unsaturated porous media, *Environ. Sci. Technol.*, 31:1645–1649.

Bryant, S. L. and A. S. Johnson (2002), *Chemicals in the Environment: Fate, Impacts and Remediation*, chapter Theoretical Evaluation of the Interfacial Area between Two fluids in a model Soil, pages 26–41, ACS Symposium Series 806, American Chemical Society.

Bryant, S. L. and A. S. Johnson (2004), Bulk and film contributions to fluid/fluid interfacial area in granular media, *Chem Eng. Comm.*, 191:1660–1670.

Carlson, W. D. (2006), Three-dimensional imaging of earth and planetary materials, *Earth and Planet. Sci. Lett.*, 249:133–147, doi: 10.1016/j.epsl.2006.06.020.

Charbeneau, R. J. (2000), *Groundwater Hydraulics and Pollutant Transport*, Prentice Hall.

Chen, D., L. J. Pyrak-Nolte, J. Griffin and N. J. Giordano (2007), Measurement of interfacial are per volume for drainage and imbibition, *Water Resour. Res.*, 43, doi: 10.1029/2007WR006021.

Chen, J., J. W. Hopmans and M. E. Grismer (1999), Parameter estimation of two-fluid capillary pressure-saturation and permeability functions, *Adv. Water Resour.*, 22(5):479–493.

Chen, L. and C. Kibbey (2006), Measurement of air-water interfacial area for multiple hysteretic drainage curves in an unsaturated fine sand, *Langmuir*, 22(16):6874–6880.

Chen, S. and G. Doolen (1998), Lattice-boltzmann method for fluid flows, *Annual Rev. Fluid Mech.*, 30:329–364.

Chen, Z., G. Huan and Y. Ma (2006), *Computational Methods for Multiphase Flow in Porous Media*, Society of Industrial and Applied Mathematics.

Cheng, J.-T., L. J. Pyrak-Nolte, D. D. Nolte and N. J. Giordano (2004), Linking pressure and saturation through interfacial areas in porous media, *Geophys. Res. Lett.*, 31.

Clausnitzer, V. and J. W. Hopmans (1999), Determination of phase-volume fractions from tomographic measurements in two-phase systems, *Adv. Water Resour.*, (22):577–584.

Clausnitzer, V. and J. W. Hopmans (2000), Pore-scale measurements of solute breakthrough using microfocus x-ray computed tomography, *Water Resour. Res.*, 36(8):2067–2079.

Coles, M. E., R. D. Hazlett, P. Spanne, W. E. Soll, E. L. Muegge and K. W. Jones (1998), Pore level imaging of fluid transport using synchrotron x-ray microtomography, *J. Pet. Sci. Eng.*, 19:55–63.

Corey, A. T. (1986), *Mechanics of Immiscible Fluids in Porous Media*, Water Resources Publications, Littleton, Colorado, second edition.

Costanza-Robinson, M. S. and M. L. Brusseau (2002), Air-water interfacial areas in unsaturated soils: Evaluation of interfacial domains, *Water Resour. Res.*, 38(10).

Costanza-Robinson, M. S., K. H. Harrold and R. M. Lieb-Lappen (2008), X-ray microtomography determination of air-water interfacial area-water saturation relationships in sandy porous media, *Environ. Sci. Technol.*, accepted.

Culligan, K. A., D. Wildenschild, B. S. Christensen, W. G. Gray and M. L. Rivers (2006), Pore-scale characteristics of multiphase flow in porous media: A comparison of air-water and oil-water experiments, *Adv. Water Resour.*, 29:227–238.

Culligan, K. A., D. Wildenschild, B. S. Christensen, W. G. Gray, M. L. Rivers and A. B. Tompson (2004), Interfacial area measurements for unsaturated flow through porous media, *Water Resour. Res.*, 40, doi: 10.1029/2004WR003278.

Dalla, E., M. Hilpert and C. T. Miller (2002), Computation of the interfacial area for two-fluid porous systems, *J. Contam. Hydrol.*, 56:25–48.

Dane, J. H. and G. C. Topp, editors (2002), *Methods of Soil Analysis Part 4-Physical Methods*, number 5 in SSSA Book Series: 5, Soil Sci. Soc. Amer.

Davidson, J. M., D. R. Nielsen and J. W. Biggar (1966), The dependence of soil water and release upon the applied pressure increment, *Soil Sci. Soc. Amer. Proc.*, 30:298–304.

Demond, A. H., F. N. Desai and K. F. Hayes (1994), Effect of cationic surfactants on organic liquid-water capillary pressure-saturation relationships, *Water Resour. Res.*, 30(2):333–342.

Dobson, R., M. H. Schroth, M. Oostrom and J. Zeyer (2006), Determination of NAPL-water interfacial areas in well-characterized porous media, *Environ. Sci. Technol.*, 40:815–822.

Dullien, F. A. L. (1992), *Porous Media: Fluid Transport and Pore Structure*, Academic Press, second edition.

Dullien, F. A. L., C. Zarcone, I. F. MacDonald, A. Collins and R. D. E. Bochard (1989), The effects of surface roughness on the capillary pressure curves and heights of capillary rise in glass beads, *J. Colloid and Interface Sci.*, 127(2):362–372.

Dumore, J. M. and R. S. Schols (1974), Drainage capillary pressure functions and the influence of connate water, *Soc. Pet Eng. J.*, 14:437–444.

Ferziger, J. H. and M. Perić (2002), *Computational Methods for Fluid Dynamics*, Springer, third edition.

Flannery, B. P., H. W. Deckman, W. G. Roberge and K. L. D'Amico (1989), Three dimensional x-ray microtomography, *Science*, 237:1439–1444.

Flin, F., J.-B. Brzoska, D. Coeurjolly, R. A. Pieritz, B. Lesaffre, C. Coléou, P. Lamboley, O. Teytaud, G. L. Vignoles and J.-F. Delesse (2005), Adaptive estimation of normals and surface area for discrete 3-d objects: Application to snow binary data from x-ray tomography, *IEEE Trans. Image Proc.*, 14(5):585–596.

Fredrich, J. T., A. A. DiGiovanni and D. R. Noble (2006), Predicting macroscopic transport properties using microscopic image data, *J. Geophys. Res.*, 111, doi: 10.1029/2005JB003774.

Frisch, U., B. Hasslacher and Y. Pomeau (1986), Lattice-gas automata for the Navier-Stokes equations, *Phys. Rev. Lett.*, 56:1505–1508.

Gallagher, N. C. and G. L. Wise (1981), A theoretical analysis of the properties of median filters, *IEEE Transactions on Acoustics, speech and Signal Processing*, 29(6):1136–1141.

Gerhard, J. I. and B. H. Kueper (2003), Capillary pressure characteristics necessary for simulating dnapl infiltration, redistribution, and immobilization in saturated porous media, *Water Resour. Res.*, 39(8), doi: 10.1029/2002WR001270.

Gerig, G., O. Kubler, R. Kikinis and F. Jolesz (1992), Nonlinear anisotropic filtering of mri data, *IEEE Transactions on Medical Imaging*, 11(2):221–232.

Gladkikh, M. and S. Bryant (2003), Prediction of interfacial areas during imbibition in simple porous media, *Adv. Water Resour.*, 26:609–622.

Grant, G. P. and J. I. Gerhard (2007a), Simulating the dissolution of a complex dense non-aqueous phase liquid source zone: 1. Model to predict interfacial area, *Water Resour. Res.*, 43, doi:10.1029/2007WR006038.

Grant, G. P. and J. I. Gerhard (2007b), Simulating the dissolution of a complex dense non-aqueous phase liquid source zone: 2. Experimental validation of an area-based mass transfer model, *Water Resour. Res.*, 43, doi:10.1029/2007WR006039.

Gray, B. and M. S. Hassanizadeh (1998), averaging theorems and averaged equations for transport of interface properties in multiphase systems, *Int. J. Multiphase Flow*, 15(1):81–95.

Gray, W. G. (1999), Thermodynamics and constitutive theory for multiphase porous-media flow considering internal geometric constraints, *Adv. Water Resour.*, 22(5):521–547.

Gray, W. G. and M. S. Hassanizadeh (1991), Paradoxes and realities in unsaturated flow theory, *Water Resour. Res.*, 27(8):1847–1854.

Gray, W. G., A. Tompson and W. Soll (2002), Closure conditions for two-fluid flow in porous media, *Trans. Porous Media*, 47:29–65.

Gunstensen, A. K., D. H. Rothman, S. Zaleski and G. Zanetti (1991), Lattice boltzmann model of immiscible fluids, *Phys. Rev. A*, 43(8):4320–4327, doi: 10.1103/PhysRevA.43.4320.

Hassanizadeh, M. S., M. A. Celia and H. K. Dahle (2002), Dynamic effect in the capillary pressure - saturation relationship and its impacts on unsaturated flow, *Vadose Zone J.*, 1:38–57.

Hassanizadeh, M. S. and W. G. Gray (1990), Mechanics and thermodynamics of multiphase flow in porous media including interphase boundaries, *Adv. Water Resour.*, 13(4):169–186.

Hassanizadeh, M. S. and W. G. Gray (1993), Thermodynamic basis of capillary pressure in porous media, *Water Resour. Res.*, 29(10):3389–3405.

Held, R. J. and M. A. Celia (2001), Modeling support of functional relationships between capillary pressure, saturation, interfacial area and common lines, *Adv. Water Resour.*, 24:325–343.

Hillel, D. (1998), *Environmental Soil Physics*, Academic Press.

Hilpert, M. and C. T. Miller (2001), Pore-morphology-based simulation of drainage in totally wetting porous media, *Adv. Water Resour.*, 24(3):243–255.

Hopmans, J. W., T. Vogel and P. D. Koblik (1992), X-ray tomography of soil water distribution in one-step outflow experiments, *Soil Sci. Soc. Am. J.*, 56:355–362.

Huang, H., D. T. Thorne, M. Schaap and M. C. Sukop (2007), Proposed approximation for contact angles in Shan-and-Chen-type multicomponent multiphase lattice Boltzmann models, *Phys. Rev. E*, 76(6):066701, doi: 10.1103/PhysRevE.76.066701.

Inamuro, T., T. Ogata, S. Tajima and N. Konishi (2004), A lattice-boltzmann method for incompressible two-phase flows with large density differences, *J. Comp. Phys.*.

Joekar-Niasar, V., S. M. Hassanizadeh and A. Leijnse (2007), Insights into the relationship among capillary pressure, saturation, interfacial area and relative permeability using pore-network modeling, *Transp. Porous Med.*, doi: 10.1007/s11242-007-9191-7.

Kaestner, A., E. Lehmann and M. Stampanoni (2008), Imaging and image processing in porous media research, *Adv. Water Resour.*, doi: 10.1016/j.advwatres.2008.01.022.

Ketcham, R. A. and G. J. Iturrino (2005), Nondestructive high-resolution visualization and measurement of anisotropic effective porosity in complex lithologies using high-resolution x-ray computed tomography, *Journal of Hydrology*, 302:92–106, doi:10.1016/j.jhydrol.2004.06.037.

Kim, H. and P. S. C. Rao (1997), Determination of effective air-water interfacial area in partially saturated porous media using surfactant adsorption, *Water Resour. Res.*, 33(12):2705–2711.

Kim, H., P. S. C. Rao and M. D. Annable (1999a), Consistency of the interfacial tracer technique: experimental evaluation, *J. Contam. Hydrol.*, 40:79–94.

Kim, H., P. S. C. Rao and M. D. Annable (1999b), Gaseous tracer technique for estimating air-water interfacial areas and interface mobility, *Soil Sci. Soc. Am. J.*, 63:1554–1560.

Kool, J. B. and J. C. Parker (1987), Development and evaluation of closed-form expressions for hysteretic soil hydraulic properties, *Water Resour. Res.*, 23(1):105–114.

Kueper, B. H. and E. O. Frind (1991), Two-phase flow in heterogeneous porous media 2. model application, *Water Resour. Res.*, 27(6):1059–1070.

Lenhard, R. J., M. Oostrom and J. H. Dane (2004), A constitutive model for air-napl-water flow in the vadose zone accounting for immobile, non-occluded (residual) napl in strongly water-wet porous media, *J. Contam. Hydrol.*, 71:261–282.

Lenhard, R. J. and J. C. Parker (1987), Measurement and prediction of saturation-pressure relationships in three-phase porous media systems, *J. Contam. Hydrol.*, 1:407–424.

Leverett, M. (1941), Capillary behavior in porous solids, *Trans. Am. Inst. Min. Metal. Pet. Eng.*, 142:152–169.

Li, H., C. Pan and C. T. Miller (2005), Pore-scale investigation of viscous coupling effects for two-phase flow in porous media, *Phys. Rev. E*, 72.

Lindquist, W. (1999), 3dma general users manual, stony Brook AMS Preprints. http://www.ams.sunysb.edu/papers/papers99.html.

Lindquist, W. and A. Venkatarangan (1999), Investigating 3d geometry of porous median from high resolution images, *Phys. Chem. Earth(A)*, 25(7):593–599.

Lindquist, W., A. Venkatarangan, J. Dunsmuir and T. fong Wong (2000), Pore and throat size distributions measured from synchrotron x-ray tomographic images of fontainebleau sandstones, *J. Geophys. Res.*, 105(B9):21509–21527.

Lindquist, W. B., S.-M. Lee, D. A. Coker, K. W. Jones and P. Spanne (1996), Medial axis analysis of void structure in three-dimensional tomographic images of porous media, *J. Geophys. Res.*, 101(B4):8297–8310.

Liu, G. R. and M. B. Liu (2003), *Smoothed Particle Hydrodynamics: A Meshfree Particle Method*, World Scientific.

Liu, Y., J. W. Hopmans, M. Grismer and J. Chen (1998), Direct estimation of air-oil and oil-water capillary pressure and permeability relations from multi-step outflow experiments, *J Contam. Hydrol.*, 32:223–245.

Luckner, L., M. T. van Genuchten and D. R. Nielsen (1989), A consistent set of parametric models for two-phase flow of immiscible fluids in the subsurface, *Water Resour. Res.*, 25(10):2187–2193.

Ma, W. J., A. Martian, J. R. Banavar and J. Koplik (1992), Dynamics of phase separation of binary fluids, *Phys. Rev. A*, 45:5347–5350.

MacQueen, J. B. (1967), Some methods for classification and analysis of multivariate observations, in *Proceedings of 5-th Berkeley Symposium on Mathematical Statistics and Probability*, pages 281–297, Berkeley, University of California Press.

Martic, G., J. D. Coninck and T. D. Blake (2003), Influence of the dynamic contact angle on the characterization of porous media, *J. Colloid and Interface Sci.*, 263(1):213–216, doi:10.1016/S0021-9797(03)00283-2.

Martys, N. S. and H. Chen (1996), Simulation of multicomponent fluids in complex three-dimensional geometries by the lattice boltzmann method, *Phys. Rev. E*, 53(1):743–750.

McClure, J., D. Adalsteinsson, C. Pan, W. Gray and C. Miller (2007), Approximation of interfacial properties in multiphase porous media systems, *Adv. Water Resour.*, 30(1):354–365.

McClure, J., C. Pan, D. Adalsteinsson, W. Gray and C. Miller (2004), Estimating interfacial areas resulting from lattice-boltzmann simulation of two-fluid-phase flow in a porous medium, in C. T. Miller, M. W. Farthing, W. G. Gray and G. F. Pinder, editors, *Computational Methods in Water Resources XV*, volume 1.

McNamara, G. and G. Zanetti (1988), Boltzmann equation to simulate lattice gas automata, *Phys. Rev. Lett.*, 61:2332–2335.

Miller, C. T., G. Christakos, P. T. Imhoff, J. F. McBride, J. A. Pedit and J. A. Trangestein (1998), Multiphase flow and transport modeling in heterogeneous porous media: challenges and approaches, *Adv. Water Resour.*, 21(2):77–120.

Miller, C. T., M. M. Poirier-McNeill and A. S. Mayer (1990), Dissolution of trapped nonaqueous phase liquids: Mass transfer characteristics, *Water Resour. Res.*, 26(11):2783–2796.

Montemagno, C. D. and Y. Ma (1999), Measurement of interfacial surface areas for two-phase flow in porous media from pvi data, in M. T. van Genuchten, F. Leije and L. Wu, editors, *Characterization and Measurements of Hydraulic Properties of Unsaturated Porous Media*, pages 121–132, University of California Press, Riverside.

Morrow, N. R. (1970), Physics and thermodynamics of capillary action in porous media, *Ind. Eng. Chem.*, 62(6):32–56.

Mualem, Y. (1974), A conceptual model of hysteresis, *Water Resour. Res.*, 10(3):514–520.

Muccino, J. C., W. G. Gray and L. A. Ferrand (1998), Toward an improved understanding of multiphase flow in porous media, *Rev. Geophys.*, 36(3):401–422.

Muraleetharan, K. K. and C. Wei (1999), Dynamic behavior of unsaturated porous media: governing equations using the theory of mixtures with interfaces (tmi), *Int. J. Num. Anal. Meth. Geomech.*, 23:1579–1608.

Murdoch, A. I. and M. S. Hassanizadeh (2002), Macroscale balance relations for bulk, interfacial and common line systems in multiphase flows through porous media on the basis of molecular considerations, *Int. J. Multiphase Flow*, 28:1091–1123.

O'Carroll, D. M., L. M. Abriola, C. A. Polityka, S. A. Bradford and A. H. Demond (2005), Prediction of two-phase capillary pressure-saturation relationships in fractional wettability systems, *J. Contam. Hydrol.*, 77:247–270, doi: 10.1016/j.jconhyd2005.01.004.

Oh, W. and B. Lindquist (1999), Image thresholding by indicator kriging, *IEEE Trans. Pattern Anal. Mach. Intell.*, 21(7):590–602.

Oostrom, M., C. Hofstee, R. Lenhard and T. Wiestma (2003), Flow behavior and residual saturation formation of liquid carbon tetrachloride in unsaturated heterogeneous porous media, *J. Contam. Hydrol.*, 64:93–112, doi: 10.1016/S0169-7722(02)00107-9.

Oostrom, M. and R. J. Lenhard (1998), Comparison of relative permeability-saturation-pressure parametric models for infiltration and redistribution of a light nonaqueous-phase liquid in sandy porous media, *Adv. Water Resour.*, 21(2):145–157.

Oostrom, M., M. D. White and M. L. Brusseau (2001), Theoretical estimation of free and entrapped nonwetting-wetting fluid interfacial areas in porous media, *Adv. Water Resour.*, 24:887–898.

Øren, P. and S. Bakke (2003), Reconstruction of berea sandstone and pore-scale modeling of wettability effects, *J. Pet. Sci. Eng.*, 39:177–199, doi: 10.1016/S0920-4105(03)00062-7.

Orlandini, E., M. R. Swift and J. M. Yeomans (1995), A lattice-boltzmann model of binary-fluid mixtures, *Europhys. Lett.*, 32:463–468.

Pal, N. R. (1996), On minimum cross-entropy thresholding, *Pattern Recogn.*, 29(4):575–580.

Pan, C. (2004), *Use of Pore-scale Modeling to Understand Flow and Transport in Porous Media*, Ph.D. thesis, University of North Carolina at Chapel Hill.

Pan, C., M. Hilpert and C. T. Miller (2004), Lattice-boltzmann simulation of two-phase flow in porous media, *Water Resour. Res.*, 40, doi:10.1029/2003WR002120.

Pappas, T. N. (1992), An adaptive clustering algorithm for image segmentation, *IEEE Trans. Signal Process.*, 40(4):901–914.

Parker, J. C. and R. J. Lenhard (1987), A model for hysteretic constitutive relations governing multiphase flow 1. saturation-pressure relations, *Water Resour. Res.*, 23(12):2187–2196.

Patzek, T. W. (2000), Verification of a complete pore network simulator of drainage and imbibition, SPE 59312.

Perona, P. and J. Malik (1990), Scale-space and edge detection using anisotropic diffusion, *IEEE Trans. Pattern Anal. Mach. Intel.*, 12(7):629–639.

Petitot, J. (2003), An introduction to the Mumford-Shah segmentation model, *J. Physiol. Paris*, 97:335–342, doi: 10.1016/j.jphysparis.2003.09.007.

Porter, M. L., M. G. Schaap and D. Wildenschild (2008a), Comparison of interfacial area estimates in a multiphase porous system using computed microtomography data and lattice-Boltzmann simulations, *Water Resour. Res.*, in preparation.

Porter, M. L. and D. Wildenschild (2008), Validation of an image analysis method for computed microtomography image data of multiphase flow in porous systems, *Comput. Geosciences*, in preparation.

Porter, M. L., D. Wildenschild, G. P. Grant and J. I. Gerhard (2008b), Investigating nonwetting-wetting phase specific interfacial area in an NAPL-water-glass bead system using computed microtomography data, *Water Resour. Res.*, in preparation.

Powers, S. E., L. M. Abriola and W. J. Weber (1992), An experimental investigation of non-aqeous phase liquid dissolution in saturated subsurface systems: Steady state mass transfer rates, *Water Resour. Res.*, 28(10):2691–2705.

Powers, S. E., W. H. Anckner and T. F. Seacord (1996), Wettability of napl-contaminated sands, *J. Envir. Eng.*, 122(10):889–896.

Prodonavić, M., W. B. Lindquist and R. Seright (2006), Porous structure and fluid partitioning in polyethylene cores from 3d x-ray microtomography imaging, *J. Colloid and Interface Sci.*, 298:282–297, doi:10.1016/j.jcis.2005.11.053.

Prodonavić, M., W. B. Lindquist and R. Seright (2007), 3d image-based characterization of fluid displacement in berea core, *Adv. Water Resour.*, 30:214–226, doi: 10.1016/j.advwatres.2005.05.015.

Pyrak-Nolte, L. J., D. Nolte, D. Chen and N. J. Giordano (In Press), Relating capillary pressure to interfacial areas, *Water Resour. Res.*, doi: 10.1029/2007WR006434.

Quartapelle, L. (1993), *Numerical solution of the Incompressible Navier-Stokes Equations*, Birkhauser Verlag, Switzerland.

Reeves, P. C. and M. A. Celia (1996), A functional relationship between capillary pressure, saturation and interfacial area as revealed by a pore-scale network model, *Water Resour. Res.*, 32(8):2345–2358.

Rivers, M. L. (2001), *GSECARS Tomography Processing Software*, http://cars9.uchicago.edu/software/idl/tomography.html.

Rothman, D. H. and S. E. Zaleski (1997), *Lattice-Gas Cellular Automata*, Cambridge University Press.

Sakai, T. and T. H. Illangasekare (2007), Comparison of height-averaged and point measured capillary pressure-saturation relations for sands using a modified tempe cell, *Water Resour. Res.*, 43, doi: 10.1029/2006WR005814.

Saripalli, K., H. Kim, P. Sao and M. Annable (1997), Measurement of specific fluid-fluid interfacial areas of immiscible fluids in porous media, *Environ. Sci. Technol.*, 31(3):932–936.

Schaap, M. G. and I. Lebron (2001), Using microscope observations of thin sections to estimate soil permeability with the kozeny-carman equation, *J. of Contam. Hydrol.*, 251:186–201.

Schaap, M. G., M. L. Porter, B. S. Christensen and D. Wildenschild (2007), Comparison of pressure-saturation characteristics derived from computed tomography images and lattice-boltzmann simulations, *Water Resour. Res.*, 43, doi: 10.1029/2006WR005730.

Schaefer, C., D. DiCarlo and M. Blunt (2000), Determination of water-oil interfacial area during 3-phase gravity drainage in porous media, *J. Colloid and Interface Sci.*, 221(2):308–312.

Scheckel, K. G., R. Hamon, L. Jassogne, M. Rivers and E. Lombi (2007), Synchrotron x-ray absorption-edge computed microtomography imaging of thallium compartmentalization in iberis intermedia, *Plant Soil*, (290):51–60, doi:10.1007/s11104-006-9102-7.

Schnaar, G. and M. L. Brusseau (2005), Pore-scale characterization of organic immiscible-liquid morphology in natural porous media using synchrotron x-ray microtomography, *Environ. Sci. Technol.*, 39:8403–8410.

Schnaar, G. and M. L. Brusseau (2006), Characterizing pore-scale configuration of organic immiscible liquid in multi-phase systems using synchrotron x-ray microtomography, *Vadose Zone J.*, 5:641–648.

Scott, P. S., G. J. Farquhar and N. Kouwen (1983), Hysteretic effects on net infiltration, in *Advances in Infiltration*, pages 163–170, American Society of Agricultural Engineers.

Selker, J. S., C. K. Keller and J. T. McCord (1999), *Vadose Zone Processes*, Lewis Publishers.

Sezgin, M. and B. Sankur (2001), Selection of thresholding methods for non-destructive testing applications, in *Image Processing, 2001. Proceedings. 2001 International Conference on*, volume 3, pages 764–767, doi: 10.1109/ICIP.2001.958231.

Sezgin, M. and B. Sankur (2004), Survey over image thresholding techniques and quantitative performance evaluation, *J. Electronic Imaging*, 13(1):146–165.

Shan, X. and H. Chen (1993), Lattice-boltzmann model for simulating flows with multiphases and components, *Phys. Rev. E*, 47:1815–1819.

Shan, X. and H. Chen (1994), Simulations of non-ideal gases and liquid-gas phase transitions by the lattice-boltzmann equation, *Phys. Rev. E*, 49:2941–2948.

Shan, X. and G. Doolen (1996), Diffusion in a multicomponent lattice boltzmann equation model, *Phys. Rev. E*, 54(4):3614–3620.

Sheppard, A. P., R. M. Sok and H. Averdunk (2004), Techniques for image enhancement and segmentation of tomographic images of porous materials, *Phys. A*, 339:145–151, doi: 10.1016/j.physa.2004.03.057.

Silin, D. and T. Patzek (2006), Pore space morphology analysis using maximal inscribed spheres, *Phys. A*, 371:336–360, doi: 10.1016/j.physa.2006.04.048.

Simdyankin, S. I. and M. Dzugutov (2003), Case study: Computational physics - the molecular dynamics method, Technical report, Royal Institute of Technology, Sweden.

Simunek, J., M. Sejna and M. T. van Genuchten (1999), The hydrus-2d software package for simulating the two-dimensional movement of water, heat, and multiple solutes in variably-saturated media, Technical report.

Smiles, D. E., G. Vachaud and M. Vauclin (1971), A test of the uniqueness of the soil moisture characteristic during transient, nonhysteretic flow of water in a rigid soil, *Soil Sci. Soc. Amer. Proc.*, 35:534–539.

Smith, R. E., K. R. J. Smetten, P. Broadbridge and D. A. Woolhiser (2002), *Infiltration Theory for Hydrologic Applications*, American Geophysical Union.

Song, S.-R., K. W. Jones, W. B. Lindquist, B. A. Dowd and D. L. Sahagian (2001), Synchrotron x-ray computed microtomography studies of vesiculated basaltic rocks, *Bull. Volcanol.*, 63:252–263.

Succi, S. (2001), *The Lattice Boltzmann Equation for fluid Dynamics and Beyond*, Oxford University Press.

Sukop, M. and D. Or (2003), Invasion percolation of single component, multiphase fluids with lattice-boltzmann models, *Physica B*, 338:298–303.

Sukop, M. C. and D. T. Thorne (2006), *Lattice Boltzmann Modeling An Introduction for Geoscientists and Engineers*, Springer.

Swift, M. R., E. Orlandini, W. R. Osborn and J. M. Yeomans (1996), Lattice boltzmann simulation of liquid-gas and binary fluid systems, *Phys. Rev. E*, 54(5):5041–5052.

Swift, M. R., W. R. Osborn and J. M. Yeomans (1995), Lattice boltzmann simulation of nonideal fluids, *Phys. Rev. Lett.*, 75(5):830–833.

Tartakovsky, A. M. and P. Meakin (2005a), Modeling of surface tension and contact angles with smoothed particle hydrodynamics, *Phys. Rev. E*, 72, doi: 10.1103/PhysRevE.72.026301.

Tartakovsky, A. M. and P. Meakin (2005b), Simulation of unsaturated flow in complex fractures using smoothed particle hydrodynamics, *Vadose Zone J.*, 4:848–855, doi: 10.2136/vzj2004.0178.

Tartakovsky, A. M., P. Meakin, T. D. Scheibe and B. D. Wood (2007), A smoothed particle hydrodynamics model for reactive transport and mineral precipitation in porous and fractured porous media, *Water Resour. Res.*, 43, doi: 10.1029/2005WR004770.

Thieme, J., G. Schneider and C. Knöchel (2003), X-ray tomography of a microhabitat of bacteria and other soil colloids with sub-100 nm resolution, *Micron*, 34:339–344, doi: 10.1016/S0968-4328(03)000061-1.

Tölke, J., M. Krafczyk, M. Schulz and E. Rank (2000), Lattice-boltzmann simulations of binary fluid flow through porous media, *Philos. Trans. R. Soc. London A*, 360:535–545.

Topp, G. C., A. Klute and D. B. Peters (1967), Comparison of water content-pressure head data obtained by equilibrium, steady state and unsteady state methods, *Soil Sci. Soc. Amer. Proc.*, 31:312–314.

Torquato, S. (2002), *Random Heterogeneous Materials Microstructure and Microscopic Properties*, Springer.

Turner, M., L. Knüfing, C. Arns, A. Sakellariou, T. Senden, A. Sheppard, R. Sok, A. Limaye, W. Pinczewski and M. Knackstedt (2004), Three-dimensional imaging of multiphase flow in porous media, *Phys. A*, 339:166–172, doi: 10.1016/j.physa.2004.03.059.

van Genuchten, M. T. (1980), A closed-form equation for predicting the hydraulic conductivity of unsaturated soils, *Soil Sci. Soc. Am. J.*, 44:892–898.

Vogel, H.-J., J. Tölke, V. Schulz, M. Krafczyk and K. Roth (2005), Comparison of a lattice-boltzmann model, a full-morphology model, and a pore network model for determining capillary pressure -saturation relationships, *Vadose Zone J.*, 4:380–388.

Vogel, T., M. T. van Genuchten and M. Cislerova (2001), Effect of the shape of the soil hydraulic functions near saturation on variably-saturated flow predictions, *Adv. Water Resour.*, 24:133–144.

Wei, C. and K. K. Muraleetharan (2002), A continuum theory of porous media saturated by multiple fluids: Ii lagrangian description and variational structure, *Int. J. Eng. Sci.*, 40:1835–1854.

Welge, H. J. (1948), Displacement of oil from porous media by water and gas, *Petroleum Technology*, pages 133–145.

White, M. D. and M. Oostrom (2000), Stomp subsurface transport over multiple phase: Theory guide, Technical report, PNNL-11216 (UC-2010), Pacific Northwest National Laboratory, Richland, Washington.

Wildenschild, D., J. W. Hopmans, M. L. Rivers and A. J. Kent (2005), Quantitative analysis of flow processes in a sand using synchrotron-based x-ray microtomography, *Vadose Zone J.*, 4:112–126.

Wildenschild, D., J. W. Hopmans, C. Vaz, M. L. Rivers, D. Rikard and B. S. Christensen (2002), Using x-ray computed microtomography in hydrology: Systems, resolution and limitations, *J. Hydrol.*, 267:285–297.

Wildenschild, D., J. W. Hopmans and J. Šimůnek (2001), Flow rate dependence of soil hydraulic characteristics, *Soil Sci. Soc. Amer. J.*, 65:35–48.

Wildenschild, D., K. H. Jensen, K. J. Hollenbeck, T. H. Illagasekare, D. Znidarcic, T. Sonnenborg and M. B. Butts (1997), A two-stage procedure for determining unsaturated hydraulic characteristics using a syringe pump and outflow observations, *Soil Sci. Soc. Amer. J.*, 61(2):347–359.

Williams, G. P. (1969), Numerical integration of the three dimensional Navier-Stokes equations for incompressible flow, *J. of Fluid Mech.*, 37(4):727–750.